NUREG/CR-3046
PNL-4385
Vol. 1

COBRA/TRAC - A Thermal-Hydraulics Code for Transient Analysis of Nuclear Reactor Vessels and Primary Coolant Systems

Equations and Constitutive Models

Prepared by M. J. Thurgood, J. M. Kelly, T. E. Guidotti,
R. J. Kohrt, K. R. Crowell

Pacific Northwest Laboratory
Operated by
Battelle Memorial Institute

Prepared for
U.S. Nuclear Regulatory
Commission

GPO Printed copy price: $7.00

NUREG/CR-3046
PNL-4385
Vol. 1
R4

COBRA/TRAC - A Thermal-Hydraulics Code for Transient Analysis of Nuclear Reactor Vessels and Primary Coolant Systems

Equations and Constitutive Models

Manuscript Completed: November 1982
Date Published: March 1983

Prepared by
M. J. Thurgood, J. M. Kelly, T. E. Guidotti,
R. J. Kohrt, K. R. Crowell

Pacific Northwest Laboratory
Richland, WA 99352

Prepared for
Division of Accident Evaluation
Office of Nuclear Regulatory Research
U.S. Nuclear Regulatory Commission
Washington, D.C. 20555
NRC FIN B2391

ABSTRACT

The COBRA/TRAC computer program has been developed to predict the thermal-hydraulic response of nuclear reactor primary coolant systems to small and large break loss-of-coolant accidents and other anticipated transients. The code solves the compressible three-dimensional, two-fluid, three-field equations for two-phase flow in the reactor vessel. The three fields are the vapor field, the continuous liquid field, and the liquid drop field. A five-equation drift flux model is used to model fluid flow in the primary system piping, pressurizer, pumps, and accumulators. The heat generation rate of the core is specified by input and no reactor kinetics calculations are included in the solution. This volume describes the conservation equations and physical models used in the vessel module.

CONTENTS

FIGURES

TABLES

ACKNOWLEDGEMENTS

COBRA/TRAC is the result of the efforts of a number of people. We wish to acknowledge the main contributors and to express our appreciation to those who have offered their advice and suggestions.

The main contributors to the program are listed below.

Fluid Dynamics:	M. J. Thurgood, T. L. George, and T. E. Guidotti
Heat Transfer:	J. M. Kelly and R. J. Kohrt
Turbulence Model:	K. R. Crowell
Graphics and Programming:	A. S. Koontz
Simulations:	K. L. Basehore, S. H. Bian, J. M. Cuta, R. J. Kohrt, G. A. Sly, and C. A. Wilkins
One-Dimensional Components and Code Architecture:	Members of the TRAC Code Development Group at LANL

We wish to thank Dr. S. Fabic of the U.S. Nuclear Regulatory Commission for his patience, support, and suggestions during this large undertaking. We also wish to thank Drs. Tong, Shotkin, Han and Zuber of the U.S. Nuclear Regulatory Commission and members of the Advanced Code Review Group for their many helpful suggestions. We also express our gratitude to our manager, Dr. D. S. Trent, for his support, and Cathy Darby and Peggy Snyder for their lead roles in typing this report.

NOMENCLATURE

A	flow area
A_H	heat transfer surface area
A_I	intercell friction area
A_I'''	interfacial area per unit volume
A_K	transverse flow area
a	absorption coefficient
b	phase mobility
C_D	drag coefficient
C_p	specific heat capacity
$\underline{\underline{D}}$	deformation tensor
$\underline{\underline{D}}^*$	deleted deformation tensor
D_H	hydraulic diameter
$\underline{\underline{F}}$	turbulence anisotropy tensor
$\underline{F}_I$	intercell drag force
F	gray body factor
f	friction factor
G	mass flux
g_c	gravitational conversion constant
g	gravitational acceleration
$\underline{g}$	gravitational acceleration vector
H	heat transfer coefficient
h	enthalpy
h_{fg}	enthalpy of vaporization
j	superficial velocity
K	loss coefficient
K_I	interfacial friction coefficient
k	thermal conductivity
k_s	equivalent sand roughness
k_σ	mass transfer coefficient
L	transverse coordinate
ℓ_h	energy mixing length
ℓ_m	momentum mixing length

$\underline{M}^d$	interfacial drag force
M_i	mass of heat transfer node i
$\underline{M}^\Gamma$	interfacial momentum exchange due to mass transfer
m	mass flow rate
N	number density
N_μ	viscosity number
P	pressure
p^T	turbulent pressure
Pr	Prandtl number
Pr^t	turbulent Prandtl number
P_w	wetted perimeter
$\underline{Q}$	conduction heat flux
Q_w'''	wall heat flux per unit fluid volume
$\underline{q}$	fluid-fluid conduction heat flux
q''	surface heat flux
q_I''	interfacial heat flux per unit volume
$\underline{q}^T$	turbulent heat flux
R	internode resistance
Re	Reynolds number
r	radius
S	net rate of entrainment
S_{DE}	rate of de-entrainment
S_E	rate of entrainment
S_k	gap width of gap k
S_u	entrainment correlation parameter
S_Γ	rate of interfacial area concentration change due to phase change
S'_{nk}	orthogonal gap width
S'''	net rate of entrainment per unit volume
$(S'''\underline{U})$	momentum exchange due to entrainment
T	temperature
$\underline{\underline{T}}$	stress tensor
$\underline{\underline{T}}^T$	Reynolds stress tensor
t	time
Δt	averaging time interval

$\underline{U}$	fluid velocity
$\underline{U}_{vj}$	drift velocity
u	velocity component in vertical (x) direction
V	volume
v	velocity component in transverse (y) direction
We	Weber number
w	velocity component in transverse (z) direction
x	vertical direction
y	transverse direction
z	transverse direction

Greek Symbols

α	void fraction
β	thermal expansion coefficient
Γ	net rate of mass transfer per unit volume
Γ'''	net rate of vapor generation per unit volume
$(\Gamma'''\underline{U})$	momentum exchange due to vapor generation
δ	film thickness
δ_{ij}	Kronecker delta
ϵ	thermal diffusivity
ϵ^T	turbulent thermal diffusivity
η	fraction of vapor generation coming from entrained liquid
η_{NR}	de-entrainment efficiency
μ	viscosity
μ^T	turbulent viscosity
ρ	density
$\underline{\underline{g}}$	fluid-fluid stress tensor
σ	surface tension
$\underline{\underline{\tau}}$	viscous stress tensor (stress deviator)
$\underline{\tau}_I'''$	interfacial drag force per unit volume
λ	characteristic wavelength
σ_β	Boltzman constant

Subscripts

B	bulk
BR	bubble rise
b	bubble
CHF	critical heat flux
DE	de-entrainment
d	drop
E	entrainment
e	entrained field
f	saturated liquid film
g	saturated vapor
I	interfacial
i	heat transfer nodes
j	
k	phase k
ℓ	liquid field
MIN	minimum film boiling point
m	mixture
R	relative
SHL	superheated liquid
SCL	subcooled liquid
SHV	superheated vapor
SCV	subcooled vapor
SP	single phase
S	surface
s	drop formation
V	vapor phase (Vapor properties used in heat transfer correlations are evaluated at the film temperature.)
v	vapor field
vℓ	between vapor and liquid fields
ve	between vapor and entrained fields
W-D	wall to drop
W-V	wall to vapor

x	
y	directions
z	
2ϕ	two phase

Superscripts

i	interfacial surface average
n	old time level
n+1	new time level
s	surface average
T	turbulent
t	transpose

COBRA/TRAC - A THERMAL-HYDRAULICS CODE FOR TRANSIENT ANALYSIS OF NUCLEAR REACTOR VESSELS AND PRIMARY COOLANT SYSTEMS VOLUME 1: EQUATIONS AND CONSTITUTIVE MODELS

1.0 INTRODUCTION

The COBRA/TRAC computer program has been developed to predict the thermal-hydraulic response of nuclear reactor primary coolant systems to small-and large-break loss-of-coolant accidents and other anticipated transients. It is derived from the merging of COBRA-TF and TRAC-PD2 (Ref. 1).

The COBRA-TF computer code provides a two-fluid, three-field representation of two-phase flow. Each field is treated in three dimensions and is compressible. Continuous vapor, continuous liquid and entrained liquid drop are the three fields. The conservation equations for each of the three fields and for heat transfer from and within the solid structures in contact with the fluid are solved using a semi-implicit, finite-difference numerical technique on an Eulerian mesh. COBRA-TF features extremely flexible noding for both the hydrodynamic mesh and the heat transfer solution. This flexibility provides the capability to model the wide variety of geometries encountered in vertical components of nuclear reactor primary systems.

TRAC-PD2 is a systems code designed to model the behavior of the entire reactor primary system. It features special models for each component in the system. These include accumulators, pumps, valves, pipes, pressurizers, steam generators, and the reactor vessel. With the exception of the reactor vessel, the thermal-hydraulic response of these components to transients is treated with a five-equation drift flux representation of two-phase flow. The vessel component of TRAC-PD2 is somewhat restricted in the geometries that can be modeled and cannot treat the entrainment of liquid drops from the continuous liquid phase directly.

The TRAC-PD2 vessel module has been removed and COBRA-TF has been implemented as the new vessel component in TRAC-PD2. The resulting code is COBRA/TRAC. The vessel component in COBRA/TRAC has the extended capabilities

provided by the three-field representation of two-phase flow and the flexible noding. The code has been assessed against a variety of two-phase flow data from experiments simulating important phenomena anticipated during postulated accidents and transients.

The documentation of the COBRA/TRAC program consists of five separate volumes. Volume 1 contains a description of the basic three-field conservation equations and constitutive models used in the vessel component (COBRA-TF). Volume 2 contains the finite-difference equations for the vessel. It describes the numerical techniques used to solve these equations and the coupling between the TRAC-PD2 equations and the COBRA-TF vessel equations. Volume 3 is the Users' Manual. It contains line-by-line input instructions for COBRA/TRAC and user-guidance for application of the code. Volume 4, the Applications Manual, contains the results of simulations run to assess the performance of the code. Volume 5 is a Programmers' Guide.

This volume, Equations and Constitutive Models, describes the conservation equations and physical models used in the vessel module. The constitutive relations in COBRA-TF include state-of-the-art physical models for the interfacial mass transfer, the interfacial drag forces, the liquid and vapor wall drag, the wall and interfacial heat transfer, the rate of entrainment and deentrainment, and the thermodynamic properties of water. In addition, a mixing length turbulence model has been included as an option. Section 2 presents the two-fluid phasic conservation equations and their extension to the three-field model. The physical models used in the hydrodynamic solution are discussed in Section 3. The physical models for the heat transfer solution are given in Section 4. Appendix A to this volume provides the derivation of the two-fluid phasic conservation equations. Appendix B lists the nuclear material properties used by the nuclear rod model. Appendix C describes the logic for calculating thermal connectors for the conduction solution.

2.0 CONSERVATION EQUATIONS FOR THE THREE-FIELD MODEL OF TWO-PHASE FLOW

Multiphase flows consist of two or more fluids separated by moving phase interfaces. Material properties are assumed to change discontinuously across these interfaces. In general, the phases present can be any combination of liquid, solid, or gas. The flow pattern can take any one of a wide variety of forms, such as bubbly flow, droplet flow, gas-particle flow, and stratified flow. Exact conservation equations can be derived for each phase, and jump conditions relating variables on each side of the phase interface can be formulated, much as in single-phase shock wave theory. With appropriate initial and boundary conditions, these equations could theoretically be solved for the exact motion of each phase and the phase interfaces. Except in a few simple cases, however, an exact analysis of multiphase flow is impossible because of its complex and essentially chaotic nature. Fortunately, one is generally not interested in the exact motion of each droplet or bubble but instead wants to learn something about the average behavior of each phase. Thus, most work in multiphase flow is done with some kind of average equations.

The average conservation equations used in the vessel module of COBRA/TRAC are derived following the methods of Ishii (Ref. 2). The average used is a simple Eulerian time average over a time interval, Δt, assumed to be long enough to smooth out the random fluctuations present in a multiphase flow but short enough to preserve any gross unsteadiness in the flow. The resulting average equations can be cast in either the mixture form or the two-fluid form. Because of its greater physical appeal and broader range of application, the two-fluid approach is used as the foundation for COBRA/TRAC.

The two-fluid formulation uses a separate set of conservation equations and constitutive relations for each phase. The effects of one phase on another are accounted for by interaction terms appearing in the equations. The conservation equations have the same form for each phase; only the constitutive relations and physical properties differ. Thus, although usually derived for two-phase flow, the two-fluid model immediately generalizes to n-phase flow.

The three-field formulation used in the vessel module of COBRA/TRAC is a straightforward extension of the two-fluid model. The fields included are vapor, continuous liquid, and entrained liquid. Dividing the liquid phase into two fields is the most convenient and physically reasonable way of handling flows where the liquid can appear in both film and droplet form. In such flows the motion of the droplets can be quite different from the motion of the film, so a single set of average liquid phase equations cannot adequately describe the liquid flow or the interaction between liquid and vapor.

Section 2 describes the development of the two-fluid, three-field conservation equations solved in the vessel module of COBRA/TRAC. The two-fluid phasic conservation equations are presented in Section 2.1, along with the assumptions necessary to obtain them. (The derivation of these equations can be found in Appendix A of this volume.) In Section 2.2 the additional assumptions and notation for the three-field model are presented, and the three-field conservation equations are derived. The equations are written out in component form in Section 2.3, and the classical subchannel form is compared with the Cartesian coordinate equations.

2.1 TWO-FLUID PHASIC CONSERVATION EQUATIONS

The phasic conservation equations given in this section describe the time-averaged behavior of phase k, which can be any phase in a multiphase flow. All fluid variables appearing in these equations are time-averaged quantities. The averaging process used is described in Appendix A, where precise definitions of all the average variables are given. The phasic conservation equations are general within the assumptions listed below.

Assumptions

1. Gravity is the only body force.
2. There is no volumetric heat generation in the fluid.
3. Radiation heat transfer is limited to rod to drop and rod to steam.
4. The pressure is the same in all phases.

5. The dissipation can be neglected in the enthalpy formulation of the energy equation.

While assumptions three and four simplify the conservation equations considerably, especially the energy equation, they also somewhat limit their applicability. But for situations typically encountered in reactor safety analysis these assumptions are usually justified. (Further discussion of these assumptions is given in Appendix A.)

Conservation of Mass

$$\frac{\partial}{\partial t}(\alpha_k \rho_k) + \nabla \cdot (\alpha_k \rho_k \underline{U}_k) = \Gamma_k \tag{2.1}$$

Rate of change of mass	+	Rate of mass efflux	=	Rate of mass transfer to phase k from the other phases

Conservation of Momentum

$$\frac{\partial}{\partial t}(\alpha_k \rho_k \underline{U}_k) + \nabla \cdot (\alpha_k \rho_k \underline{U}_k \underline{U}_k) = \alpha_k \rho_k \underline{g} - \alpha_k \nabla P$$

$$+ \nabla \cdot [\alpha_k (\underline{\underline{\tau}}_k + \underline{\underline{\tau}}_k^T)] + \underline{M}_k^{\Gamma} + \underline{M}_k^{d} \tag{2.2}$$

Rate of change of momentum	+	Rate of efflux of momentum	=	Gravity force	+	Pressure gradient force
+ Viscous and turbulent forces	+	Momentum exchange due to mass transfer to phase k	+	Interfacial drag force		

Conservation of Energy

$$\frac{\partial}{\partial t}(\alpha_k \rho_k h_k) + \nabla \cdot (\alpha_k \rho_k h_k \underline{U}_k) = -\nabla \cdot [\alpha_k (\underline{Q}_k + \underline{q}_k^T)] + \Gamma_k h_k^i + q_{I_k}''' + \alpha_k \frac{\partial P}{\partial t} \tag{2.3}$$

Rate of change of enthalpy	+	Rate of efflux of enthalpy	=	Conduction and turbulent heat flux	
+ Energy exchange due to mass transfer to phase k	+	Interfacial heat transfer	+	Pressure derivative	

The following definitions have been used in the above equations:

α_k = average k-phase void fraction

ρ_k = average k-phase density

$\underline{U}_k$ = average k-phase velocity

Γ_k = average rate of mass transfer to phase k from the other phases

$\underline{g}$ = acceleration of gravity

P = average pressure

$\underline{\underline{\tau}}_k$ = average k-phase viscous stress tensor (stress deviator)

$\underline{\underline{T}}_k$ = k-phase turbulent (Reynolds) stress tensor

$\underline{M}_k^\Gamma$ = average supply of momentum to phase k due to mass transfer to phase k

$\underline{M}_k^d$ = average drag force on phase k by the other phases

h_k = average k-phase enthalpy

$\underline{Q}_k$ = average k-phase conduction vector

$\underline{q}_k^T$ = k-phase turbulent heat flux

h_k^i = surface average enthalpy of phase k

2.2 THREE-FIELD CONSERVATION EQUATIONS

In the three-field formulation there are three continuity equations, three momentum equations, and two energy equations. (The two liquid fields are assumed to be in thermal equilibrium.) These equations are obtained from Equations 2.1 through 2.3 by introducing the appropriate three-field notation and a few simplifying assumptions.

2.2.1 Three-Field Model Notation

In general, the subscripts v, ℓ and e refer to the vapor, continuous liquid and entrained liquid fields, respectively. The term describing mass transfer between phases is, however, handled somewhat differently. Let

Γ''' = average rate of vapor generation per unit volume

Since both liquid fields can contribute to the vapor generation rate, let

η = the fraction of the total vapor generation coming from the entrained liquid

Γ_e''' = average rate of vapor generation per unit volume coming from the entrained liquid, $\Gamma_e''' = \eta\Gamma'''$

Γ_ℓ''' = average rate of vapor generation per unit volume coming from the continuous liquid, $\Gamma_\ell''' = (1 - \eta)\Gamma'''$

The two liquid fields can exchange mass by entrainment as well as by phase change. For notation let

S''' = average net rate of entrainment per unit volume

With the above definitions the mass transfer terms can be written as

$$\begin{aligned} \Gamma_v &= \Gamma''' \\ \Gamma_\ell &= -\Gamma_\ell''' - S''' = -(1 - \eta)\Gamma''' - S''' \\ \Gamma_e &= -\Gamma_e''' + S''' = -\eta\Gamma''' + S''' \end{aligned} \tag{2.4}$$

The interfacial momentum exchange terms can be expressed as

$$\begin{aligned} \underline{M}_v^d &= -\underline{\tau}_{I_{v\ell}}''' - \underline{\tau}_{I_{ve}}''' \\ \underline{M}_\ell^d &= \underline{\tau}_{I_{v\ell}}''' \\ \underline{M}_e^d &= \underline{\tau}_{I_{ve}}''' \end{aligned} \tag{2.5}$$

where

$\underline{\tau}_{I_{v\ell}}'''$ = average drag force per unit volume by the vapor on the continuous liquid

$\underline{\tau}_{I_{ve}}'''$ = average drag force per unit volume by the vapor on the entrained liquid

The momentum exchange due to mass transfer between the three fields can be written as

$$\begin{aligned} \underline{M}_v^\Gamma &= (\Gamma''' \underline{U}) \\ \underline{M}_\ell^\Gamma &= -(\Gamma_\ell''' \underline{U}) - (S''' \underline{U}) \\ \underline{M}_e^\Gamma &= -(\Gamma_e''' \underline{U}) + (S''' \underline{U}) \end{aligned} \tag{2.6}$$

This notation was chosen to emphasize the fact that $\underline{M}_v^\Gamma$ is due only to vapor generation, but $\underline{M}_\ell^\Gamma$ and $\underline{M}_e^\Gamma$ are affected by both vapor generation and entrainment.

2.2.2 Three-Field Model Assumptions

To obtain the three-field model from Equations 2.1 through 2.3, the following assumptions are needed:

1. The turbulent stresses and turbulent heat flux of the entrained phase can be neglected, so

$$\underline{\underline{T}}_e^T = 0$$

$$\underline{q}_e^T = 0 \qquad (2.7)$$

2. When the equations are solved on a finite-difference grid, the viscous stresses can be partitioned into wall shear and fluid-fluid shear. The fluid-fluid shear can be neglected in the entrained liquid phase. The notation for this is given below.

$$\nabla \cdot (\alpha_e \underline{\underline{\tau}}_e) = \underline{\tau}_{we}'''$$

$$\nabla \cdot (\alpha_v \underline{\underline{\tau}}_v) = \underline{\tau}_{wv}''' + \nabla \cdot (\alpha_v \underline{\underline{\sigma}}_v) \qquad (2.8)$$

$$\nabla \cdot (\alpha_\ell \underline{\underline{\tau}}_\ell) = \underline{\tau}_{w\ell}''' + \nabla \cdot (\alpha_\ell \underline{\underline{\sigma}}_\ell)$$

In Equation 2.8, $\underline{\tau}_{wv}'''$, $\underline{\tau}_{we}'''$, and $\underline{\tau}_{w\ell}'''$ are the forces exerted by the wall on the vapor, the entrained liquid and the continuous liquid, respectively; $\underline{\underline{\sigma}}_v$ and $\underline{\underline{\sigma}}_\ell$ are the fluid-fluid viscous stress tensors for the vapor and the liquid.

3. The conduction heat flux can be partitioned into a wall term and a fluid-fluid conduction term. The latter is assumed negligible in the entrained liquid. Thus,

$$-\nabla \cdot (\alpha_v \underline{Q}_v) = -\nabla \cdot (\alpha_v \underline{q}_v) + Q_{wv}'''$$

$$-\nabla \cdot (\alpha_e \underline{Q}_e + \alpha_\ell \underline{Q}_\ell) = -\nabla \cdot (\alpha_\ell \underline{q}_\ell) + Q_{w\ell}''' \qquad (2.9)$$

where Q_{wv}''' and $Q_{w\ell}'''$ are the wall heat transfer rates per unit volume to the vapor and liquid, respectively; $\underline{q}_\ell$ is the fluid-fluid conduction vector for the continuous liquid; and $\underline{q}_v$ is the fluid-fluid conduction vector for the vapor.

4. All mass entering or leaving a phase interface is at saturation. Therefore,

$$h_v^i = h_g$$

$$h_\ell^i = h_f \tag{2.10}$$

2.2.3 Three-Field Equations

Substituting Equations 2.4 through 2.10 into Equations 2.1 through 2.3 yields the three-field conservation equations used in COBRA-TF.

Conservation of Mass (3 equations)

$$\frac{\partial}{\partial t}(\alpha_v \rho_v) + \nabla \cdot (\alpha_v \rho_v \underline{U}_v) = \Gamma'''$$

$$\frac{\partial}{\partial t}(\alpha_\ell \rho_\ell) + \nabla \cdot (\alpha_\ell \rho_\ell \underline{U}_\ell) = -\Gamma_\ell''' - S'''$$

$$\frac{\partial}{\partial t}(\alpha_e \rho_\ell) + \nabla \cdot (\alpha_e \rho_\ell \underline{U}_e) = -\Gamma_e''' + S''' \tag{2.11}$$

Conservation of Momentum (3 equations)

$$\frac{\partial}{\partial t}(\alpha_v \rho_v \underline{U}_v) + \nabla \cdot (\alpha_v \rho_v \underline{U}_v \underline{U}_v) = -\alpha_v \nabla P + \alpha_v \rho_v \underline{g}$$

$$+ \nabla \cdot [\alpha_v (\underline{\underline{\sigma}}_v + \underline{\underline{I}}_v^T)] + \underline{\tau}_{wv}''' - \underline{\tau}_{Iv\ell}''' - \tau_{Ive}''' + (\Gamma''' \underline{U})$$

$$\frac{\partial}{\partial t}(\alpha_\ell \rho_\ell \underline{U}_\ell) + \nabla \cdot (\alpha_\ell \rho_\ell \underline{U}_\ell \underline{U}_\ell) = -\alpha_\ell \nabla P + \alpha_\ell \rho_\ell \underline{g}$$

$$+ \nabla \cdot [\alpha_\ell (\underline{\underline{\sigma}}_\ell + \underline{\underline{I}}_\ell^T)] + \underline{\tau}_{w\ell}''' + \underline{\tau}_{Iv\ell}''' - (\Gamma_\ell''' \underline{U}) - (S''' \underline{U})$$

$$\frac{\partial}{\partial t}(\alpha_e \rho_\ell \underline{U}_e) + \nabla \cdot (\alpha_e \rho_\ell \underline{U}_e \underline{U}_e) = -\alpha_e \nabla P + \alpha_e \rho_\ell \underline{g} + \underline{\tau}_{we}''' + \underline{\tau}_{Ive}'''$$

$$- (\Gamma_e''' \underline{U}) + (S''' \underline{U}) \qquad (2.12)$$

Conservation of Energy (2 equations)

$$\frac{\partial}{\partial t}(\alpha_v \rho_v h_v) + \nabla \cdot (\alpha_v \rho_v h_v \underline{U}_v) = -\nabla \cdot [\alpha_v (\underline{q}_v + \underline{q}_v^T)] + \Gamma''' h_g + q_{Iv}''' + Q_{wv}''' + \alpha_v \frac{\partial P}{\partial t}$$

$$\frac{\partial}{\partial t}[(\alpha_\ell + \alpha_e)\rho_\ell h_\ell] + \nabla \cdot (\alpha_\ell \rho_\ell h_\ell \underline{U}_\ell) + \nabla \cdot (\alpha_e \rho_\ell h_\ell \underline{U}_e)$$

$$= -\nabla \cdot [\alpha_\ell (\underline{q}_\ell + \underline{q}_\ell^T)] - \Gamma''' h_f + q_{I\ell}''' + Q_{w\ell}''' + (\alpha_\ell + \alpha_e) \frac{\partial P}{\partial t} \qquad (2.13)$$

The use of a single energy equation for the combined continous liquid and liquid droplet fields means that both fields are assumed to be at the same temperature. In regions where both liquid droplets and liquid films are present this can be justified in view of the large rate of mass transfer between the two fields, which will tend to draw both to the same temperature. This assumption leads to a great simplification in the numerical solution of the equations, resulting in a reduced computing cost. The user is cautioned to carefully review results for problems where temperature differences between the droplet field and continuous liquid within a single mesh cell may be significant.

2.3 THREE-FIELD CONSERVATION EQUATIONS IN COMPONENT FORM

COBRA-TF has been developed for use with either rectangular Cartesian or subchannel coordinates. This allows a fully three-dimensional treatment in geometries amenable to description in a Cartesian coordinate system. For more complex or irregular geometries the user may select the subchannel formulation (which neglects some of the convective terms in the above equations) or a mixture of the two. The subchannel approach has been used by the COBRA (Ref. 3) codes for bundle thermal-hydraulic analysis. To illustrate the difference between the two formulations, the vapor momentum equation is written out in component form for each case in the paragraphs below. (The momentum equations for the continuous and entrained liquid fields are treated analogously but are not shown.)

2.3.1 Cartesian Coordinates

Let u, v and w denote the x, y and z components of velocity with x being the vertical coordinate. The Cartesian components of the vapor momentum equation are:

x-component (vertical)

$$\frac{\partial}{\partial t}(\alpha_v\rho_v u_v) + \frac{\partial}{\partial x}(\alpha_v\rho_v u_v u_v) + \frac{\partial}{\partial y}(\alpha_v\rho_v u_v v_v) + \frac{\partial}{\partial z}(\alpha_v\rho_v u_v w_v) = -\alpha_v\frac{\partial P}{\partial x} - \alpha_v\rho_v g$$

$$+ \tau'''_{wv_x} - \tau'''_{I_{v\ell_x}} - \tau'''_{I_{ve_x}} + (\Gamma'''U)_x \qquad (2.14)$$

y-component

$$\frac{\partial}{\partial t}(\alpha_v\rho_v v_v) + \frac{\partial}{\partial x}(\alpha_v\rho_v v_v u_v) + \frac{\partial}{\partial y}(\alpha_v\rho_v v_v v_v) + \frac{\partial}{\partial z}(\alpha_v\rho_v v_v w_v) = -\alpha_v\frac{\partial P}{\partial y}$$

$$+ \tau'''_{wv_y} - \tau'''_{I_{v\ell_y}} - \tau'''_{I_{ve_y}} + (\Gamma'''U)_y \qquad (2.15)$$

z-component

$$\frac{\partial}{\partial t}(\alpha_v\rho_v w_v) + \frac{\partial}{\partial x}(\alpha_v\rho_v w_v u_v) + \frac{\partial}{\partial y}(\alpha_v\rho_v w_v v_v) + \frac{\partial}{\partial z}(\alpha_v\rho_v w_v w_v) = -\alpha_v\frac{\partial P}{\partial z}$$

$$+ \tau'''_{wv_z} - \tau'''_{I_{v\ell_z}} - \tau'''_{I_{ve_z}} + (\Gamma'''U)_z \qquad (2.16)$$

2.3.2 Subchannel Coordinates

Fixed transverse coordinates are not used in the subchannel formulation. Instead, all transverse flows are assumed to occur through gaps

(e.g., between fuel rods). Thus, one transverse momentum equation applies to all gaps regardless of the gap orientation. This reduces the number of component momentum equations to only two: vertical and transverse.

Vertical Momentum

$$\frac{\partial}{\partial t}(\alpha_v \rho_v u_v A) + \frac{\partial}{\partial x}(\alpha_v \rho_v u_v u_v A) + \sum_k (\alpha_v \rho_v u_v v_v S)_k$$

$$= -\alpha_v A \frac{\partial P}{\partial x} - \alpha_v \rho_v A g + \tau'''_{wv_x} A - \tau'''_{I_{v\ell_x}} A - \tau'''_{I_{ve_x}} A + (\Gamma'''U)_x A \qquad (2.17)$$

Rate of change of vertical momentum + Rate of vertical momentum efflux by axial convection + Rate of vertical momentum efflux by transverse convection

= Vertical pressure gradient force + Gravity force + Vertical wall shear + Vertical interfacial drag between vapor and continuous liquid + Vertical interfacial drag between vapor and entrained liquid + Vertical momentum exchange due to mass transfer to vapor

Transverse Momentum

$$\frac{\partial}{\partial t}(\alpha_v \rho_v v_v A_k) + \frac{\partial}{\partial L}(\alpha_v \rho_v v_v v_v A_k) + \frac{\partial}{\partial x}(\alpha_v \rho_v v_v u_v A) + \sum_{nk}(\alpha_v \rho_v v_v v_{v_{nk}} S'_{nk})$$

$$= -\alpha_v A_k \frac{\partial P}{\partial L} + \tau'''_{wv_k} A_k - \tau'''_{Iv\ell_k} A_k - \tau'''_{Ive_k} A_k + (\Gamma'''U)_k A_k \qquad (2.18)$$

Rate of change of transverse momentum	+ Rate of transverse momentum efflux by transverse convection	+ Rate of transverse momentum efflux by vertical convection	+ Rate of transverse momentum efflux by orthogonal transverse convection

= Transverse pressure gradient force	+ Transverse wall shear	+ Transverse interfacial drag between vapor and continuous liquid	+ Transverse interfacial drag between vapor and entrained liquid	+ Transverse momentum exchange due to mass transfer to vapor

The following notation has been used in the subchannel equations:

u = vertical velocity

v = transverse velocity

A = vertical flow area of subchannel

A_k = transverse flow area of gap k

S = gap width

S' = orthogonal gap width

L = transverse coordinate

Subscript k refers to gap k.

Subscript nk refers to orthogonal gap nk.

2.3.3 Comparison of Cartesian and Subchannel Equations

The subchannel vertical momentum equation, Equation 2.17, contains derivatives only with respect to x and t, and is already partially finite-differenced. The corresponding Cartesian component equation, Equation 2.14, is still completely in differential form. To compare the two, the Cartesian equation must be put in a form compatible with the subchannel equation.

Figure 2.1 shows a rectangular control volume of length Δx taken from a single subchannel. Expressing Equation 2.14 in partially finite-differenced form for this control volume yields

$$\frac{\partial}{\partial t}(\alpha_v \rho_v u_v)A + \frac{\partial}{\partial x}(\alpha_v \rho_v u_v u_v)A$$

$$+ [(\alpha_v \rho_v u_v v_v)_{y_0+\Delta y} - (\alpha_v \rho_v u_v v_v)_{y_0}]\Delta z$$

$$+ [(\alpha_v \rho_v u_v w_v)_{z_0+\Delta z} - (\alpha_v \rho_v u_v w_v)_{z_0}]\Delta y$$

$$= -\alpha_v \frac{\partial P}{\partial x}A - \alpha_v \rho_v g A + \tau'''_{wv_x} A - \tau'''_{I_{v\ell_x}} A - \tau'''_{I_{ve_x}} A + (\Gamma'''U)_x A \qquad (2.19)$$

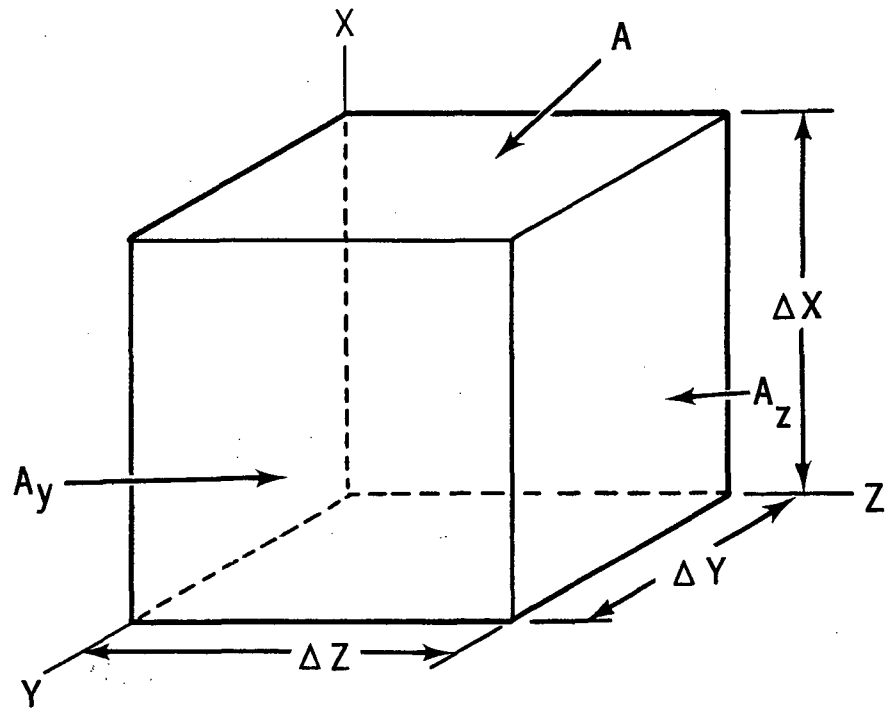

FIGURE 2.1. Control Volume for Cartesian Coordinates

The y- and z-direction vapor momentum equations can be treated in the same fashion. Equation 2.15 becomes

$$\frac{\partial}{\partial t}(\alpha_v \rho_v v_v)A_y + \frac{\partial}{\partial y}(\alpha_v \rho_v v_v v_v)A_y$$

$$+ [(\alpha_v \rho_v v_v u_v)_{x_o+\Delta x} - (\alpha_v \rho_v v_v u_v)_{x_o}]\Delta z$$

$$+ [(\alpha_v \rho_v v_v w_v)_{z_o+\Delta z} - (\alpha_v \rho_v v_v w_v)_{z_o}]\Delta x$$

$$= -\alpha_v \frac{\partial P}{\partial y} A_y + \tau'''_{wv_y} A_y - \tau'''_{Iv\ell_y} A_y - \tau'''_{Ive_y} A_y + (\Gamma'''U)_y A_y \qquad (2.20)$$

and Equation 2.16 becomes

$$\frac{\partial}{\partial t}(\alpha_v \rho_v w_v)A_z + \frac{\partial}{\partial z}(\alpha_v \rho_v w_v w_v)A_z$$

$$+ [(\alpha_v \rho_v w_v u_v)_{x_o+\Delta x} - (\alpha_v \rho_v w_v u_v)_{x_o}]\Delta y$$

$$+ [(\alpha_v \rho_v w_v v_v)_{y_o+\Delta y} - (\alpha_v \rho_v w_v v_v)_{y_o}]\Delta x$$

$$= -\alpha_v \frac{\partial P}{\partial z} A_z + \tau'''_{wv_z} A_z - \tau'''_{Iv\ell_z} A_z - \tau'''_{Ive_z} A_z + (\Gamma'''U)_z A_z \qquad (2.21)$$

The conditions for equivalency between the subchannel and Cartesian momentum equations can be demonstrated with the above equations. Assuming the subchannels are arranged in a rectangular array, equivalence requires

$$\sum_k (\alpha_v \rho_v u_v v_v S)_k = [(\alpha_v \rho_v u_v v_v)_{y_o+\Delta y} - (\alpha_v \rho_v u_v v_v)_{y_o}]\Delta z$$

$$+ [(\alpha_v \rho_v u_v w_v)_{z_o+\Delta z} - (\alpha_v \rho_v u_v w_v)_{z_o}]\Delta y \qquad (2.22)$$

In addition, gaps with unit vectors in the y-direction must have

$$\sum_{nk} (\alpha_v \rho_v v_v v_{v_{nk}} S'_{nk}) = [(\alpha_v \rho_v v_v w_v)_{z_o+\Delta z} - (\alpha_v \rho_v v_v w_v)_{z_o}]\Delta x \qquad (2.23)$$

while gaps with unit vectors in the z-direction must have

$$\sum_{nk} (\alpha_v \rho_v v_v v_{v_{nk}} S'_{nk}) = [(\alpha_v \rho_v w_v v_v)_{y_o+\Delta y} - (\alpha_v \rho_v w_v v_v)_{y_o}]\Delta x \qquad (2.24)$$

The user selects either the three-dimensional Cartesian equations or the subchannel formulation by input. When the subchannel formulation is chosen, the second and fourth terms on the left side of the transverse momentum equation (Equation 2.18) are neglected, yielding the historical form of the subchannel transverse momentum equation. The corresponding components of viscous and turbulent shear stresses are also neglected in the subchannel formulation.

3.0 PHYSICAL MODELS

The conservation equations presented in Section 2.0 are solved numerically on a finite-difference mesh made up of numerous computational cells. Closure of the equation set requires physical models for the mass exchange among the three fields at the phase interfaces, the exchange of momentum at the interfaces, the drag forces at solid boundaries, the viscous stress and turbulence terms in the continuous fields, and the entrainment rate. In addition, property relations for water are needed.

This section contains descriptions of the physical models used in the vessel module of COBRA/TRAC. To facilitate the explanation of the physical models a brief description of the computational cell structure and variable placement for the vessel module is given in Section 3.1. (A more complete discussion of this topic can be found in Volume 2, Numerical Solution Methods.) To implement many of these models the code must define the flow regime. Section 3.2 describes the flow regime map and various parameters used to characterize two-phase flow, such as bubble size and film thickness. The interfacial mass transfer model is explained in Section 3.3, and in Section 3.4 the interfacial drag force is discussed. Section 3.5 contains the wall drag force model. The viscous stress, turbulent stress and turbulent heat flux models are described in Section 3.6. Section 3.7 describes the entrainment models. Fluid thermodynamic properties are discussed in Section 3.8.

3.1 COMPUTATIONAL CELL STRUCTURE

A typical finite-difference mesh is shown in Figure 3.1. The fluid volume is partitioned into a number of computational cells. The equations are solved using a staggered difference scheme in which the velocities are obtained at the mesh cell faces and the state variables such as pressure, density, enthalpy and void fraction are obtained at the cell center.

The mesh cell is characterized by its cross-sectional area, A, its height, Δx, and the width, S, of its connection with adjacent mesh cells.

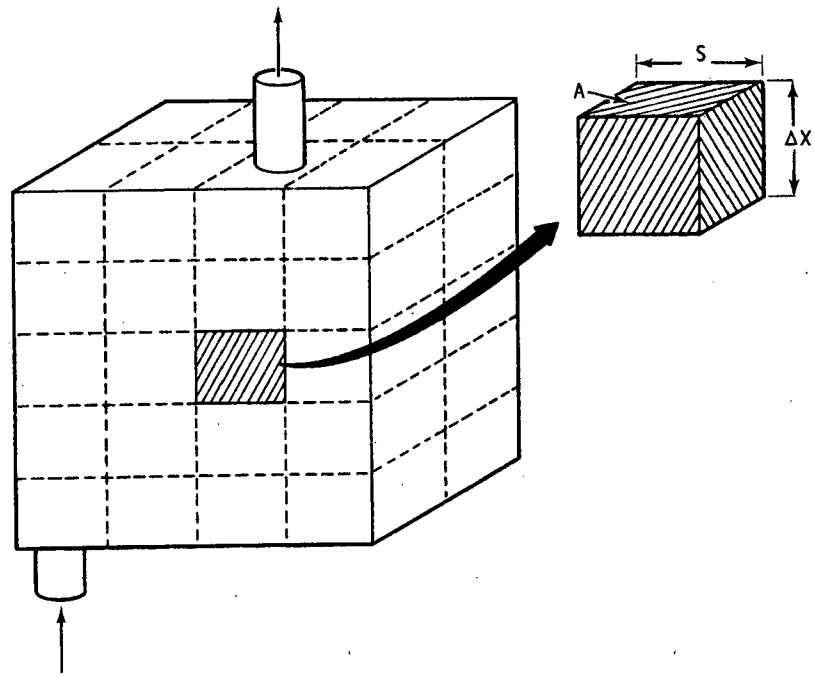

FIGURE 3.1. Mass/Energy Cell

The cell depicted in Figure 3.1 is a mass/energy cell, so named because it is the cell used for solving the scalar continuity and energy equations. The momentum equations are solved on staggered cells that are centered on the scalar mesh cell face. The vertical and transverse momentum cells are shown in Figure 3.2.

3.2 FLOW REGIME SELECTION

Several flow regime maps have been proposed and used by various investigators to describe observed two-phase flow patterns (Ref. 4,5,6). While many of these maps are useful within the range of the data for which they were developed, none can be generally applied to all two-phase flow problems. For example, different flow patterns are observed in a test section containing hot surfaces than are observed in a similar test section having the same mass flux and quality but no hot surfaces. The accurate prediction of exactly which flow regime can be expected under a given set of flow conditions is beyond the current understanding of two-phase flow. With this in mind, the

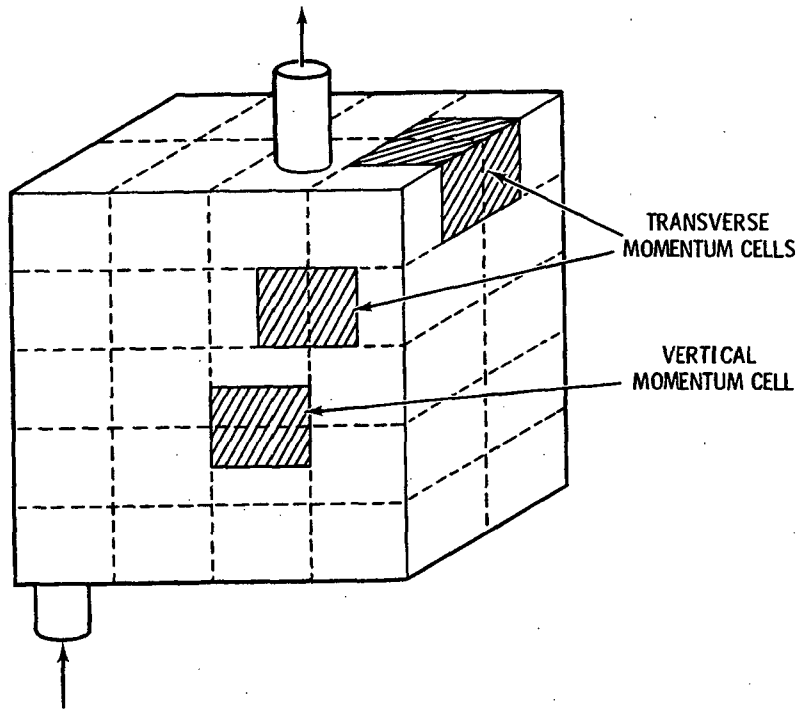

FIGURE 3.2. Vertical and Transverse Momentum Cells

physical basis of existing flow regime maps was studied to develop the most widely applicable and yet simplest flow regime map possible for use in the vessel module in COBRA/TRAC. In this regard, the work by A. E. Dukler (Ref. 6) at the University of Houston pertaining to flow regime transitions in vertical flow has been very helpful.

The flow regime map used in the vessel module of COBRA/TRAC can be divided into two main parts: 1) the logic used to select physical models in the absence of unwetted hot surfaces (e.g., fuel rods) and 2) the logic used when hot surfaces are present. The flow regimes described by the first set of logic are referred to as "normal" flow regimes, while those described by the second set are called "hot wall" flow regimes. Since COBRA-TF was developed for vertical two-phase flow, horizontal flow regimes are not considered.

The physical models used in the numerical solution must be defined for each mesh cell. Therefore, the flow regime must be determined from fluid

properties and flow conditions within each cell or in the immediate surrounding cells. When selecting a mesh size, care must be taken to assure that the local flow regime map renders the correct global flow regime for the problem under consideration.

3.2.1 Normal Flow Regimes

The physical models are selected using the normal flow regime logic if a mesh cell does not contain any solid surface with a temperature greater than 750°F. A schematic of the normal flow regimes is shown in Figure 3.3. The flow regimes considered include dispersed bubbly flow, slug flow, churn-turbulent flow, film flow and film mist flow. The logic for determining the appropriate flow regime and the transitions between flow regimes is illustrated schematically in Figure 3.4.

If the local void fraction is less than 0.2, a dispersed bubbly flow is assumed. The flow consists of spherical or distorted bubbles with radius r_b determined from a critical Weber number criterion as

$$r_b = \min \left(0.5 \frac{We_b \, \sigma}{\rho_\ell |\underline{U}_{v\ell}|^2}, \; 0.5D_H, \; 0.02\right) \tag{3.1}$$

where $\underline{U}_{v\ell} = \underline{U}_v - \underline{U}_\ell$. A critical Weber number of 10 is used.

Bubbles in flashing or boiling two-phase flow will grow around nucleation sites located within the fluid volume or on solid surfaces bounding the fluid volume. The number of such sites is dependent on several factors, including the nature and amount of solid surface as well as the amount of contaminants and noncondensible gases present in the fluid. The surface area for interfacial heat transfer between the superheated liquid and vapor phases is computed using a bubble radius that is the lesser of the two values given by Equation 3.1 and that obtained from a minimum bubble number density:

$$r_b = 0.5 \left(\frac{3}{4} \frac{\alpha_m}{\pi N_b}\right)^{1/3} \tag{3.2}$$

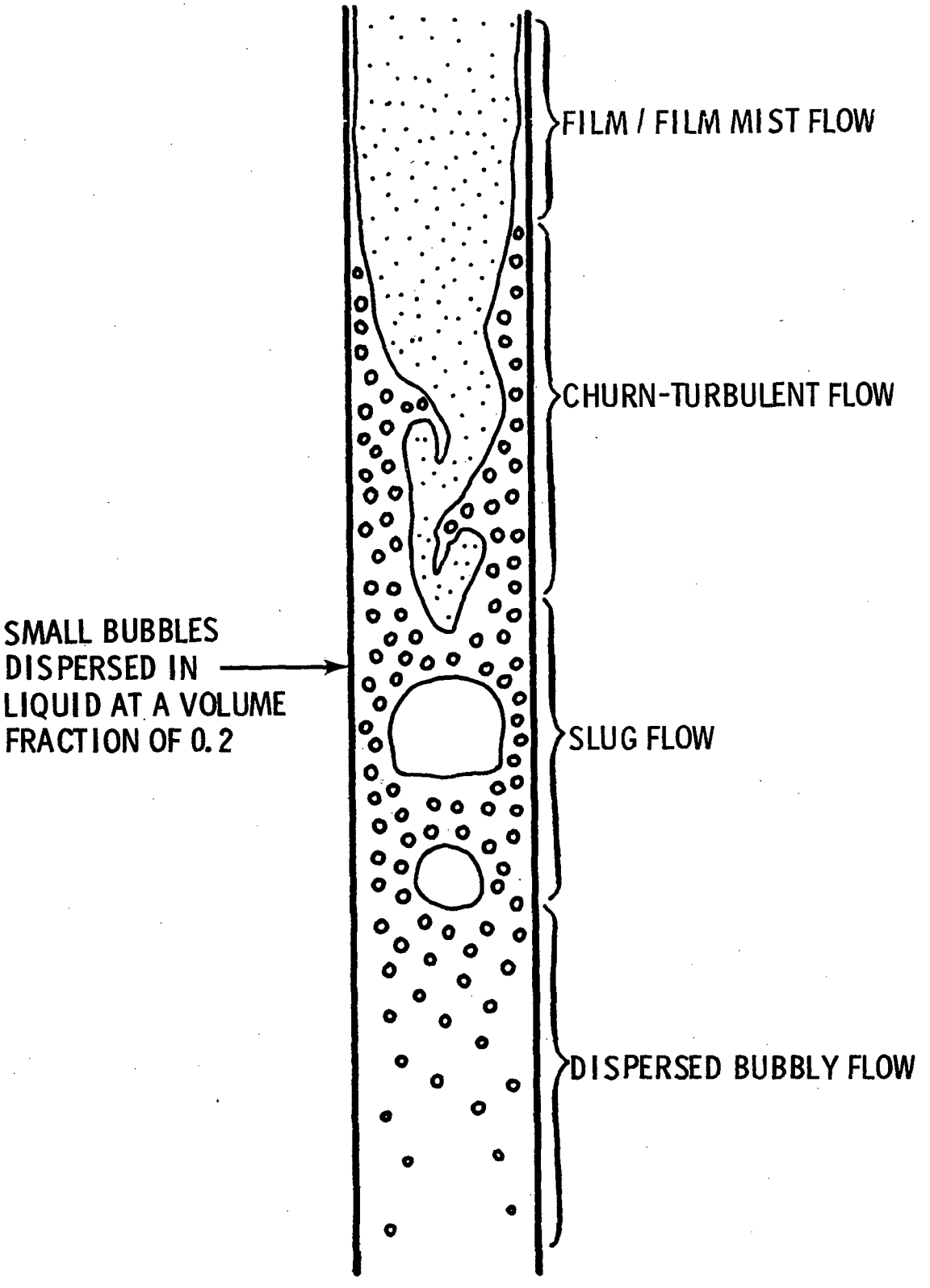

FIGURE 3.3. Normal Two-Phase Flow Regimes

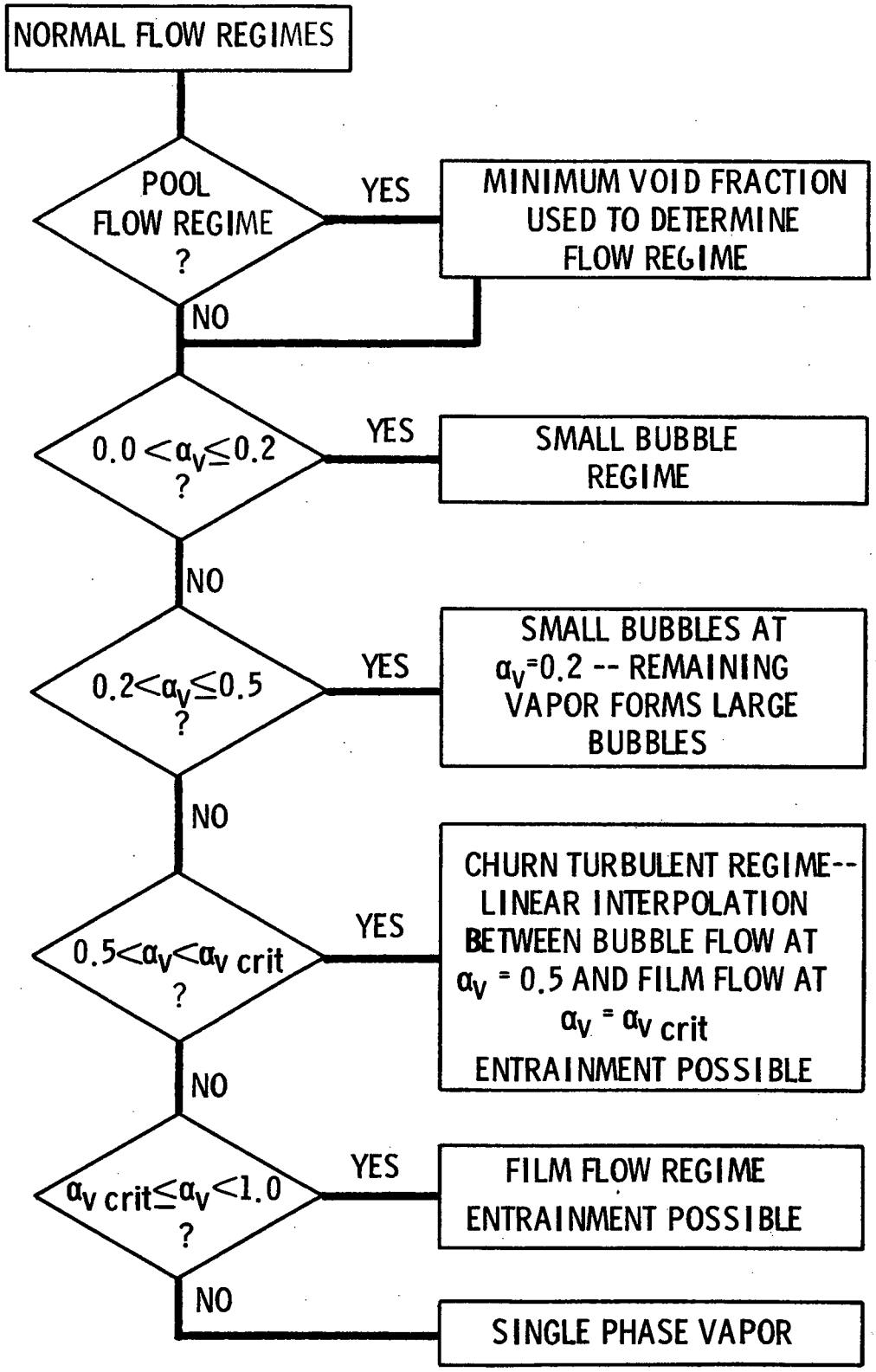

FIGURE 3.4. Normal Flow Regime Selection Logic

where $N_b = 2000/\alpha_m$ and α_m is the larger of α_v and 0.001. N_b is in units of number of bubbles per cubic foot. The dependence of the bubble number density on void fraction is intended to account for coalescence of bubbles as the vapor content of the flow increases. The model yields a bubble radius of 0.1 in. at a void fraction of 0.2. The purpose of this model is to provide an interfacial area for the initiation of flashing. This value is highly dependent on the purity of the water being considered. Better models for this parameter need to be developed, and the model proposed here should only be considered as the current best estimate. The effect of solid surfaces on bubble nucleation is treated separately and will be discussed in more detail in Section 3.3.

It has been observed (Ref. 6) that as the vapor content of the flow increases, a point is reached when the dispersed bubbles become so closely packed that they collide with one another and coalesce into larger bubbles. Although these larger bubbles may be unstable and tend to break up again, the collision frequency is sufficiently high to maintain larger bubbles. This is the beginning of the transition to slug flow. It is assumed that this process begins at a void fraction of 0.2. For void fractions above 0.2, the continuous liquid is assumed to contain small dispersed bubbles at a volume fraction of 0.2 while the remainder of the vapor forms a larger bubble. The large bubble will grow with increasing vapor flow until it reaches the maximum allowable bubble size, then another larger bubble will begin forming. (See Figure 3.3.) The radius of the large bubble is given by

$$r_b = \left[\frac{3}{4\pi} (\alpha_v - 0.16\ \alpha_\ell) \cdot (\text{Volume of cell})\right]^{1/3} \qquad (3.3)$$

and is limited to half the hydraulic diameter of the flow channel.

As the vapor content of the flow increases, the large bubbles will begin to coalesce, and a transition into churn-turbulent and then film flow will occur. It is assumed that this begins to occur at a void fraction of 0.5. The churn-turbulent flow regime is assumed until a stable liquid film is

achieved. The void fraction at which a stable liquid film will exist depends on the flow channel size and the vapor velocity. The critical void fraction is determined from a force balance between the disruptive force of the pressure gradient over the crest of waves on the film and the restraining force of surface tension. The resulting expression for the critical film thickness is (Ref. 7)

$$\delta_{crit} = \frac{C_1 \sigma}{\rho_v |\underline{U}_{v\ell}|^2} \tag{3.4}$$

The constant C_1 contains the effects of wave shape and amplitude on the surface tension force and pressure force, and the relationship between the wave amplitude and film thickness. If the wave amplitude is assumed to be about four times the film thickness, the value of C_1 should be about 0.5. Comparison of the model with the onset of entrainment data of Dukler (Ref. 8) indicated that a C_1 of 0.5 is a reasonable value. The film thickness in a flow channel is given by

$$\delta = \frac{\alpha_\ell D_H}{4} \tag{3.5}$$

Substituting this into the equation for critical film thickness gives the expression for the critical void fraction for stable film flow:

$$\alpha_{v_{crit}} = 1.0 - 4.0\ C_1 \sigma / \rho_v |\underline{U}_{v\ell}|^2\ D_H \tag{3.6}$$

The critical void fraction is limited to a minimum value of 0.8, the value at which waves can be expected to bridge across the flow channel and cause a transition to churn flow. The interfacial geometry of the churn-turbulent flow is treated as a linear interpolation between bubble flow and film flow.

The flow is considered to consist entirely of bubbly flow as described above at a void fraction of 0.5 and entirely of film flow at the critical void fraction. Entrainment of liquid from the continuous liquid field into the droplet field is allowed in this flow regime. The entrainment rate is interpolated between 0.0 at a void fraction of 0.5 to the full value given by the entrainment correlations at the critical void fraction. This provides a smooth transition into film or film mist flow. It should be noted that as long as the vapor velocity is sufficiently high to carry liquid drops away, the film mist flow regime will be maintained. This is consistent with Dukler's explanation for the transition to film flow. This transition is predicted by the code based on the models used for the entrainment rate and interfacial drag between the vapor and drops.

Additional checks are made to assure that the flow regimes assumed locally are consistent with the global flow pattern. This is done by checking for a large void fraction difference between two mesh cells. If one mesh cell has a void fraction greater than 0.6 and the difference in void fraction between the two cells is greater than 0.4, then it is assumed that a liquid pool or froth front exists, and the larger void fraction is used to determine the flow regime and physical models in the pool. If a cell has a void fraction greater than 0.6 and the difference in void fraction between it and the cell above it is greater than 0.4, then an inverted pool is assumed, and the lower void fraction is used to determine the flow regime and physical models. This inverted pool regime can occur in the downcomer of a pressurized water reactor during emergency core coolant injection. The size of the bubbles formed as the vapor penetrates the inverted pool interface is assumed to be the larger of the Weber number-controlled bubble radius and an instability-controlled bubble radius given by

$$r_b = \frac{\sigma}{\rho_v u_R^2} \tag{3.7}$$

where u_R is the vapor vertical velocity below the interface minus the liquid vertical velocity at the interface.

The same kind of check is made in the transverse directions. The lower void fraction is again used to determine flow regime and physical models. In all other cases the void fraction of the staggered momentum mesh cell is used to determine flow regimes and physical models in that cell. Physical models required for the continuity mesh cells (i.e., interfacial heat transfer coefficients and areas) are taken to be the average of two adjacent momentum mesh cell values.

A check is made in the bubbly flow regimes to determine if vapor is concentrated at the walls of the flow channel as a result of vapor generation due to wall heat transfer. The vertical vapor velocity resulting from vapor generation at the heat transfer surface is given by

$$u_\Gamma = \min \left(\frac{\Gamma''' \, \Delta x}{\alpha_v \rho_v} , \frac{Q''' _{w\ell} \, \Delta x}{h_{fg} \alpha_v \rho_v} \right) \tag{3.8}$$

where Δx is the vertical length increment of the mesh. This expression assumes that all vapor generated within the cell leaves vertically. The bubble rise velocity relative to the liquid is given by (Ref. 9)

$$u_{BR} = 1.414 \left(\sigma g \Delta \rho / \rho_\ell^2 \right)^{1/4} / (1 - \alpha_v) \tag{3.9}$$

If vapor is being generated at the wall at a faster rate than it can be carried away by the flow, i.e., if $(u_\Gamma - u_\ell) > u_{BR}$, then the vapor is assumed to be concentrated at the wall. The interfacial drag model computes a smaller drag coefficient than would be possible for bubbles dispersed uniformly in the liquid.

3.2.2 Hot Wall Flow Regimes

Effective cooling of the core is lost during the blowdown stage of a loss-of-coolant accident in light water reactors, and the core is subjected to a nearly adiabatic heatup. The steam environment surrounding the rods does

not provide sufficient heat transfer from the cladding to remove heat being added from stored energy in the fuel pellets and from fission-product decay. This temperature excursion is halted by the injection of emergency core cooling (ECC) water into the reactor vessel.

As the cooling water enters the core, it contacts the hot rods and begins to re-establish effective cooling of the core. It is during this period that the temperature excursion of the cladding is turned around. Complex hydrodynamic and heat transfer processes take place during this phase of the transient as a result of saturated or subcooled water coming into contact with the high-temperature cladding. When the cladding temperature is above the surface rewetting temperature, a film boiling heat transfer mechanism will be established. This may correspond to either a dispersed flow regime or an inverted-annular, two-phase flow regime, depending upon the liquid content of the flow and the vapor velocity. As the cladding temperature is reduced because of the cooling provided by film boiling, the cladding will enter a transition boiling and finally a nucleate boiling regime. The temperature will fall below the surface rewet temperature, and the surface will quench. Heat transfer from the rod will then take place in the form of nucleate boiling or single-phase liquid heat transfer, depending on the subcooling and flow rate of the liquid entering the core. The rate at which liquid will enter the core during bottom reflood is limited by the available driving head provided by the liquid in the downcomer and the flow resistance through the broken hot leg. During top reflood, the rate liquid will enter the core is controlled by the countercurrent flow limitation.

High flow rates of superheated vapor result from the steam generated as the rods are quenched. Vapor velocities are usually high enough to entrain significant fractions of the liquid in the form of drops. This droplet entrainment is beneficial since it enhances heat transfer downstream of the quench front by desuperheating the steam and contributing to the total steam flow rate as the drops evaporate.

The "hot wall" flow regimes are used when a mesh cell contains a solid surface with a temperature greater than 750°F. These flow regimes describe

the hydrodynamics of the highly nonhomogenous, thermal nonequilibrium, two-phase flow encountered during reflood. The "hot wall" flow regimes include subcooled inverted annular flow, saturated liquid chunk flow, dispersed drop-vapor flow, falling film flow and top deluge.

The normal direction for reflood is from the bottom of the core, but a top quench front is assumed to exist if the mesh cell above the cell with a hot wall contains no surfaces with a temperature greater than T_{sat} + 75°F. If the void fraction is greater than 0.8, a falling film flow regime is assumed in the cell containing the top quench front; otherwise a top deluge is assumed. In the deluge regime the flow is assumed to consist of large liquid chunks having diameters equal to the flow channel hydraulic diameter. Droplet deposition and entrainment is allowed in the falling film regime.

An inverted annular flow regime is assumed during bottom reflood if the continuous liquid phase is subcooled. This regime consists of a liquid core surrounded by a vapor film. If the liquid is saturated, then a liquid chunk flow regime is assumed in which the flow is considered as liquid drops surrounded by vapor. Entrainment of liquid into the entrained droplet field is allowed in this flow regime, permitting a transition to dispersed flow based on the physical models for the entrainment rate and droplet/vapor interfacial drag. The deposition and breakup of droplets on grid spacers is also considered. The hot wall flow regimes are illustrated in Figure 3.5, and Figure 3.6 shows the selection logic.

3.3 INTERFACIAL MASS TRANSFER

The model for interfacial mass transfer is obtained from the energy jump condition, Equation A.37, by neglecting the mechanical terms and averaging. This yields

$$\Gamma''' = \frac{-q'''_{I_\ell} - q'''_{I_v}}{h_{fg}} \tag{3.10}$$

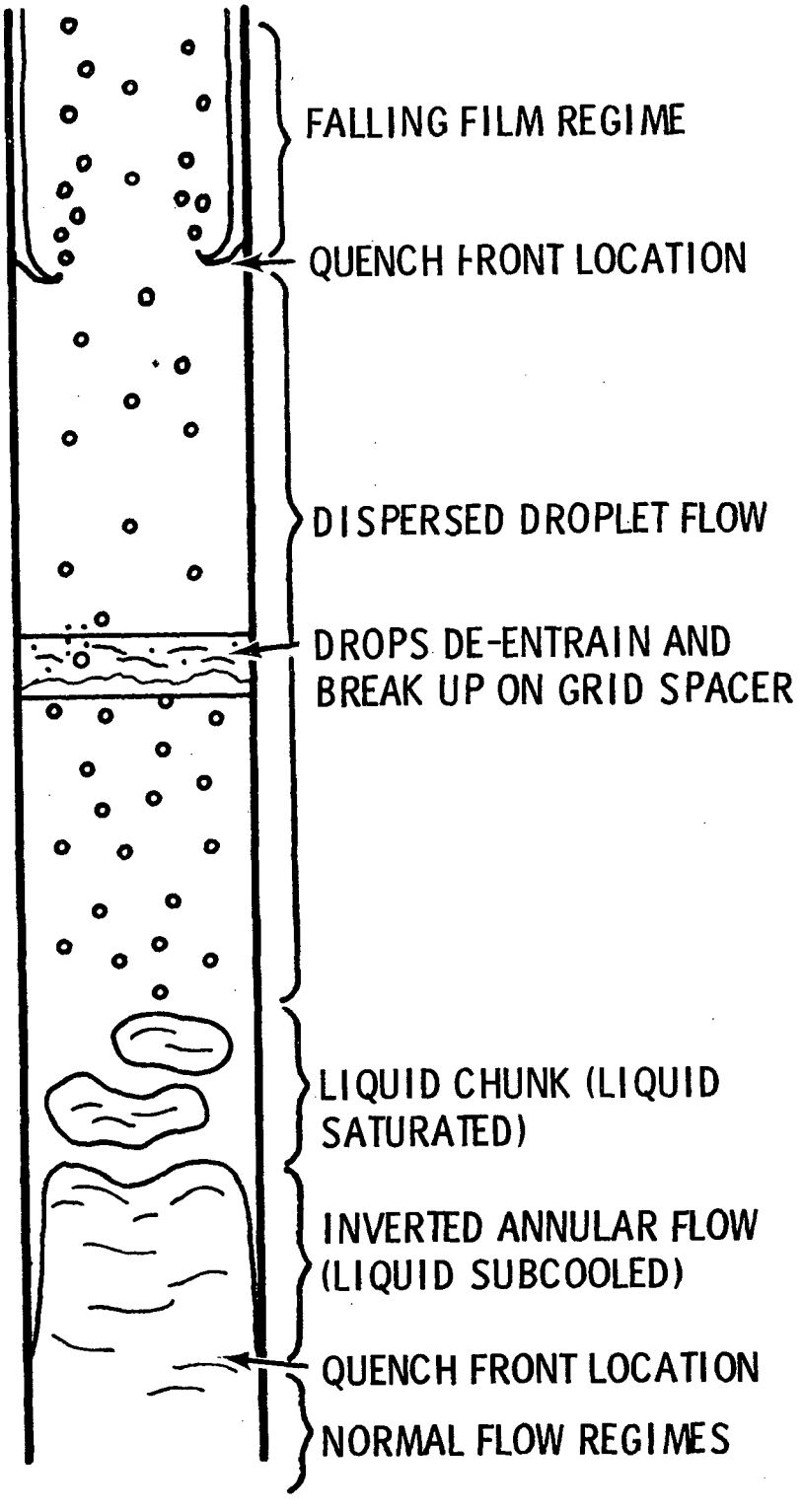

FIGURE 3.5. Hot Wall Flow Regimes

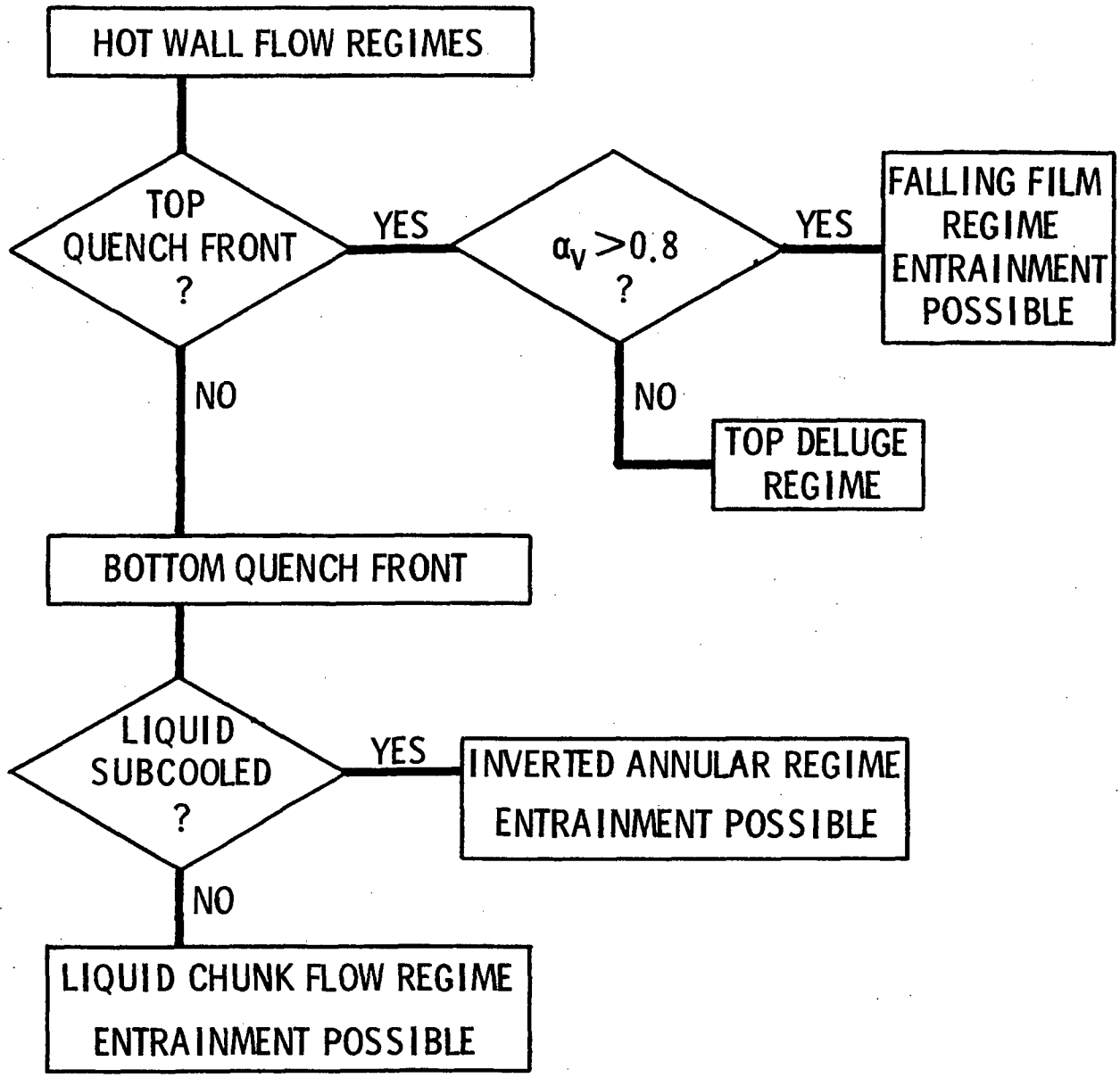

FIGURE 3.6. Hot Wall Flow Regime Selection Logic

The interfacial heat transfer, q_I''', for phase k is given by

$$q_{I_k}''' = H\, A_I'''\, (T_s - T_k) \tag{3.11}$$

where A_I''' is the average interfacial area per unit volume and H is a surface heat transfer coefficient. It is convenient to divide the vapor generation into four components, two for each phase, depending on whether the phase is superheated or subcooled. The total vapor generation rate is given by the sum of these components. For example, Γ_{SHL}''', the vapor generation per unit volume resulting from superheated liquid, is given by

$$\Gamma_{SHL}''' = \frac{H_{SHL} A_I'''\, (h_\ell - h_f)}{C_{p\ell}\, h_{fg}} \tag{3.12}$$

Analogous relations hold for subcooled liquid (SCL) superheated vapor (SHV) and subcooled vapor (SCV). The fraction (η) of total vapor generation coming from the entrained liquid is given by

$$\eta = \min\left[\frac{\alpha_e}{1-\alpha_v},\ \left(1.0 - \frac{Q_{w\ell}'''}{\Gamma'''\, h_{fg}}\right)\right], \text{ for vaporization}$$

and

$$\eta = \left(\frac{\alpha_e}{1-\alpha_v}\right), \text{ for condensation.}$$

The interfacial area per unit volume, A_I''', is based on flow regime, as are the heat transfer coefficients, H. Correlations for the various heat transfer coefficients are given in Table 3.1, and models for interfacial area for each flow regime are given in Table 3.2. The various Reynolds numbers used in Table 3.1 are defined as follows:

TABLE 3.1. Interfacial Heat Transfer Coefficients

Mode of Heat Transfer	Correlation (Btu/hr-ft^2-°F)		Flow Regime
H_{SHV}	1.0×10^4 (a)		Bubble
	$(2.0 + 0.74\ Re_v^{0.5}\ Pr_v^{1/3}) \frac{k_v}{D_H}$	(Ref. 10)	Large Bubble
	$\frac{f_I}{2} \rho_v\ C_{p_v} \lvert \underline{U}_{v\ell} \rvert Pr_v^{-2/3}$		Film
	$(2.0 + 0.74\ Re_d^{0.5}\ Pr_v^{1/3}) \frac{k_v}{2r_d}$	(Ref. 10)	Drop
	$(2.0 + 0.74\ Re_v^{0.5}\ Pr_v^{1/3}) \frac{k_v}{D_H}$		Liquid chunk, inverted annular
H_{SCV}	1.0×10^4 (a)		All regimes

(a) Constant large value used to drive phase to equilibrium

TABLE 3.1. (continued)

Mode of Heat Transfer	Correlation (Btu/hr-ft^2-°F)		Flow Regime
H_{SHL}	$\frac{1}{\sqrt{\pi}} \left(\frac{k_\ell \lvert \underline{U}_{v\ell} \rvert}{r_b} \rho_\ell C_{p\ell}\right)^{1/2}$		Bubble
	1.0×10^5 (a)		Large bubble, liquid chunk and inverted annular
	The maximum of:		
	$1.925\ \rho_\ell C_{p_\ell} \lvert \underline{U}_\ell \rvert / (Re_f^{2/3}\ Pr_\ell^{2/3})$		Film (b)
	for $Re_f < 1000$		
	$0.2701 \rho_\ell C_{p_\ell} \lvert \underline{U}_\ell \rvert / (Re_f^{0.38}\ Pr_\ell^{2/3})$		
	for $1000 \leq Re_f$		
	and: $2.0 k_\ell / \delta$		
	$C \frac{\pi^2}{3} \frac{k_\ell}{r_d}$ $(C = 2.7)$	(Ref. 11)	Drop

(b) From Colburn analogy using friction factors of Hughmark (Ref. 13)

TABLE 3.1. (continued)

Mode of Heat Transfer	Correlation (Btu/hr-ft^2-°F)		Flow Regime
H_{SCL}	$\frac{1}{\sqrt{\pi}} \left(\frac{k_\ell \lvert U_{v\ell} \rvert}{r_b} \rho_\ell C_{p_\ell}\right)^{1/2}$	(Ref. 12)	Bubble, large bubble
	$1.925\ \rho_\ell C_{p_\ell} \lvert U_\ell \rvert / (Re_f^{2/3}\ Pr_\ell^{2/3})$		Film (b)
	for $Re_f < 1000$		
	$0.2701\ \rho_\ell C_{p_\ell} \lvert U_\ell \rvert / (Re_f^{0.38}\ Pr_\ell^{2/3})$		
	for $1000 \leq Re_f$		
	$C \frac{\pi}{3} \frac{k_\ell}{r_d}$ $(C = 2.7)$	(Ref. 11)	Drop, liquid chunk, inverted annular

TABLE 3.2. Interfacial Heat Transfer Area Per Unit Volume

Flow Regime	Interfacial Area, A_I'''
Bubble	$N_b \, 4 \pi r_b^2$ (a)
Film	$\sqrt{\alpha_v} \, P_w/A$
Liquid Chunk	$N_d \, \pi \, D_H^2$ (b)
Inverted Annular	$\sqrt{\alpha_\ell} \, P_w/A$
Drop	Drop interfacial area transport equation (Equations 3.18 and 3.19)

(a) $$N_b = \frac{\alpha_v}{\frac{4\pi}{3} r_b^3}$$

(b) $$N_d = \frac{\alpha_\ell}{\frac{\pi \, D_H^3}{6}}$$

$$Re_v = \frac{D_H \rho_v |\underline{U}_{v\ell}|}{\mu_v}$$

$$Re_b = \frac{2r_b \rho_\ell |\underline{U}_{v\ell}|}{\mu_{m_b}} \quad , \quad \mu_{m_b} = \mu_\ell (1 - \alpha_v)^{-2.5} \frac{(\mu_v + 0.4\ \mu_\ell)}{(\mu_v + \mu_\ell)}$$

$$Re_d = \frac{2r_d\ \rho_v |\underline{U}_{ve}|}{\mu_{m_b}} \quad , \quad \mu_{m_b} = \mu_v \alpha_v^{-2.5} \frac{(\mu_\ell + 0.4\ \mu_v)}{(\mu_v + \mu_\ell)}$$

$$Re_f = \frac{D_H\ \rho_\ell |\underline{U}_\ell|}{\mu_\ell} \tag{3.13}$$

The friction factor, f_I, is given by Wallis (Ref. 14)

$$f_I = 0.005\ (1 + 75\ \alpha_\ell) \tag{3.14}$$

The smaller bubble size of the one given by the Weber number criterion (Equation 3.1) and that given by the bubble number density (Equation 3.2) is used to compute the area for superheated liquid interfacial heat transfer. In addition, nucleation on solid surfaces is accounted for by an additional interfacial heat transfer coefficient and area given by:

$$(H_{SHL} A_I''')_{WALL} = \frac{k_\ell}{D_H} (8.0 + 0.023\ Re_\ell^{0.8}\ Pr_\ell^{0.4}) \frac{P_w}{A} \tag{3.15}$$

Here the interfacial area has been assumed to be equal to the surface area of the solid structure within the mesh cell, and the interfacial heat transfer coefficient is given by the Dittus-Boelter correlation (Ref. 15). A more general correlation for nucleation on solid surfaces is needed and will replace Equation 3.15 should one become available.

The effect of grid spacers on the superheated vapor interfacial heat transfer during reflood is added to the interfacial heat transfer between drops and vapor. Experimental data (Ref. 16) has indicated that grid spacers have a significant effect on desuperheating the vapor flowing through the grid spacer. This effect is important, as the reduced vapor temperature enhances the rod heat transfer in the upper portions of the bundle, resulting in lower peak cladding temperatures. This effect has been accounted for in two ways. First, as droplets pass through the grid spacer, a certain fraction of them will hit the grid structure. Since the grid has no internal heat generation, the droplets rewet the grid early in the reflood transient, forming a liquid film on the grid. This wet grid acts as a large area for interfacial heat transfer between the liquid film and the superheated vapor. The interfacial heat transfer coefficient is assumed to be given by the Dittus-Boelter (Ref. 15) correlation, and the interfacial area is assumed to be equal to the surface area of the grid spacer,

$$(HA''')_{GRID} = \frac{k_\ell}{D_H} (0.023\ Re_v^{0.8}\ Pr_v^{0.3})\ 0.222\ P_w/A\Delta X \tag{3.16}$$

The factor 0.222 was determined by assuming a rod diameter of 0.422 in., a rod pitch of 0.563 in., and a grid spacer height of 1.57 in. (These values are typical for PWRs.) The second major effect of grid spacers is that as the droplets hit the grid, the impact creates a splatter of smaller droplets which rapidly evaporate. This has been accounted for by increasing the droplet interfacial area by 55% in mesh cells containing grids. (This value is based on FLECHT/SEASET data.)

When a combination of flow regimes exist within a mesh cell, the total interfacial heat transfer coefficient times area is the sum of the HA_I''' for all regimes. For example, if the flow consists of small and large bubbles, the total is given as

$$H_{SHL}A_I''' = (H_{SHL}A_I''')_{\substack{SMALL \\ BUBBLES}} + (H_{SHL}A_I''')_{\substack{LARGE \\ BUBBLES}} \tag{3.17}$$

The same is true for liquid film and drops, etc.

The total interfacial area of drops within a mesh cell is determined by solving an interfacial area concentration transport equation as follows:

$$\frac{\partial A''_{I_d}}{\partial t} + \nabla \cdot (A''_{I_d} \underline{U}_e) = \frac{3\, S'''}{\rho_\ell r_s} + S_r \tag{3.18}$$

Rate of change of interfacial area concentration	+	Rate of efflux of interfacial area concentration	=	Rate of interfacial area generation due to entrainment and deposition of drops	+	Rate of interfacial area concentration change due to phase change

Once a drop is formed, no further breakup is assumed to occur, and the drops change size only as a result of condensation, vaporization or new drop formation. The drop size is easily computed from the interfacial area as

$$r_d = 3\, \alpha_e / A''_{I_d} \tag{3.19}$$

The expression for r_s, the drop formation size, is dependent on the conditions under which the drop is formed, and is discussed with the entrainment model in Section 3.7.

3.4 INTERFACIAL DRAG FORCE

The average interfacial drag force per unit volume between the vapor and continuous liquid is defined as a function of relative velocity,

$$\underline{\tau}''_{I_{v\ell}} = K_{I_{v\ell}} \underline{U}_{v\ell} \tag{3.20}$$

The drag force between the vapor and entrained liquid is also a function of the relative velocities of the two fields,

$$\underline{\tau}''' _{I_{ve}} = K_{I_{ve}} \underline{U}_{ve} \tag{3.21}$$

The interfacial friction coefficients, K_I, are dependent on flow regime and are defined as follows:

Bubble

$$K_{I_{v\ell}} = 0.375 \frac{C_{D_b}}{r_b} \alpha_v \rho_\ell |\underline{U}_{v\ell}| \tag{3.22}$$

Drop

$$K_{I_{ve}} = 0.375 \frac{C_{D_d}}{r_d} \alpha_e \rho_v |\underline{U}_{ve}| \tag{3.23}$$

Film

$$K_{I_{v\ell}} = 2.0 \frac{f_I}{D_H} \sqrt{\alpha_v}\ \rho_v |\underline{U}_{v\ell}| \tag{3.24}$$

Inverted Annular

$$K_{I_{v\ell}} = 2.0 \frac{f_I}{D_H} \sqrt{\alpha_\ell}\ \rho_v |\underline{U}_{v\ell}| \tag{3.25}$$

Expressions for the bubble and drop drag coefficients, C_{D_b} and C_{D_d}, are discussed by Ishii (Ref. 9). The drag coefficients are Reynolds number dependent and closely related to the drag coefficients for single bubbles and drops in an infinite medium. The drag coefficient for a single bubble in an infinite liquid medium is shown in Figure 3.7. The bubble is considered to behave as a solid sphere in the viscous regime. At higher Reynolds numbers the bubble is characterized by a distorted shape and irregular motion. In this distorted particle regime the drag coefficient increases with Reynolds number. As the Reynolds number further increases, the bubble becomes spherical-cap shaped and the drag coefficient becomes constant.

As discussed by Ishii, in the viscous regime the drag coefficient of a single particle in a multiparticle system may be assumed to have the same functional form as that of single particle in an infinite medium provided that the Reynolds number is computed using the appropriate mixture viscosity. Therefore, in the viscous regime the drag coefficient on a bubble is given by

$$C_{D_b} = \frac{24}{Re_b} (1.0 + 0.1\ Re_b^{0.75}) \tag{3.26}$$

where Re_b is defined as in Equation 3.13. The mixture viscosity is used in Re_b because a particle moving in a multiparticle system experiences a greater resistance than a single particle in an infinite medium. As it moves it must not only deform the fluid but the neighboring particles as well. The effect is seen by the particle as an increased viscosity.

In the distorted particle regime it is again assumed that the drag coefficient for a particle in a multiparticle system is the same as that of a single particle in an infinite medium with the Reynolds number based on a mixture viscosity. In addition, it is assumed that churn-turbulent flow always exists in the distorted particle regime. Under these conditions a particle tends to move in the wake caused by other particles. Therefore, the velocity used in the drag coefficient and Reynolds number should be the drift velocity, $\underline{U}_{vj} = (1 - \alpha_v)\ \underline{U}_{v\ell}$. The drag coefficient in the churn-turbulent regime is then

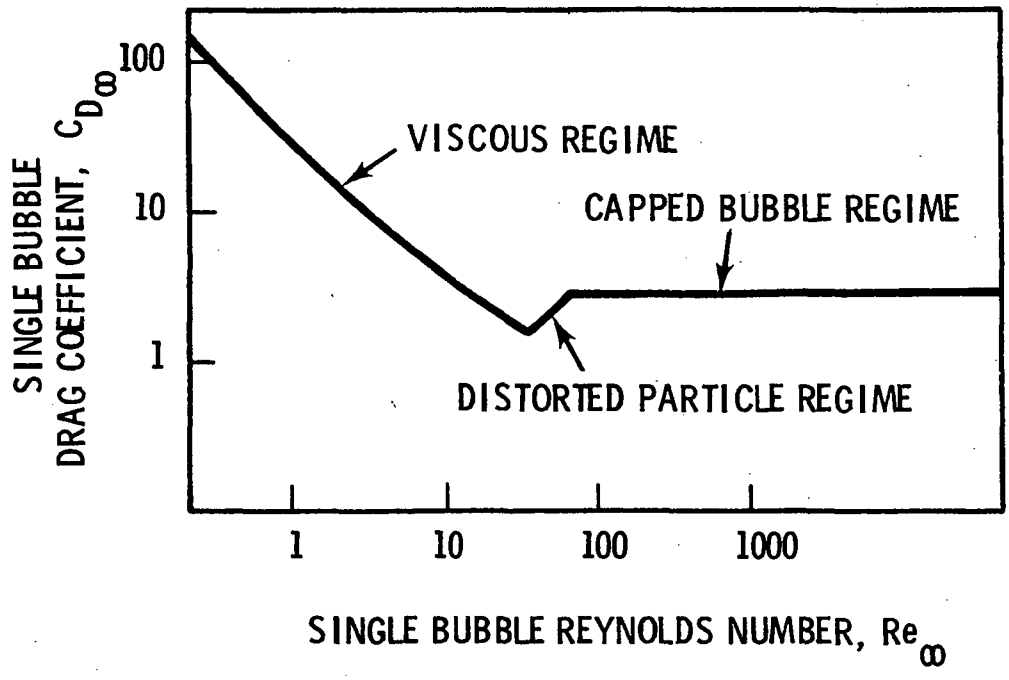

FIGURE 3.7. Single-Bubble Drag Coefficient

$$C_{D_b} = \frac{\sqrt{2}}{3} N_\mu \, Re'_b \, (1 - \alpha_v)^2 \tag{3.27}$$

where

$$N_\mu = \frac{\mu_\ell}{\left(\rho_\ell \sigma \sqrt{\frac{\sigma}{g(\rho_\ell - \rho_v)}}\right)^{1/2}} \tag{3.28}$$

$$Re'_b = 2 \, r_b \, \rho_\ell (1 - \alpha_v) |\underline{u}_{v\ell}| / \mu_m \tag{3.29}$$

and

$$\mu_m = \frac{\mu_\ell}{(1 - \alpha_v)} \tag{3.30}$$

The $(1 - \alpha_v)^2$ in the expression for the drag coefficient results from using the drift velocity to compute the drag force.

Churn-turbulent flow is also assumed for the cap bubble regime where

$$C_{D_b} = \frac{8}{3} (1 - \alpha_v)^2 \tag{3.31}$$

For the large-bubble flow regime, Equation 3.26 is assumed to apply down to the limit of Newton's regime where the drag coefficient for a single solid sphere becomes constant at a value of 0.45. Within Newton's regime the large bubbles are assumed to move with respect to the average volumetric flux, and therefore

$$C_{D_b} = 0.45 (1 - \alpha_v)^2 \tag{3.32}$$

The viscous regime is assumed for drops, and the drag coefficient has the same form as that for bubbles except the Reynolds number is Re_d, as defined by Equation 3.13. The drop drag coefficient is limited to a minimum value of 0.45.

The friction factor, f_I, for film flow is dependent on whether the film is stable or unstable. It has been observed experimentally that the onset of film instability causes a sudden increase in system pressure drop. This is a result of increased roughness of the liquid film caused by large, unstable waves. While the film friction factor for unstable film flow in large tubes has been studied, the correlation does not extrapolate to hydraulic diameters typical of LWR fuel bundles. Henstock and Hanratty (Ref. 17) have correlated

a large amount of cocurrent and countercurrent film flow data; however, their correlation does not predict the sudden increase in pressure drop at the onset of instability.

Until further information becomes available, it has been assumed that the film friction factor for stable films is given by the correlation recommended by Wallis (Ref. 14), Equation 3.14. This expression is also used for unstable films when solving the transverse momentum equations. When solving the vertical momentum equations, the friction factor for unstable films is taken to be the larger of either Henstock and Hanratty's correlation or five times the value of f_I given by the Wallis correlation.

Henstock and Hanratty's correlation is of the form,

$$f_I = f_s \{1 + 1400F [1 - \exp (- \frac{1}{G} \frac{(1 + 1400F)^{3/2}}{13.2F}]\} \tag{3.33}$$

where

$$G = \frac{\rho_\ell \, g \, D_H}{\rho_v \, u_v^2 \, f_s}$$

$$F = \frac{m^+}{Re_v^{0.9}} \frac{\mu_\ell}{\mu_v} \sqrt{\frac{\rho_v}{\rho_\ell}}$$

$$m^+ = [(0.707 \, Re_\ell^{0.5})^{2.5} + (0.0379 \, Re_\ell^{0.9})^{2.5}]^{0.40}$$

$$f_s = 0.046 \, Re_v^{-0.20} \tag{3.34}$$

The multiplication factor of five was obtained from the observed difference between the pressure drop characteristics for stable films and that for unstable films (Ref. 8). This can be replaced by a more appropriate correlation, should one become available. The friction factor for inverted annular flow is assumed to be a constant,

$$f_I = 0.01 \tag{3.35}$$

until more information is available.

An additional interfacial drag force is calculated for interfaces that occur at mesh cell boundaries. These interfaces are detected by changes in void fraction between adjacent cells, and can occur on either horizontal or vertical cell boundaries. For two cells, i and j, connected to each other by a vertical or transverse connection, an intercell interface is assumed when $\alpha_i > 0.8$ and $\alpha_j < 0.6$, so that cell i is on the vapor side of the interface and cell j is on the liquid side. The drag force is a function of the difference between the vapor velocity in cell i and the liquid velocity in cell j, and is given by

$$F_{I_x} = f_I \frac{1}{2} \rho_v |u_{v_i} - u_{\ell_j}| (u_{v_i} - u_{\ell_j}) A_{I_x} \tag{3.36}$$

for the vertical direction and

$$F_{I_y} = f_I \frac{1}{2} \rho_v |v_{v_i} - v_{\ell_j}| (v_{v_i} - v_{\ell_j}) A_{I_y} \tag{3.37}$$

for the transverse direction. In these equations A_{I_x} and A_{I_y} are the appropriate intercell areas. A friction factor of 0.08 is assumed and has given good results. The intercell interfacial force is added to the liquid momentum equation in cell j (on the liquid side of the interface) and subtracted from the vapor momentum equation in cell i (on the vapor side).

3.5 WALL DRAG FORCE

The wall drag forces per unit volume on each phase, $\underline{\tau}''' _{w\ell}$, $\underline{\tau}''' _{wv}$ and $\underline{\tau}''' _{we}$, are defined as functions of the phase velocities

$$\underline{\tau}''' _{w\ell} = - K_{\ell} \underline{U}_{\ell} \tag{3.38}$$

$$\underline{\tau}''' _{wv} = - K_{v} \underline{U}_{v} \tag{3.39}$$

$$\underline{\tau}''' _{we} = - K_{e} \underline{U}_{e} \tag{3.40}$$

The drag coefficients, K_{ℓ}, K_{e} and K_{v}, contain both the local form loss and the friction factor and are defined as

$$K_{\ell} = \left(\frac{f_{\ell}}{2D_{H}} + \alpha_{\ell} \frac{K}{\Delta x}\right) \rho_{\ell} |\underline{U}_{\ell}| \tag{3.41}$$

$$K_{v} = \left(\frac{f_{v}}{2D_{H}} + \alpha_{v} \frac{K}{\Delta x}\right) \rho_{v} |\underline{U}_{v}| \tag{3.42}$$

$$K_{e} = \alpha_{e} \frac{K}{\Delta x} \rho_{\ell} |\underline{U}_{e}| \tag{3.43}$$

The friction factors for single-phase liquid flow, f_{ℓ}, and single-phase vapor flow, f_{v}, are computed from laminar or modified Blasius correlations based on the single-phase liquid or vapor Reynolds number.

$$f_{k} = \begin{cases} 64.0/Re_{k} & \text{laminar flow} \\ 0.0055 + 0.55\ Re_{k}^{-1/3} & \text{turbulent flow} \end{cases} \tag{3.44}$$

The vapor friction factor, f_v, is set to zero for the bubbly, film and single-phase liquid flow regimes. The liquid friction factor, f_ℓ, is set to zero for the single-phase vapor, inverted annular and droplet (no film) flow regimes.

3.6 VISCOUS STRESS AND TURBULENCE MODELS

As noted in Section 2.2.2, the viscous stresses and the turbulence terms are modeled only in the continuous liquid and vapor fields. For the fluid-fluid viscous stress tensor, $\underline{\underline{\sigma}}_\ell$, Ishii (Ref. 2) proposes the relation

$$\underline{\underline{\sigma}}_\ell = 2\,\mu_\ell(\underline{\underline{D}}_{\ell_B} + \underline{\underline{D}}_{\ell_I}) \tag{3.45}$$

where

$$\underline{\underline{D}}_{\ell_B} = \frac{1}{2}\left[\nabla\underline{U}_\ell + (\nabla\underline{U}_\ell)^t\right] \tag{3.46}$$

and

$$\underline{\underline{D}}_{\ell_I} = -\frac{b_\ell(\alpha_\ell)}{2\alpha_\ell}\left[\nabla\alpha_\ell(\underline{U}_v - \underline{U}_\ell) + (\underline{U}_v - \underline{U}_\ell)\,\nabla\alpha_\ell\right] \tag{3.47}$$

The tensors $\underline{\underline{D}}_{\ell_B}$ and $\underline{\underline{D}}_{\ell_I}$ are called the bulk and interfacial deformation tensors, respectively, and $b_\ell(\alpha_\ell)$ is called the mobility of the liquid phase.

The viscous stress model used in the code is a simplified version of the above model. The interfacial deformation and the viscous contributions to the normal stresses are neglected. Thus, the viscous stress model becomes

$$\underline{\underline{\sigma}}_\ell = 2\mu_\ell\underline{\underline{D}}^*_\ell \tag{3.48}$$

where

$$D^*_{\ell_{ij}} = \frac{1}{2}\left(\frac{\partial U_{\ell_j}}{\partial x_i} + \frac{\partial U_{\ell_i}}{\partial x_j}\right)(1 - \delta_{ij}) \tag{3.49}$$

The simplest three-dimensional turbulence model is a generalization of Prandtl's mixing length theory. With this in mind, Ishii (Ref. 2) assumes

$$\underline{\underline{I}}^T_\ell = 2\mu^T_\ell(\underline{\underline{D}}_{\ell_B} + \underline{\underline{D}}_{\ell_I}) \tag{3.50}$$

where μ^T_ℓ is an eddy viscosity for the liquid and can be a function of α_ℓ, ρ_ℓ, $\underline{U}_{v\ell}$, the distance to the nearest wall, and the scalar invariants of $(\underline{\underline{D}}_{\ell_B} + \underline{\underline{D}}_{\ell_I})$. Drew and Lahey (Ref. 18) point out that Equation 3.50 predicts zero turbulent normal stress in a simple shear flow and therefore cannot be correct. They propose a more general model involving four unknown parameters which must be determined by experiment. (Since no experimental results for these parameters have been published, their model is not usable at this time.)

A generalization of the Ishii model has been implemented in the code. The turbulent stress tensor is given by

$$\underline{\underline{I}}^T_\ell = P^T_\ell \underline{\underline{F}}_\ell + 2\mu^T_\ell \underline{\underline{D}}^*_\ell \tag{3.51}$$

The turbulent pressure, defined by

$$P^T_\ell = -\frac{1}{3} T^T_{\ell_{jj}} \tag{3.52}$$

is included to model the normal stresses, while the deformation term models the shear stresses. The tensor $\underline{\underline{F}}_\ell$, defined by

$$\underline{\underline{F}}_\ell = \begin{bmatrix} F_{\ell_{11}} & 0 & 0 \\ 0 & F_{\ell_{22}} & 0 \\ 0 & 0 & F_{\ell_{33}} \end{bmatrix} \tag{3.53}$$

is included to allow for nonisotropic normal stresses. A model for $\underline{\underline{F}}_\ell$ is still needed and is subject to the contraint

$$F_{\ell_{jj}} = 3 \tag{3.54}$$

The following forms are assumed for P_ℓ^T and μ_ℓ^T:

$$P_\ell^T = \rho_\ell \, \ell_m^2 \, (2 \, \underline{\underline{D}}^*_{\ell_B} : \underline{\underline{D}}^*_{\ell_B}) \tag{3.55}$$

$$\mu_\ell^T = \rho_\ell \, \ell_m^2 \sqrt{2 \, \underline{\underline{D}}^*_{\ell_B} : \underline{\underline{D}}^*_{\ell_B}} \tag{3.56}$$

where ℓ_m is the momentum mixing length for the continuous liquid.

The mixing length is input by the user. In rod bundles a value equal to the hydraulic diameter is recommended. Either constant or spatially varying values for ℓ_m and $\underline{\underline{F}}_\ell$ can be used. Although these parameters will generally vary with position in the flow, constant values have given good results in rod bundles, where the scale of the turbulence is well defined by the rod geometry. (The values of ℓ_m and $\underline{\underline{F}}_\ell$ are specified by user input.)

The formulation of the turbulent heat flux consistent with the above turbulent stress treatment is

$$\underline{q}_\ell^T = - \rho_\ell \varepsilon_\ell^T \nabla h_\ell \tag{3.57}$$

where ε_ℓ^T is the turbulent thermal diffusivity and is given by

$$\varepsilon_\ell^T = \ell_h \ell_m \sqrt{2 \underline{\underline{D}}^*_{\ell_B} : \underline{\underline{D}}^*_{\ell_B}} \tag{3.58}$$

In this expression ℓ_h is the energy mixing length for the liquid.

The sum of the conduction and turbulent heat flux becomes

$$\underline{q}_\ell + \underline{q}_\ell^T = - \rho_\ell (\varepsilon_\ell + \varepsilon_\ell^T) \nabla h_\ell \tag{3.59}$$

where $\varepsilon_\ell = k_\ell / \rho_\ell C_{p\ell}$ is the liquid thermal diffusivity. With the introduction of the Prandtl number, $(Pr_\ell = C_{p\ell} \mu_\ell / k_\ell)$ and the turbulent Prandtl number $(Pr_\ell^T = \mu_\ell^T / \rho_\ell \varepsilon_\ell^T)$ the above equation can be written

$$\underline{q}_\ell + \underline{q}_\ell^T = -\left(\frac{\mu_\ell}{Pr_\ell} + \frac{\mu_\ell^T}{Pr_\ell^T}\right) \nabla h_\ell \tag{3.60}$$

The turbulent Prandtl number must be specified by user input and is generally equal to 1.0. The viscous stresses and turbulence terms for the vapor phase are treated in the same manner as for the liquid, but these terms are computed only for the continuous phase. The continous phase is assumed to be liquid for $\alpha < 0.6$, and vapor for $\alpha > 0.8$. A ramp between the two is used for $0.6 < \alpha < 0.8$.

3.7 ENTRAINMENT RATE

Entrainment of liquid drops from the continuous liquid phase can occur under a variety of conditions. The physical models used to determine the average net mass rate of entrainment and the drop formation size will be different for each condition. Entrainment mechanisms that may have a significant influence on reactor thermal hydraulics have been addressed in the development of entrainment models. These include entrainment from liquid films, reflood entrainment, entrainment resulting from vapor bubbling through liquid pools and entrainment resulting from vapor flow across rod structures such as the upper plenum internals of a PWR.

The net mass entrainment rate is defined as

$$S = S''' \cdot (\text{Volume of cell}) \tag{3.61}$$

The net mass entrainment rate, S, has units of mass per unit time and is the net result of the opposing mechanisms of entrainment, S_E, and de-entrainment, S_{DE}. Models for entrainment rate, de-entrainment rate and drop formation size are discussed below.

3.7.1 Entrainment in Film Flow

The entrainment of drops from the liquid film has been studied by numerous investigators (Ref. 7,8,19,20,21). Several different mechanisms for entrainment have been proposed, most of which depend upon the stability of the liquid film. As noted by Hewitt and Hall-Taylor (Ref. 19), the hydrodynamics of film flow as they relate to entrainment are extremely complex and have not been completely quantified. The simplistic approach taken here is an appropriate first attempt at describing a hydrodynamically complex process.

Random perturbations in the flow cause the development of a wavy interface on the film. These waves will grow as a result of the hydrodynamic and surface tension forces acting on the wave. Eventually the amplitude of the wave becomes so large that the pressure differential over the wave exceeds the restraining force of surface tension, and the wave breaks toward the gas core. The resulting drops are then carried along with the vapor. The shape and size of the wave depends on whether the film flow is cocurrent or countercurrent. Lower-amplitude roll waves with drops being sheared off of

the wave crest are typical of cocurrent flow (Ref. 21). Abrupt, large-amplitude waves are typical of countercurrent flow (Ref. 7). This may be partially attributed to the fact that high vapor velocities are required to cause vertical cocurrent upflow. As a result, the film thickness and wave amplitudes are generally smaller than those found in countercurrent vertical flow, which occurs at lower vapor velocities. Also, in countercurrent flow the shear forces act in opposition to gravity, causing larger wave amplitudes.

The model used for the countercurrent case is a simple one. The entrainment rate (S_E) is taken to be the difference between the liquid flow rate in the film and the critical film flow rate:

$$S_E = (\alpha_\ell - \alpha_{\ell_{crit}}) \rho_\ell |u_\ell| A \tag{3.62}$$

The critical liquid fraction is defined as

$$\alpha_{\ell_{crit}} = (1 - \alpha_{v_{crit}}) \tag{3.63}$$

where $\alpha_{v_{crit}}$ is given by Equation 3.6.

It is assumed that all liquid in excess of that required for a stable film is removed from the film and enters into the entrained liquid phase, where it is treated as drops. In reality some of this liquid may be in the form of waves which travel upward while the bulk of the film flows down. The gross flow split between the amount of liquid flowing down and that flowing up in the form of drops and waves is obtained by the above assumption. This is sufficient for most applications. A similar model was used by Lovell (Ref. 7) to predict the penetration rate of liquid against an upflow of vapor.

Whalley, Hewitt and Hutchinson (Ref. 22) have correlated entrainment data for cocurrent film flow with the parameter

$$S_k = k_s \tau_I / \sigma \tag{3.64}$$

where k_s, the equivalent sand roughness, is used as the length scale for the containment force due to surface tension, and τ_I is the interfacial shear stress. Wurtz (Ref. 23) later modified the above correlation by multiplying it by the dimensionless velocity $|\underline{U}_v|\mu_\ell/\sigma$ to compare with a larger variety of data. This velocity was also used by Paleev and Filippovich (Ref. 24) to correlate air-water entrainment data. This resulting correlating parameter

$$S_u = \frac{k_s \tau_I |\underline{U}_v| \mu_\ell}{\sigma^2} \tag{3.65}$$

was then used to obtain a relationship for the entrainment rate. This relationship is

$$S_E = 0.41 \, S_u \, P_w \, \Delta x \tag{3.66}$$

where Δx is the vertical dimension of the mesh cell. This empirical correlation is used to determine the entrainment rate for cocurrent film flow. The equivalent sand roughness is given as

$$k_s = [0.57]\delta + [6625.0 \text{ ft}^{-1}] \, \delta^2 - [3.56 \times 10^6 \text{ ft}^{-2}]\delta^3 + [1.5736 \times 10^9 \text{ ft}^{-3}]\delta^4 \tag{3.67}$$

and

$$\tau_I = \frac{f_I}{2} \rho_v |\underline{U}_{v\ell}|^2 \tag{3.68}$$

Correlations for the interfacial friction factor, f_I, have been given with the interfacial drag model in Section 3.4.

The size of drops formed by entrainment from films has been characterized by Tatterson et al. (Ref. 25). His results are used for both cocurrent and countercurrent flow. The drop formation radius is given by

$$r_s = 0.0056 \left(\frac{D_H \sigma}{\frac{f_s}{2} \rho_v |\underline{u}_v|^2} \right)^{1/2} \tag{3.69}$$

where f_s is defined in Equation 3.34.

3.7.2 De-entrainment in Film Flow

The deposition of drops on the liquid film occurs as a result of random turbulent motions that impart transverse velocity to the drops, bringing them into contact with the solid surfaces or liquid films within the flow channel. The rate at which this occurs has been correlated by Cousins et al. (Ref. 26) using a drop concentration gradient diffusion model in which the concentration at the wall is assumed to be zero. Cousins' model is used to determine the de-entrainment rate for film flow as

$$S_{DE} = k_\sigma \Delta C \, P_w \, \Delta x \tag{3.70}$$

where ΔC is the concentration gradient as given by

$$\Delta C = \frac{\alpha_e \rho_\ell}{\alpha_e + \alpha_v} \tag{3.71}$$

and k_σ is the mass transfer coefficient. The mass transfer coefficient has been found to be a function of surface tension (Ref. 27). This function is reasonably represented by

$$k_\sigma = \max \{3.0491 \times 10^{12}\ \sigma^{5.3054},\ 12.491\ \sigma^{0.8968}\} \qquad (3.72)$$

3.7.3 Entrainment During Reflood

Several mechanisms for the formation of droplets during reflood can be postulated. The droplets may be formed by the breakup of the inverted annular liquid core because of surface instabilities if the liquid is subcooled. If the liquid is saturated, droplets may be formed by bubbles breaking through the surface of the liquid. During top reflood, droplets are formed at the sputtering front as the liquid film is disrupted by the large vaporization rates.

A model similar to one proposed for droplet entrainment by vapor bubbling through liquid pools (Ref. 28) is used for bottom reflood. The entrainment rate is given by

$$S_E = (\alpha_v u_v / u_{crit})^2\ \dot{m}_v \qquad (3.73)$$

where $\dot{m}_v$ is the vertical vapor mass flow rate and u_{crit} is the vertical vapor velocity required to lift a droplet with radius defined by the critical Weber criterion against gravity. The critical velocity is obtained from a balance between the drag force and gravity force acting on the drop,

$$u_{crit} = \left(\frac{4\ We_d}{3C_D}\right)^{1/4} \left(\frac{\sigma g \Delta\rho}{\rho_v^2}\right)^{1/4} \qquad (3.74)$$

A Weber number of 2.7 (typical of reflood in the FLECHT tests) and a drag coefficient of 0.45 are used. The use of the vapor flow rate, $\dot{m}_v$, in Equation 3.73 reflects the effect of boiling at the quench front on droplet formation.

It is assumed that the entrainment rate from a falling film top quench front is equal to the liquid film flow rate, $\dot{m}_\ell$, minus the vapor generation rate at the quench front, Γ_q''', times the volume of the cell:

$$S_E = \dot{m}_\ell - \Gamma_q''' \text{ (volume of cell)} \tag{3.75}$$

The droplet formation size for both top and bottom reflood is assumed to be given by a critical Weber number criterion,

$$r_s = 0.5 \frac{We_d \sigma}{\rho_v (u_{v\ell})^2} \tag{3.76}$$

with a Weber number of 2.7. The maximum droplet size for top reflood is limited to r_s = .003 feet. The low value for the Weber number is a result of using the superficial velocity to compute the droplet size. The vapor velocity where the drops are formed is much higher than the superficial velocity as a result of the reduced void fraction near the quench front.

3.7.4 De-Entrainment on Grid Spacers

It is assumed that any droplets that are in the path of grid spacer structures impinge on the grid spacer and de-entrain.

$$S_{DE} = 0.15\, \alpha_e\, \rho_\ell |u_e| A \tag{3.77}$$

Once a liquid film is established on the grid it is assumed that the same amount of liquid is re-entrained

$$S_E = S_{DE} \tag{3.78}$$

3.7.5 De-Entrainment on Upper Plenum Structure

Liquid carried over during bottom reflood may be de-entrained in the upper plenum as it flows around the upper plenum structures such as support columns and guide tubes. This liquid may then flow down the structures and form a pool above the upper core plate.

The model used in the code is a simple one, employing de-entrainment fractions obtained in the upper plenum de-entrainment experiments of Dallman and Kirchner (Ref. 29).

$$S_{DE} = \eta_{NR}\ \alpha_e\ \rho_\ell |V_e| \text{ (transverse flow area)} \tag{3.79}$$

The de-entrainment fraction, η_{NR}, is input. Following the recommendations of Dallman and Kirchner the de-entrainment fraction for an array of tubes is given by

$$\eta_{NR} = 1 - (1 - \eta_R)^N$$

$$\eta_R = \eta_I\ (1 + 4.5\ \beta^2) \tag{3.80}$$

where η_R = the de-entrainment fraction for a single row of tubes
N = the number of rows of tubes
β = the diameter-to-pitch ratio of the array
η_I = the de-entrainment fraction for a single tube
(0.19 for cylindrical tubes and 0.27 for square tubes.)

3.7.6 De-Entrainment at Area Changes

Droplets will de-entrain at restrictions in the flow path as a result of drop impingement on solid surfaces. This can be expected to occur as droplets formed during reflood flow through the upper tie plate for example. Droplets that strike the solid portions of the tie plate de-entrain and provide the initial liquid for the top quench front. This type of de-entrainment is accounted for using a simple flow area ratio,

$$S_{DE} = (1 - A_1/A_2)\ \alpha_e \rho_\ell |u_e| A_2 \qquad (3.81)$$

where A_1 is the flow area in the restriction and A_2 is the flow area before the restriction.

3.7.7 De-Entrainment on Solid Surfaces and Liquid Pools

All entrained droplets flowing toward a horizontal solid surface, such as the top of the upper plenum, or towards a liquid pool, are assumed to be de-entrained.

3.8 FLUID THERMODYNAMIC PROPERTIES

Saturated and subcooled liquid viscosity, thermal conductivity, specific heat at constant pressure, Prandtl number and surface tension are obtained as functions of enthalpy from data tables. The tables are constructed in enthalpy increments of 10 Btu/lbm from results obtained with the WASP (Ref. 30) computer program.

Saturated and superheated vapor viscosity and thermal conductivity are computed as functions of enthalpy and density by the equations given in the 1967 ASME Steam Tables (Ref. 31). The expression for thermal conductivity is

$$k = k_1 + (103.51 + 0.4198\ T - 2.771(10)^{-5}\ T^2)\rho + 2.1482(10)^{14}\ \frac{\rho^2}{T^{4.2}} \qquad (3.82)$$

where

$$k_1 = 17.6 + 5.87(10)^{-2}\ T + 1.04(10)^{-4}\ T^2 - 4.51(10)^{-8}\ T^3 \qquad (3.83)$$

The viscosity is given by

$$\mu = \begin{cases} \mu_1 - \rho(1858 - 5.9T) & , \text{ if } T < 340^0C \\ \mu_1 + 353\ \rho + 676.5\ \rho^2 + 102.1\ \rho^3 & , \text{ if } T > 365^0C \end{cases} \tag{3.84}$$

$$\mu_1 = 0.407T + 80.4 \tag{3.85}$$

For values of T between 340°C and 365°C the viscosity is interpolated between the values given by the two expressions in Equation 3.84. In Equations 3.82 through 3.85 temperature is in °C, density is in g/cm^3, thermal conductivity is in mW/m-°K and viscosity is in micropoise.

Saturation enthalpies are computed as functions of pressure from equations developed by Agee for EPRI (Ref.32).

$$h_f = \sum_{n=1}^{9} A_{1,n}\ Y^{n-1} \qquad 0.1 < P < 898.7$$

$$h_f = \sum_{n=1}^{9} A_{2,n}\ Y^{n-1} \qquad 898.7 < P < 2529.9 \tag{3.86}$$

$$h_f = \sum_{n=1}^{9} A_{3,n}\ Z^{n-1} \qquad 2529.9 < P < 3208.$$

$$h_g = \sum_{n=1}^{5} B_{1,n}\ Y^{n-1} + \sum_{n=6}^{8} B_{1,n}\ Y^{n+3} \qquad 0.1 < P < 1467.6$$

$$h_g = \sum_{n=1}^{9} B_{2,n}\ Y^{n-1} \qquad 1467.6 < P < 2586.0 \tag{3.87}$$

$$h_g = \sum_{n=1}^{7} B_{3,n}\ Z^{n-1} \qquad 2586 < P < 3208$$

where $Y = \ln(P)$

$Z = (3208.200000001 - P)^{.41}$

The units of P are psia, and h is in Btu/lbm. The coefficients A and B are:

n	$A_{1,n}$	$A_{2,n}$	$A_{3,m}$
1	$.6970887859(10)^{2}$	$.8408618802(10)^{6}$	$.9060030436(10)^{3}$
2	$.3337529994(10)^{2}$	$.3637413208(10)^{6}$	$-.1426813520(10)^{2}$
3	$.2318240735(10)^{1}$	$-.4634506669(10)^{6}$	$.1522233257(10)^{1}$
4	$.1840599513(10)^{0}$	$.1130306339(10)^{6}$	$-.6973992961(10)^{0}$
5	$-.5245502294(10)^{-2}$	$-.4350217298(10)^{3}$	$.1743091663(10)^{0}$
6	$.2878007027(10)^{-2}$	$-.3898988188(10)^{4}$	$-.2319717696(10)^{-1}$
7	$.1753652324(10)^{-2}$	$.6697399434(10)^{3}$	$.1694019149(10)^{-2}$
8	$-.4334859620(10)^{-3}$	$-.4730726377(10)^{2}$	$-.6454771710(10)^{-4}$
9	$.3325699282(10)^{-4}$	$.1265125057(10)^{1}$	$.1003003098(10)^{-5}$

n	$B_{1,n}$	$B_{2,n}$	$B_{3,n}$
1	$.1105836875(10)^{4}$	$.5918671729(10)^{6}$	$.9059978254(10)^{3}$
2	$.1436943768(10)^{2}$	$-.2559433320(10)^{6}$	$.5561957539(10)^{1}$
3	$.8018288621(10)^{0}$	$.3032474387(10)^{5}$	$.3434189609(10)^{1}$
4	$.1617232913(10)^{-1}$	$.4109051958(10)^{1}$	$-.6406390628(10)^{0}$
5	$-.1501147505(10)^{-2}$	$.3475066877(10)^{0}$	$.5918579484(10)^{-1}$
6	$-.1237675562(10)^{-4}$	$-.3026047262(10)^{0}$	$-.2725378570(10)^{-2}$
7	$.3004773304(10)^{-5}$	$-.1022018012(10)^{2}$	$.5006336938(10)^{-4}$
8	$-.2062390734(10)^{-6}$	$.1591215116(10)^{1}$	0.0
9	0.0	$-.6768383759(10)^{-1}$	0.0

The enthalpy of superheated vapor as a function of temperature and pressure is computed from equations given in Keenan and Keys tables (Ref. 33) of 1936:

$$h = f(P,T)$$

$$= F_0 P + \frac{F_1}{2} P^2 + \frac{F_3}{4} P^4 + \frac{F_{12}}{13} P^{13} + F' \qquad (3.88)$$

To define F_0, F_1, F_3 and F_{12}, let

$$\tau = 1/T$$

$$B_0 = 1.89 - 2641.62\ \tau\ 10^{80870\tau^2}$$

$$B_1 = B_0^2\ (82.546\ \tau^2 - 1.6246(10)^5 \tau^3)$$

$$B_3 = B_0^4\ (0.21828\ \tau^3 - 1.2697(10)^5 \tau^5)$$

$$B_{12} = -B_0^{13}\ (3.635(10)^{-4} \tau^{12} - 6.768(10)^{64} \tau^{36}) \qquad (3.89)$$

Then the F_K are defined by

$$F_k = \frac{\partial}{\partial \tau} (B_k \tau) \quad , \quad k = 0,1,3,12 \qquad (3.90)$$

The function F' is given by

$$F' = \int_{273.16}^{T} C_{p_o}\ dT + 2502.36 \qquad (3.91)$$

with

$$C_{p_o} = 1.4720 + 7.5566(10)^{-4}T + 47.8365\ \tau \qquad (3.92)$$

In Equations 3.88 through 3.92, T is in °K, P is in atmospheres and h is in J/g.

Values for superheated vapor temperature are computed as functions of pressure and enthalpy using an iterative method described by McClintock and Silvestri (Ref. 34). First, estimates for T and C_p are computed from the expressions

$$T = A_1 + A_2h + A_3h^2 + A_4h^3 + A_5P + A_6P^2$$

$$+ A_7P^3 + P(A_8h + A_9h^2 + A_{10}h^3) \qquad (3.93)$$

$$1/C_p = B_1 + B_2h + B_3h^2 + B_4h^3 + B_5 \ln P + B_6(\ln P)^2$$

$$+ B_7(\ln P)^3 + (\ln P)\ (B_8h + B_9h^2 + B_{10}h^3) \qquad (3.94)$$

where T is in °F, P is in psia, h is in Btu/lbm and C_p is in Btu/lbm-°F. When $P \leq 1000$ psia, or $P > 100$ psia and $h \geq 1280$ Btu/lbm, the constants are

$A_1 = -1.0659659(10)^4$
$A_2 = 2.0110905(10)^1$
$A_3 = -1.250954(10)^{-2}$
$A_4 = 2.8274992(10)^{-6}$
$A_5 = 4.9815820$

$A_6 = -7.7618225(10)^{-6}$
$A_7 = 2.4391612(10)^{-10}$
$A_8 = -9.8147341(10)^{-3}$
$A_9 = 6.5824890(10)^{-6}$
$A_{10} = -1.4747938(10)^{-9}$
$B_1 = -2.8557816$
$B_2 = 1.3250230(10)^{-2}$
$B_3 = -1.0521514(10)^{-5}$
$B_4 = 2.5007955(10)^{-9}$
$B_5 = -3.4620214$
$B_6 = -3.6261637(10)^{-2}$
$B_7 = 7.3529479(10)^{-4}$
$B_8 = 5.7703098(10)^{-3}$
$B_9 = -2.9972073(10)^{-6}$
$B_{10} = 5.2037300(10)^{-10}$

Where $P > 1000$ psia and $h < 1280$ Btu/lbm, the constants are given by

$A_1 = -4.5298646(10)^{3}$
$A_2 = 1.5358850(10)^{1}$
$A_3 = -1.5655537(10)^{-2}$
$A_4 = 5.2687849(10)^{-6}$
$A_5 = 4.4185386(10)^{-1}$
$A_6 = -9.1654905(10)^{-6}$
$A_7 = 2.7549766(10)^{-10}$
$A_8 = -1.1541553(10)^{-3}$
$A_9 = 1.2384560(10)^{-6}$
$A_{10} = -4.1724604(10)^{-10}$
$B_1 = 1.2659960(10)^{2}$
$B_2 = -2.5611614(10)^{-1}$
$B_3 = 2.2270593(10)^{-4}$
$B_4 = -5.9928922(10)^{-8}$
$B_5 = -2.1818030(10)^{1}$
$B_6 = 1.3424036$

$$B_7 = -4.9110372(10)^{-2}$$
$$B_8 = 2.7966370(10)^{-2}$$
$$B_9 = -2.4665012(10)^{-5}$$
$$B_{10} = 6.7723080(10)^{-9}$$

The estimated temperature is then used to compute an approximate enthalpy from

$$h' = f(P,T) \tag{3.95}$$

where the function f(P,T) has been described by Equations 3.88 through 3.92. Next, a temperature correction, ΔT, is computed from

$$\Delta T = (1/C_p)\ (h - h') \tag{3.96}$$

and the new estimated temperature becomes

$$T' = T + \Delta T \tag{3.97}$$

A new approximate enthalpy, h", is computed using this temperature in Equation 3.95, and the iteration is continued until $(T - T') < 1.0°F$. Iteration is not used in the specific heat calculation. The C_p value given by Equation 3.94 is taken as the final value.

Liquid and vapor specific volumes as functions of pressure and enthalpy are computed using equations from Reference 33. For the vapor,

$$v = E_1 + E_2P + E_3/P + E_4h + E_5Ph + E_6h/P \tag{3.98}$$

and for the liquid

$$v = \exp\left\{\sum_{k=0}^{4}\sum_{n=0}^{2} C_{k,n} P^n h^k\right\} \tag{3.99}$$

where P is in psia, h is in Btu/lbm and v is in ft^3/lbm. The constants for these equations are

$$E_1 = -0.81735849(10)^{-3}$$
$$E_2 = 0.12378514(10)^{-4}$$
$$E_3 = -0.10339904(10)^{4}$$
$$E_4 = -0.62941689(10)^{-5}$$
$$E_5 = -0.87292160(10)^{-8}$$
$$E_6 = 0.12460225(10)^{1}$$

$C_{0,0} = -0.41345(10)^{1}$	$C_{0,1} = -0.59428(10)^{-5}$	$C_{0,2} = 0.15681(10)^{-8}$
$C_{1,0} = 0.13252(10)^{-4}$	$C_{1,1} = 0.63377(10)^{-7}$	$C_{1,2} = -0.40711(10)^{-10}$
$C_{2,0} = 0.15812(10)^{-5}$	$C_{2,1} = -0.39974(10)^{-9}$	$C_{2,2} = 0.25401(10)^{-12}$
$C_{3,0} = -0.21959(10)^{-8}$	$C_{3,1} = 0.69391(10)^{-12}$	$C_{3,2} = -0.52372(10)^{-15}$
$C_{4,0} = 0.21683(10)^{-11}$	$C_{4,1} = -0.36159(10)^{-15}$	$C_{4,2} = 0.32503(10)^{-18}$

4.0 HEAT TRANSFER MODELS

The heat transfer models in the vessel module of COBRA/TRAC determine the material heat release rates and temperature response of the fuel rods and structural components of a light water reactor during operating and transient conditions. All of the heat transfer calculations are performed at the beginning of each time step before the hydrodynamic solution. Heat transfer coefficients based on old time fluid conditions are used to advance the material conduction solution. The resultant heat release rates are explicitly coupled to the hydrodynamic solution as source terms in the fluid energy equations.

To effectively perform these tasks, a consistent set of heat transfer models was developed. It consists of four components:

- CONDUCTION MODEL — specifies the conductor geometry and material properties, and solves the conduction equation
- HEAT TRANSFER PACKAGE — selects and evaluates the appropriate heat transfer correlations
- QUENCH FRONT MODEL — a "fine mesh-rezoning" method that calculates quench front propagation due to axial conduction and radial heat transfer
- GAP CONDUCTANCE MODEL — a dynamic gap conductance model[a] that evaluates fuel pellet-clad conductance for a nuclear fuel rod.

(a) Developed for the VIPRE code (Ref. 35) under EPRI Contract 2311203885 based on models in the FRAP (Ref. 36) and GAPCON (Ref. 37) codes.

4.1 CONDUCTION MODELS

The rod model is designed for nuclear fuel rods, heater rods, tubes and walls. These options allow the user to simulate most of the conductor geometries found in reactor vessels and heat transfer experiments. In addition, an unheated conductor model is provided for structural heat transfer surfaces.

4.1.1 Conductor Geometry

A nuclear fuel rod model requiring minimal user input is built into the code. Material properties can be specified by input or defaulted to uranium-dioxide and zircaloy. These properties are calculated using correlations from MATPRO-11 (Revision 1) (Ref. 38). The conductor geometry for a nuclear fuel rod is illustrated in Figure 4.1. Only cylindrical fuel rods with fluid thermal connections on the rod exterior are considered by this model.

A dynamic gap conductance model based on the GAPCON (Ref. 37,39) and FRAP (Ref. 36,40,41) computer codes is available for use with the nuclear fuel rod model. This is discussed in Section 4.4. Alternatively, the user may specify gap conductance by input, either as a constant or with axial and temporal variations using input forcing functions. (The gap conductance options are available only with the nuclear fuel rod model.)

Electric heater rods used as fuel pin simulators and other solid cylinders can be modeled with the heater rod option. These rods consist of concentric rings of different material regions, as shown in Figure 4.2. In each region the material type, number of radial nodes, width and power factor are specified by input. Contact resistances are not calculated between material regions but can be modeled by including a region one node wide with material properties that give it the appropriate thermal resistance.

Conductors, either tube or plate, with thermal connections to channels on either the inner or the outer surface are modeled by the tube and wall models. These geometries, shown in Figure 4.3, are similar to the heater rod model except for the interior coolant connections. Concentric and flat plate fuel elements, thermal walls and simple tubes can be modeled with these options. Each rod may extend through any number of channel-splitting sections, but each

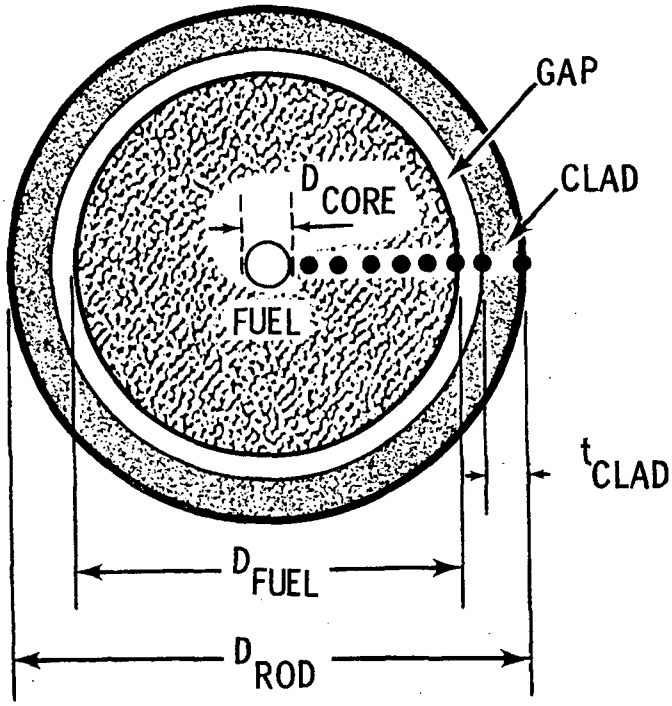

FIGURE 4.1. Nuclear Fuel Rod Geometry

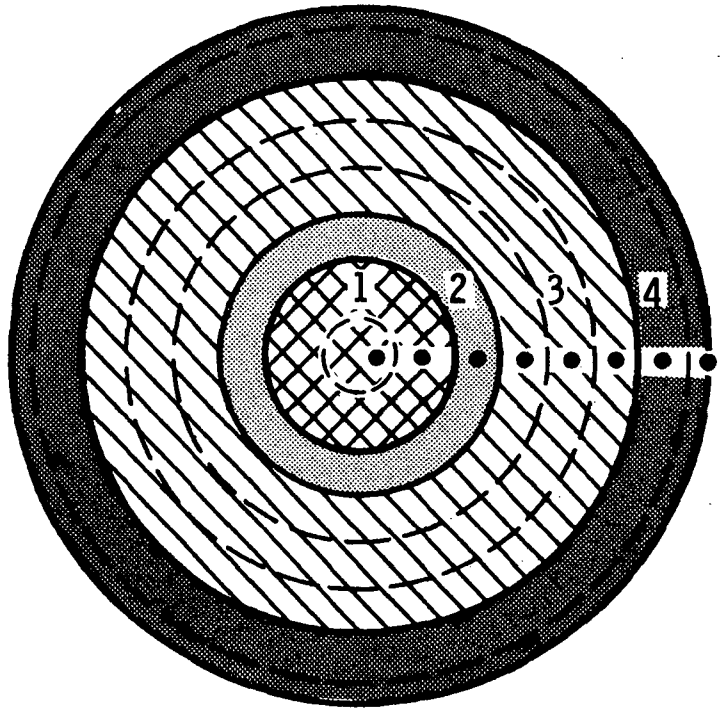

FIGURE 4.2. Heater Rod Geometry (Example of a Fuel Pin Simulator)

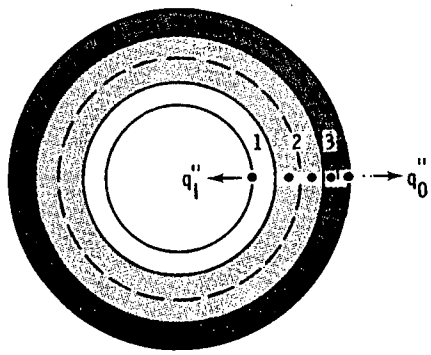

A) TUBE

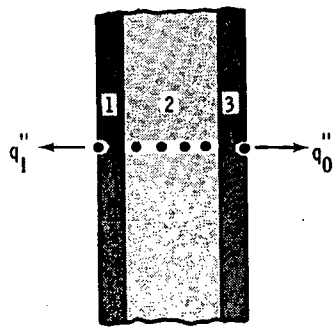

B) WALL

FIGURE 4.3. Tube and Wall Conductor Geometries

heat transfer surface may only be connected to one channel in each section. Detailed discussion of how to use these models for specific problems and the definition of a section are included in the User's Manual, Volume 3.

4.1.2 Unheated Conductor Model

Structural heat transfer surfaces can be more efficiently modeled with the unheated conductor model. This option accesses the same conductor geometries (except for the nuclear fuel rod geometry) as the rod model, and uses the same heat transfer package. However, to economize computer time and storage, the unheated conductor model is limited in the following ways:

- No internal heat generation is included.
- Radial conduction only is used.
- No fine mesh-rezoning quench front model is included.
- Unheated conductors do not extend across section boundaries.
- The fluid solution cannot be forced into the "hot wall" flow regime.

- Vapor properties in the convective heat transfer correlations are evaluated at the bulk vapor temperature rather than the film temperature.
- The minimum film boiling temperature is set to a constant 900°F.

These limitations only apply to the unheated conductor model and not to the rod model in general. Unheated conductors should be used to model structural elements for which expected peak temperatures are well below the minimum film boiling point.

4.1.3 Conduction Equation

The modeling requirements of the vessel module include the ability to simulate generalized conductor geometries (fuel rods, electric heater rods, tubes, and walls) and temperature-dependent material properties. To accomplish this, a finite-difference form of the conduction equation has been employed (replacing the orthogonal collocation method of COBRA-IV-I, (Ref. 42).

The difference equations are formulated using the "heat balance" approach (Ref. 43) which easily accommodates the following features:

- unequal mesh spacing
- temperature-dependent material properties
- space-dependent material properties
- internal resistances (such as those due to gaps)
- radial heat generation profiles.

The finite-difference nodes of the conduction equation are modeled as control volumes connected by thermal resistances. They form a set of linearized equations solved by Gaussian elimination and back-substitution.

The radial conduction equation for a control volume can be derived from a simple heat balance. For node i of Figure 4.4 this is

$$(\rho C_p V)_i \frac{\partial T_i}{\partial t} = - Q_{i,i-1} - Q_{i,i+1} + Q'''_i V_i \qquad (4.1)$$

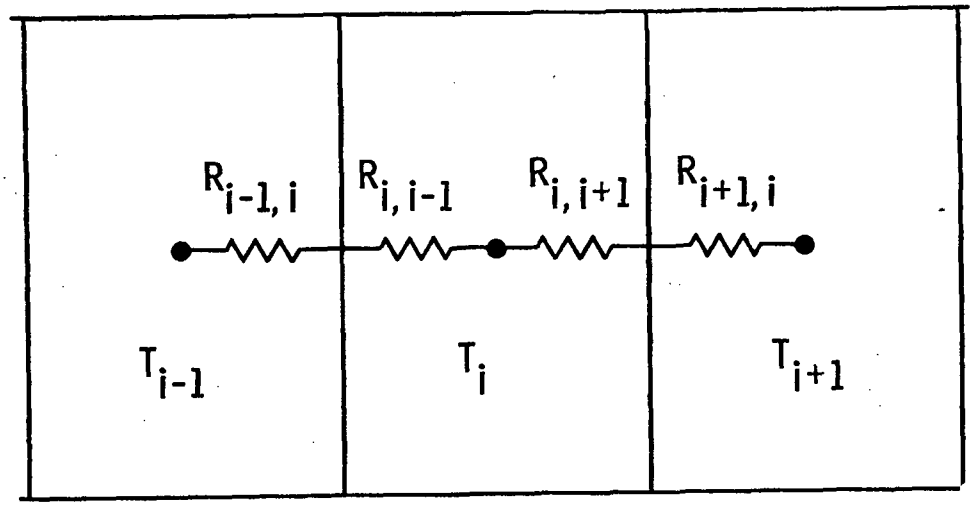

FIGURE 4.4. Heat Balance Control Volume

where ρ = density (lbm/ft^3)

C_p = specific heat (Btu/lbm-°F)

V = node volume (ft^3)

T = node temperature (°F)

$Q_{i,i-1}$ = radial heat flow from node (i) to (i-1) (Btu/sec)

$Q_{i,i+1}$ = radial heat flow from node (i) to (i+1) (Btu/sec)

Q_i''' = volumetric heat generation rate ($Btu/sec-ft^3$)

The locations of radial conduction nodes are automatically calculated for a conductor geometry type. Each material region is divided into a specified number of subregions of equal radial thickness, and a conduction node is located at the center of mass of each subregion. This rule is followed for all nodes except the following:

- the node at the inside and outside surface of a "TUBE" or "WALL"
- outside surface of a heater rod
- fuel pellet exterior, cladding interior and cladding exterior surface for a nuclear fuel rod.

For these surfaces, a subregion half as wide as the other subregions is defined, and the node is located on the surface. The noding within a nuclear fuel rod is illustrated in Figure 4.5. (The fuel centerline temperature is calculated by Hermite interpolation.)

The radial positions of the conduction nodes are fixed; relocation due to thermal expansion is not calculated. To prevent an apparent loss of mass from the conductor because of density change with temperature, the term (ρV) is evaluated at the cold state density and dimensions, and defines the mass M_i associated with node i. So Equation 4.1 becomes

$$(MC_p)_i \frac{\partial T_i}{\partial t} = - Q_{i,i-1} - Q_{i,i+1} + Q'''_i V_i \qquad (4.2)$$

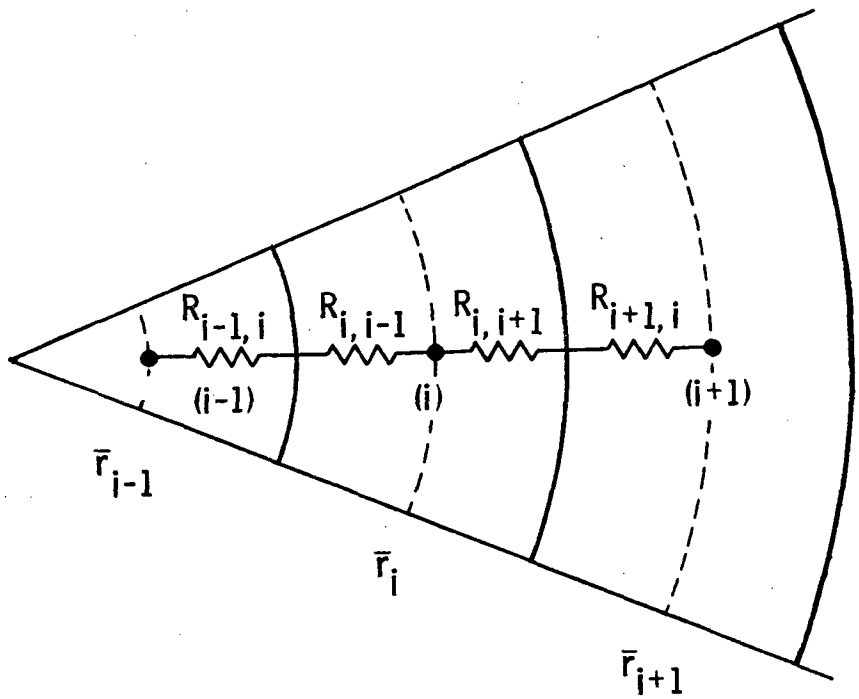

FIGURE 4.5. Conduction Node Positioning

Heat transfer through a node is computed from the conductance, K, of the material and the temperature gradient across the node as

$$Q_{i,j} = - K_{i,j} (T_j - T_i) \tag{4.3}$$

and

$$K_{i,j} = K_{j,i} \quad \text{for } j = \begin{cases} i-1 \\ i+1 \end{cases}$$

The conductance is simply the inverse of the thermal resistance, R, between nodes and is computed as

$$K_{i,i-1} = 1/(R_{i,i-1} + R_{i-1,i}) \tag{4.4}$$

Thermal resistances are calculated for each node as a function of geometry and thermal conductivity. (See Appendix C for a complete explanation of this procedure.)

Substituting Equation 4.3 into 4.2 gives

$$(MC_p)_i \frac{\partial T_i}{\partial t} = K_{i,i-1} (T_{i-1} - T_i) + K_{i,i+1} (T_{i+1} - T_i) + Q'''_i V_i \tag{4.5}$$

Forward differencing the temporal derivative in Equation 4.5 yields

$$\frac{(MC_p)_i}{\Delta t} (T_i - T_i^n) = K_{i,i-1} (T_{i-1} - T_i) + K_{i,i+1} (T_{i+1} - T_i) + Q'''_i V_i \tag{4.6}$$

where; Δt = time increment

n = old time level (all other temperatures are at the new time level)

To solve this equation, an implicit formulation is applied in the radial direction and the equation solved by Gaussian elimination for all nodes at that axial level. Axial conduction, if used, is treated as an explicit source term. The finite-difference equation for node (i) is then:

$$\frac{(MC_p)_i}{\Delta t}(T_i - T_i^n) = K_{i,i-1}(T_{i-1} - T_i) + K_{i,i+1}(T_{i+1} - T_i)$$

$$+ K_{i,j-1}(T_{j-1}^n - T_i^n) + K_{i,j+1}(T_{j+1}^n - T_i^n)$$

$$+ Q_i''' V_i \qquad (4.7)$$

where the subscripts (j+1) and (j-1) represent the nodes at the same radial location and immediately above and below node i. If the stability criterion for the explicit axial conduction is exceeded, the time step used in the conduction equation is divided into two or more smaller time steps and the conduction equation is solved for each of these.

Variations of Equation 4.7 are defined for the boundary nodes. The boundary condition applied to the conduction equation can be adiabatic or a surface heat transfer coefficient. Adiabatic boundary conditions are assigned to the center nodes of solid cylindrical rods (nuclear and heater rods) and at any surface node not connected to the fluid. Heat transfer coefficient boundary conditions are applied at surfaces connected to the fluid.

The heat transfer surface is coupled to the fluid channel through the heat transfer coefficient boundary condition. For each surface heat transfer node, both a heat transfer coefficient and a fluid sink temperature are specified for each phase of the fluid. Thus, the rod heat flux is given by:

$$q'' = H_\ell \, (T_s - T_\ell^n) + H_v \, (T_s - T_v^n) \tag{4.8}$$

The fraction of the rod surface area in contact with a given phase is accounted for in the heat transfer coefficient (e.g., $H_v = 0$ for annular flow).

The nucleate boiling heat flux depends very strongly on the wall surface temperature. Since the wall temperature is in turn affected strongly by the heat flux, the surface temperature solution may oscillate in nucleate boiling unless the heat transfer and wall temperature solution are coupled implicitly. This is done non-iteratively by including the "linearized" derivative of the heat transfer coefficient with respect to temperature in the surface boundary condition. Therefore, the heat flux from the surface to phase (ℓ) is given by:

$$q''_\ell = H_\ell (T_s - T_\ell^n) + \left(\frac{\partial H_\ell}{\partial T_s}\right) (T_s - T_s^n) \, (T_s^n - T_\ell^n) \tag{4.9}$$

Rewriting Equation (4.7) for a surface node (s):

$$\begin{aligned} \frac{(MC_p)_s}{\Delta t} (T_s - T_s^n) = {} & K_{s,s-1} \, (T_{s-1} - T_s) + K_{s,j-1} \, (T_{j-1}^n - T_s^n) \\ & + K_{s,j+1} \, (T_{j+1}^n - T_s^n) \\ & - A_s \left[H_\ell (T_s - T_\ell^n) + \frac{\partial H_\ell}{\partial T_s} (T_s - T_s^n)(T_s^n - T_\ell^n) \right] \\ & - A_s \, H_v \, (T_s - T_v^n) + Q'''_s \, V_s \end{aligned} \tag{4.10}$$

where A_s is the heated surface area.

Equation 4.10 is solved simultaneously with a set of equations for the interior nodes to determine the new time temperatures. The amount of heat transferred to each phase of the fluid during the time step is back calculated after the conduction equation is solved, as follows:

$$Q_\ell = \left[H_\ell (T_s - T_\ell^n) + \frac{\partial H_\ell}{\partial T_s} (T_s - T_s^n)(T_s^n - T_\ell^n)\right] A_s$$

$$Q_v = H_v (T_s - T_v^n) A_s \qquad (4.11)$$

4.2 HEAT TRANSFER PACKAGE

The heat transfer package consists of a library of heat transfer correlations and a selection logic algorithm. Together these produce a continuous boiling curve that is used to determine the phasic heat fluxes. A schematic of the boiling curve shown in Figure 4.6 and Figure 4.7 illustrates the heat transfer regime selection logic. The correlations used in each regime are detailed below.

4.2.1 Single-Phase Vapor

The maximum of the Dittus-Boelter (Ref. 15) turbulent convection correlation and the McAdams (Ref. 44) steam natural convection equation is used. For single-phase convection to vapor, all vapor properties except β are evaluated at the film temperature.

- Dittus-Boelter (steam)

$$HTC = 0.023 \frac{k_v}{D_H} \left(\frac{G_v D_H}{\mu_v}\right)^{0.8} (Pr_v)^{0.4} \qquad (4.12)$$

- McAdams Natural Convection

$$HTC = 0.13\ k_v \left[\frac{\rho_v^2\ g\ \beta\ (T_w - T_v)}{\mu_v^2} \right]^{1/3} \qquad (4.13)$$

4.2.2 Single-Phase Liquid

Convection to single-phase liquid is computed as the larger of either the Dittus-Boelter turbulent convection correlation or the laminar flow with a limit Nusselt number equal to 7.86 (Ref. 45).

- Dittus-Boelter (liquid)

$$HTC = 0.23 \frac{k_\ell}{D_H} \left(\frac{G_\ell\ D_H}{\mu_\ell} \right)^{0.8} (Pr_\ell)^{0.4} \qquad (4.14)$$

- Laminar

$$HTC = 7.86 \frac{k_\ell}{D_H} \qquad (4.15)$$

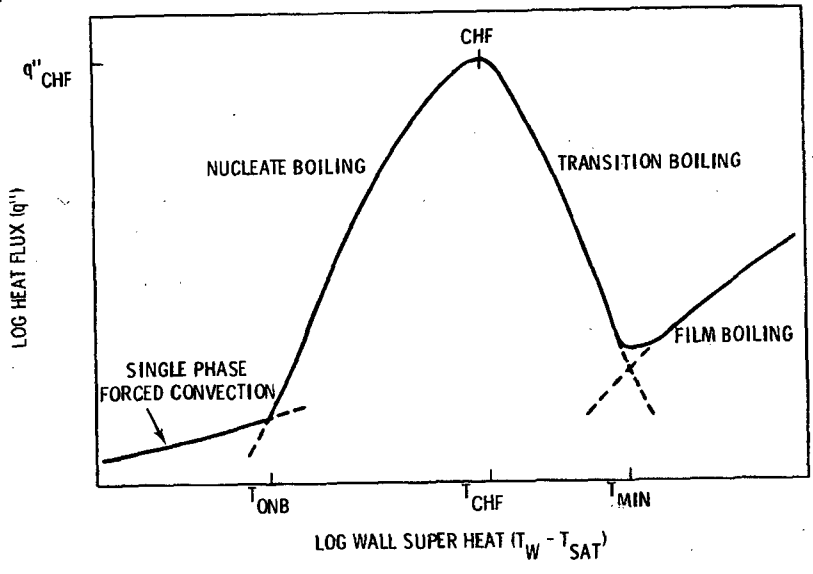

FIGURE 4.6. Schematic Representation of the Boiling Curve

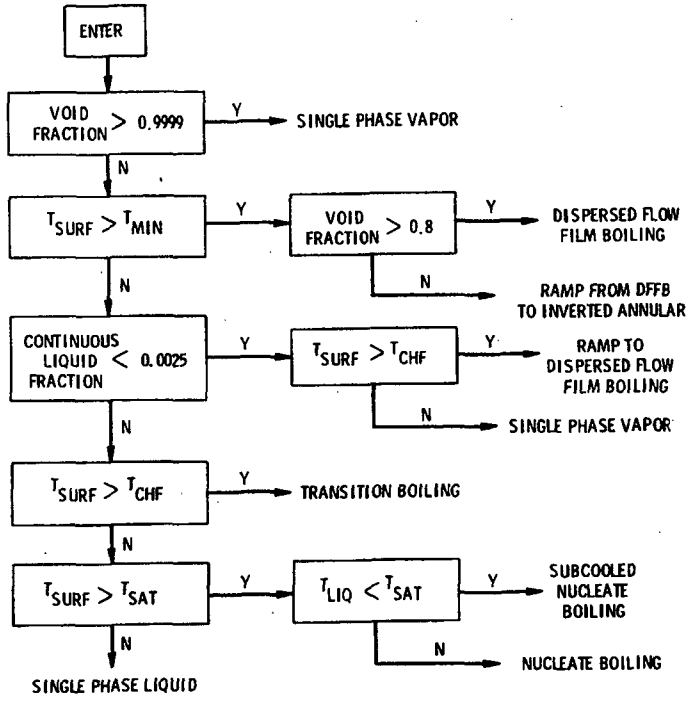

FIGURE 4.7. Heat Transfer Regime Selection Logic

4.2.3 Nucleate Boiling

When the wall temperature is greater than saturation but less than the critical heat flux temperature and liquid is present, the Chen (Ref. 46) nucleate boiling correlation is used. The Chen correlation applies to both the saturated nucleate boiling region and the two-phase forced convection region. It automatically makes the transition to single-phase convection at low wall superheat and pool boiling at low flow rate. Chen assumes a superposition of a forced-convection correlation (Dittus-Boelter type) and a pool boiling equation (Forster-Zuber). Thus

$$H_{CHEN} = H_{SPL} + H_{NB}$$

where $H_{SPL} = 0.023\ F\ (\frac{k_f}{D_H})\ Re^{0.8}\ Pr^{0.4}$ (4.16)

F = Reynolds number factor (Figure 4.8)

Re = Reynolds number = $\frac{(1-x)\ G\ D_H}{\mu_f}$

Pr = Prandtl number

and

$$H_{NB} = 0.00122\ S\ \left[\frac{k_f^{0.79} Cp_f^{0.45} \rho_f^{0.49} g_c^{.25}}{\sigma^{0.5} \mu_f^{0.29} h_{fg}^{0.24} \rho_g^{0.24}}\right] (T_w - T_f)^{0.24} (P_w - P)^{0.75} \quad (4.17)$$

where S = suppression factor (Figure 4.9)

T_w = wall surface temperature

P_w = saturation pressure corresponding to T_w (lbf/ft^3)

All fluid properties are evaluated at saturation conditions. Butterworth developed curve fits for both the Reynolds number factor (F) and the suppression factor[a] (S) as follows (Ref. 47):

$$F = \begin{cases} 1.0 & ; \ X_{tt}^{-1} \leq 0.1 \\ 2.34\ (X_{tt}^{-1} + 0.213)^{0.736} & ; \ X_{tt}^{-1} > 0.1 \end{cases} \quad (4.18)$$

where X_{tt}^{-1} = inverse Martinelli factor

$$X_{tt}^{-1} = \left(\frac{x}{1-x}\right)^{0.9} \left(\frac{\rho_f}{\rho_g}\right)^{0.5} \left(\frac{\mu_g}{\mu_f}\right)^{0.1} \quad (4.19)$$

$$S = \begin{cases} [1 + 0.12(Re'_{TP})^{1.14}]^{-1} & ; \ Re'_{TP} < 32.5 \\ [1 + 0.42(Re'_{TP})^{0.78}]^{-1} & ; \ 32.5 \leq Re'_{TP} < 50.9 \\ 0.1 & ; \ Re'_{TP} \geq 50.9 \end{cases} \quad (4.20)$$

(a) Reynolds number limit modified from original 70 to be continuous

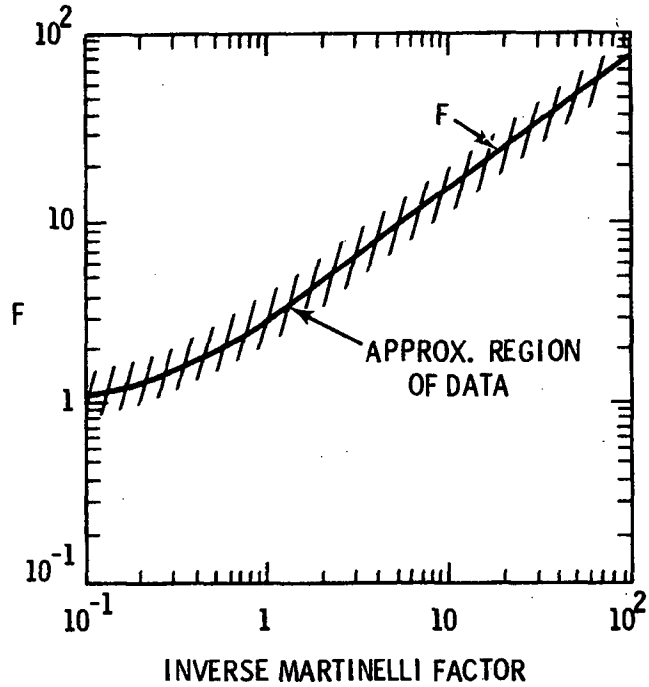

FIGURE 4.8. Reynolds Number Factor, F, for Chen Correlation

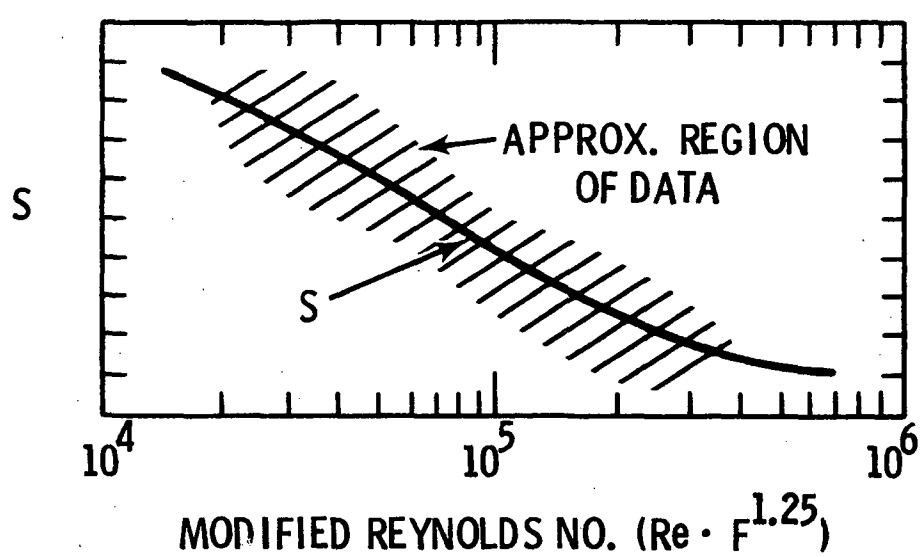

FIGURE 4.9. Suppression Factor, S, for Chen Correlation

where $Re'_{TP} = (1 \times 10^{-4})\ Re\ F^{1.25}$ (4.21)

These factors are illustrated graphically in Figures 4.8 and 4.9.

4.2.4 Subcooled Nucleate Boiling

The Chen correlation, though developed for saturated boiling, may be extended into the subcooled region. As discussed in the saturated boiling section, the Chen correlation superimposes a forced convective and nucleate boiling component. For subcooled boiling

$$q'' = q''_{FC} + q''_{NB}$$

The nucleate boiling heat flux is evaluated as

$$q''_{NB} = H_{NB}(T_w - T_f) \quad (4.22)$$

where H_{NB} is defined by Equation 4.17 above, and the suppression factor, S, is computed from Equation 4.20 using the single-phase Reynolds number $Re = G_\ell D_H/\mu_\ell$. The forced convection heat flux is computed from Equation 4.16 using subcooled liquid properties and setting the flow factor, F, to unity, so

$$q''_{FC} = 0.023 \left(\frac{k_\ell}{D_H}\right) Re^{0.8}\ Pr^{0.4}\ (T_w - T_\ell) \quad (4.23)$$

where $Re = \dfrac{G_\ell D_H}{\mu_\ell}$

T_ℓ = local bulk fluid temperature

Moles and Shaw (Ref. 48) compared the Chen correlation to subcooled boiling data for several fluids and reported satisfactory agreement for water at low to moderate subcoolings.

During subcooled boiling, vapor generation occurs and a significant void fraction ($\alpha \sim 0.6$) may exist despite the presence of subcooled water. In this regime, four processes are of interest:

i) forced convection to liquid
ii) vapor generation at the wall
iii) condensation near the wall
iv) bulk condensation (subcooled liquid core).

Condensation occurring because of the presence of vapor in the subcooled liquid core is calculated implicitly during the solution of the energy equations and does not affect the determination of phasic heat inputs. Forced convection to liquid is treated using Equation 4.23 and the heat input to the liquid energy equation. The nucleate boiling component of the Chen correlation (Equation 4.22) defines the amount of heat available to cause vapor generation at the wall.

The near-wall condensation is estimated using the Hancox-Nicoll (Ref. 49) correlation for heat flux at the point where all the bubbles generated collapse in the near-wall region:

$$q''_{HN} = 0.4 \left[\frac{C_{p_f} \mu_f}{D_H}\right] \left[\frac{G D_H}{\mu_f}\right]^{0.662} (T_f - T_\ell) \qquad (4.24)$$

where T_f = saturation temperature
T_ℓ = subcooled liquid temperature

The heat flux dissipated in near-wall condensation is calculated as

$$q''_C = \text{MAXIMUM}\ (0.0;\ q''_{HN} - q''_{SPL})$$

Subtracting the near wall condensation from the amount available for vapor generation yields:

$$Q_\Gamma = (q''_{NB} - q''_c)\ A_H \tag{4.25}$$

However, a fraction of Q_Γ is expended to heat up the subcooled liquid "pumped" into the saturated thermal boundary layer. This fraction is given by the Rouhani (Ref. 50) model:

$$\varepsilon_p = \frac{(\rho_f/\rho_g)\ (h_f - h_\ell)}{h_{fg} + (\rho_f/\rho_g)\ (h_f - h_\ell)} \tag{4.26}$$

and;

$$\varepsilon_\Gamma = (1 - \varepsilon_p) = \frac{h_{fg}}{h_{fg} + (\rho_f/\rho_g)(h_f - h_\ell)} \tag{4.27}$$

where ε_p = fraction of heat to boundary layer
ε_Γ = fraction of heat causing vapor generation

Finally, the amount of vapor generation is:

$$Q_\Gamma = (q''_{NB} - q''_c)\ \varepsilon_\Gamma\ A_H \tag{4.28}$$

and, adding all the heat inputs to the liquid:

$$Q_L = [q''_{SPL} + (1-\varepsilon_\Gamma)\ q''_{NB} + \varepsilon_\Gamma\ q''_c]\ A_H \tag{4.29}$$

The heat source term for vapor generation, Q_Γ, enters the liquid energy equation as an explicit vapor generation rate [$\Gamma = Q_\Gamma/(h_g - h_f)$] and will

partially condense because of the implicit bulk condensation. This model was developed for the two-fluid steam generator code, COBRA-TF/EPRI, (Ref. 51) and has been quite successful in predicting subcooled void distributions (Ref. 52).

4.2.5 Critical Heat Flux and Transition Boiling Regime

The intersection of the nucleate boiling and transition boiling heat transfer regimes occurs at the CHF point. To provide for a continuous transition between regimes, the CHF point (q''_{CHF}, T_{CHF}) must be specified.

Three CHF regimes are considered (see Figure 4.10); pool boiling, forced-convection departure from nucleate boiling (DNB) and annular film dryout.

Pool Boiling DNB

Pool boiling DNB is selected when the mass flux is low ($G < 30$ g/cm^{2}sec) and the flow regime is not annular film flow. The pool boiling critical heat flux is given by Griffith's (Ref. 74) modification of the Zuber (Ref. 53) equation:

$$q''_{CHF} = 0.9\ (1-\alpha)\ \frac{\pi}{24}\ h_{fg}\ \rho_g^{0.5}\ [g_c g\sigma(\rho_f-\rho_g)]^{0.25} \qquad (4.30)$$

The critical heat flux in this region is chosen as the larger of Equation 4.30 and the forced convection DNB heat flux evaluated at a mass flux of 30 g/cm^2-sec.

Forced-Convection DNB

Forced-convection DNB is considered when the mass flux is greater than 30 g/cm$_2$sec and the flow regime is not annular film flow. The critical heat flux is given by the Biasi correlation (Ref. 54) which consists of two equations, one for low-quality CHF and one for high-quality CHF, and is given below:

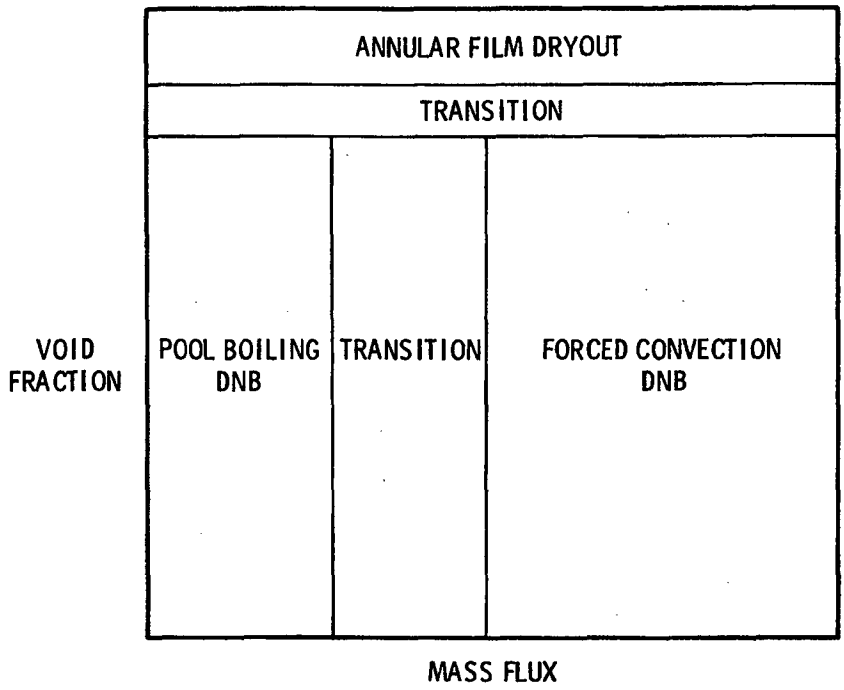

FIGURE 4.10. Schematic of CHF Regime Selection Logic

$$q''_{B1} = (5.9695 \times 10^6)\, G^{-1/6}\, (F(P)G^{-1/6} - X)\, D_H^{-n} \qquad (4.31)$$

$$q''_{B2} = (11.98 \times 10^6)\, H(P)\, (1-X)\, D_H^{-n}\, G^{-0.6} \qquad (4.32)$$

where q" = critical heat flux (Btu/hr-ft^2)
G = mass flux (g/cm^2-sec)
P = pressure (bars)
D_H = hydraulic diameter (cm)
X = quality
n = 0.6, if $D_H < 1.0$ cm: n = 0.4, if $D_H \geq 1.0$ cm

and

$$F(P) = 0.7249 + 0.099\ P \exp(-0.032\ P) \tag{4.33}$$

$$H(P) = -1.159 + 0.149\ P \exp(-0.019\ P) + 8.99\ P\ (10+P^2)^{-1} \tag{4.34}$$

The critical heat flux is defined as the maximum of the two equations.

$$q''_{CHF} = \text{Maximum}\ (q''_{B1},\ q''_{B2}) \tag{4.35}$$

Annular Film Dryout

If annular flow exists, the departure from nucleate boiling is caused by annular film dryout. In this regime, the heat flux is not limited by a correlation, but rather forced convection vaporization exists until the film dries out. Film dryout is a complex function of the film flow rate, the applied heat flux, and the entrainment/de-entrainment rate, and is determined by the solution of the hydrodynamic equations. This approach was pioneered by Whalley et al. (Ref. 55,56) and has been applied successfully to the analysis of the Bennett tube tests (Ref. 57) (see Volume 4, Developmental Assessment and Applications).

To be consistent with the remainder of the heat transfer package, the critical heat flux point for annular film dryout must be defined. A value of 75 °F wall superheat has been selected and the critical heat flux is set to that given by the Zuber equation. The onset of film boiling is not affected by this definition since film boiling is controlled by film dryout (see Figure 4.7). As before, the critical heat flux is ramped between the annular film dryout regime and the pool boiling and forced-convection DNB regimes.

Critical Heat Flux Temperature

To define the boiling curve, it is necessary to know the surface temperature at which CHF occurs. An iterative procedure is used to find the wall temperature at which the heat flux from the Chen nucleate boiling correlation is equal to the critical heat flux. Thus,

$$q''_{CHEN}\ (T_{CHF}) = q''_{CHF}$$

Minimum Stable Film Boiling Point

The transition boiling regime is bounded by the CHF point (below which the wall is continuously wetted and nucleate boiling exists) and the minimum stable film boiling point (above which the liquid cannot wet the wall and film boiling exists). It is assumed that the minimum film boiling temperature is the wall temperature that results in an instantaneous contact temperature equal to the homogeneous nucleation temperature, T_{HN}. Using a contact temperature correction to include the effects of surface thermal properties, the minimum film boiling temperature is

$$T_{MIN} = T_{HN} + (T_{HN} - T_{\ell})\sqrt{\frac{(k\rho C_p)_{\ell}}{(k\rho C_p)_w}} \qquad (4.36)$$

where the homogeneous nucleation temperature is given as a function of pressure by a simple curve fit:

$$T_{HN} = 705.44 - (4.722E\text{-}2)\ DP + (2.3907E\text{-}5)\ DP^2 - (5.8193E\text{-}9)\ DP^3 \qquad (4.37)$$

where $DP = 3203.6 - P$

The minimum film boiling temperature is specified as the larger of either Equation 4.36 or that given by Henry's (Ref. 58) modification of the Berenson correlation:

$$T_{MIN} = T_B + 0.42\ (T_B - T_\ell) \left\{ \sqrt{\frac{(k\rho C_p)_\ell}{(k\rho C_p)_w}}\ \left[\frac{h_{fg}}{C_{pw}(T_B - T_f)}\right] \right\}^{0.6}$$

where

$$T_B = T_f + 0.127\ \frac{\rho_v\ h_{fg}}{k_v} \left[\frac{g(\rho_f - \rho_g)}{(\rho_f + \rho_g)}\right]^{2/3} \left[\frac{g_c \sigma}{g\ (\rho_f - \rho_g)}\right]^{1/2} \left[\frac{\mu_v}{g\ (\rho_f - \rho_g)}\right]^{1/3}$$

In addition, the minimum film boiling temperature is restricted to:

$$800°F \leq T_{MIN} \leq 1200°F$$

Transition Boiling

At present, there is no consensus on a correlation to use for the transition boiling region. The vessel module in COBRA/TRAC uses a simple interpolation scheme (Ref. 74) between the critical heat flux (T_{CHF}, q''_{CHF}) and minimum film boiling (T_{MIN}, q''_{MIN}) point to compute the fraction of the wall that is wettable. This method is simple and physically based, and results in a continuous boiling curve.

It is assumed that the transition boiling heat transfer is composed of both nucleate boiling (wet wall) and film boiling (dry wall) heat transfer, as follows:

$$q''_{TB} = \text{Maximum}\ (0.2,\ 1-\alpha)\ \delta\ q''_{CHF} + q''_{FB} \tag{4.38}$$

where

$$\delta = \left(\frac{T_w - T_{MIN}}{T_{CHF} - T_{MIN}} \right)^2 \tag{4.39}$$

For top quenching, the void fraction can be very large (.95-.99) and yet still produce significant quench rates. Since the void fraction remains near unity, the $(1-\alpha)$ modifier in Equation 4.38 applies too restrictive a constraint upon the transition boiling heat flux. This is overcome by removing the $(1-\alpha)$ from the calculation for a region near the top quench front (the so-called "sputtering" region). An exponential decay as a function of distance is employed;

$$\xi = \text{EXP}\ [-0.299(\Delta Z-1.2)]$$

$$\xi = \text{minimum}\ (1.0,\ \text{maximum}\ (\xi,\ 1-\alpha))$$

where;

ξ = exponential modifier

ΔZ = distance below a top quench front (inches)

and,

$$q''_{TB} = \xi\ \delta q''_{CHF} + q''_{FB}$$

The transition boiling heat flux at a top quench front is not enhanced above the reasonable value of $(\delta\ q''_{CHF})$; rather the amount by which it is decreased as a function of void fraction is reduced. The film boiling heat flux is the value obtained by evaluating the appropriate film boiling correlation (see below).

4.2.6 Dispersed Flow and Inverted Annular Film Boiling

Heat transfer in the film boiling region is assumed to result from one of two mechanisms: dispersed flow film boiling (DFFB) or inverted annular film boiling (TAFB).

Dispersed flow film boiling is selected if the void fraction is greater than 0.8. It is treated by a "two-step" method where the dominant heat transfer mode is forced convection to superheated steam. The steam superheat

is then determined by the interfacial heat transfer rate to the entrained droplets as part of the hydrodynamic solution. Heat fluxes due to wall-droplet radiation and droplet impingement are superimposed upon the vapor convective heat flux. The total heat flux is:

$$q''_{DFFB} = q''_{FC} + q''_{R} + q''_{W-D} \tag{4.40}$$

where $q''_{FC} = H_{SPV} (T_W - T_V)$

H_{SPV} = the Dittus-Boelter correlation

T_V = superheated vapor temperature

q''_R = wall-drop radiation heat flux

q''_{W-D} = drop impingement heat flux

Heat transfer due to droplets striking the wall is evaluated using the Forslund-Rohsenow (Ref. 59) equation:

$$q''_{W-D} = 0.2 \frac{\pi}{4} \left(\frac{6}{\pi}\right)^{2/3} (1-\alpha)^{2/3} \left[\frac{g\rho_f \rho_v h_{fg} k_v^3}{(T_w-T_f) \mu_v \left(\frac{\pi}{6}\right)^{1/3} D_D}\right]^{1/4} \tag{4.41}$$

where D_D = drop diameter, calculated using the entrained void fraction and the droplet number density

The radiative heat transfer, q''_R, is calculated using the model of Sun et al. (Ref. 60) and is discussed later under radiation heat transfer.

When the void fraction is less than 0.6, inverted annular film boiling is assumed to occur. The heat flux for this regime is computed from the larger of either the value calculated in Equation 4.40 for dispersed flow film boiling, or the value from the modified Bromley correlation (Ref. 61);

$$q''_{BROM} = 0.62 \left(\frac{D_H}{\lambda_c}\right)^{0.172} \left[\frac{k_g^3 \rho_g (\rho_f-\rho_g) h'_{fg} g}{D_H \mu_g (T_w-T_f)}\right]^{1/4} (T_w-T_f) \tag{4.42}$$

where $h'_{fg} = h_{fg} [1.0 + 0.4C_{pv} (T_w - T_f)/h_{fg}]$

$$\lambda_c = 2 \pi \left[\frac{g_c \sigma}{g (\rho_f - \rho_g)} \right]^{1/2}$$

The radiation heat flux term q''_{R_I} is defined

$$q''_{R_I} = \frac{\sigma_{SB}}{\frac{1}{\epsilon} + \frac{1}{\alpha_L} - 1} (T_w^4 - T_f^4)$$

where σ_{SB} = Boltzman constant
ϵ = emissivity of heat rods (~0.7)
α_L = absorptivity of liquid (~1.0)

So, for inverted annular film boiling, the heat flux is

$$q''_{IAFB} = q''_{BROM} + q''_{R_I} \tag{4.43}$$

At intermediate void fractions ($0.8 > \alpha > 0.6$), the heat flux is interpolated between the values for inverted annular and dispersed flow film boiling.

Radiation Heat Transfer in Dispersed Flow Film Boiling Regime

The radiation heat transfer model used in the dispersed flow regime was developed by Sun, Gonzalez and Tien (Ref. 60). They demonstrated that if the dispersed flow regime is "optically thin", then the wall, vapor and liquid droplets can be treated as single nodes in a conventional network analysis of radiation heat transfer. Using this assumption, the gray body factors are

$$F_{W-D} = 1/[R_2 \left(1 + \frac{R_3}{R_1} + \frac{R_3}{R_2}\right)]$$

$$F_{W-V} = 1/[R_1 \left(1 + \frac{R_3}{R_1} + \frac{R_3}{R_2}\right)] \qquad (4.44)$$

where

$$R_1 = \frac{1 - \varepsilon_v}{\varepsilon_v (1 - \varepsilon_v \varepsilon_f)}$$

$$R_2 = \frac{1 - \varepsilon_f}{\varepsilon_f (1 - \varepsilon_v \varepsilon_f)} \qquad (4.45)$$

$$R_3 = \frac{1}{1 - \varepsilon_v \varepsilon_f} + \frac{1 - \varepsilon_w}{\varepsilon_w}$$

and

$$\varepsilon_v = 1 - \exp(- a_v L)$$
$$\varepsilon_f = 1 - \exp(- a_f L) \qquad (4.46)$$

The parameter L is the mean beam length and is assumed equal to the hydraulic diameter of the cell. The vapor emissivity (a_v) is assumed equal to 0.02, and the liquid emissivity is

$$a_f = 0.74 \left(\frac{\pi}{4}\right) D_D^2 N_D \qquad (4.47)$$

where N_D is the drop number density.

The radiative heat fluxes are given by

$$q''_{W-D} = F_{W-D}\ \sigma_{SB}\ (T_w^4 - T_f^4)$$

$$q''_{W-V} = F_{W-V}\ \sigma_{SB}\ (T_w^4 - T_v^4) \qquad (4.48)$$

where σ_{SB} is the Boltzman constant.

4.3 QUENCH FRONT MODEL

Coupled thermal-hydraulic numerical simulations of rewetting encounter difficulties with large axial computational mesh spacing (typically, 2 feet for a full vessel) which cannot adequately resolve the axial profile of temperature and surface heat flux across the quench front. During quenching, the entire boiling curve--from film boiling through transition boiling and critical heat flux to nucleate boiling--can be encompassed by one hydrodynamic mesh cell. Constraining the entire cell to be in one boiling regime is nonphysical and results in stepwise cell-by-cell quenching, producing flow oscillations that can obscure the correct hydrodynamic solution. Consequently, an integration of the boiling curve shape through the hydrodynamic computational cell must be performed to determine the fluid heat input.

A fine mesh-rezoning technique (Ref. 62) is employed in the vessel module of COBRA/TRAC to surmount these difficulties. Fine mesh heat transfer cells with axial and radial conduction are superimposed upon the coarse hydrodynamic mesh spacing, and a boiling heat transfer package is applied to each node.

By solving the two-dimensional conduction equation for a variable fine mesh at the quench front, propagation due either to quenching or dryout can be resolved and the surface heat flux integrated to provide the cell-averaged phasic heat inputs for the fluid energy equation. The resulting quench front velocity will be a function of:

- axial conduction
- boiling curve shape
- prequench heat transfer
- internal heat transfer within the rod.

Resolution of axial temperature and surface heat flux excursions is achieved by rezoning the heat conductor mesh in their vicinity. Figure 4.11 illustrates the normal axial noding scheme. Both fluid and rod temperatures are calculated at the centers of the fluid continuity cells. Two extra rod nodes are included at the top and bottom of the rod. When axial temperature differences between adjacent axial nodes exceed splitting criteria (user-specified maximum surface temperature differences) an additional row of nodes is inserted halfway between the two original nodes. (This is illustrated in Figure 4.12.) The temperatures assigned to these nodes are computed so that energy is conserved. This splitting process continues (over a succession of time steps) until the mesh is fine enough to resolve the surface temperature curve to the desired level of detail.

The correct temperature differences to be used as splitting criteria depend on the heat transfer regime. They are further modified by functions of the wall temperature (when the wall temperature is near the critical heat flux temperature) to ensure resolution of the surface heat flux profile in the vicinity of the quench front. The temperatures assigned to the inserted nodes are calculated from an energy balance:

$$Cp_1 (T_1 - T_I) \frac{\Delta X}{2} + Cp_2 (T_2 - T_I) \frac{\Delta X}{2} = 0$$

$$T_I = \frac{(CpT)_1 + (CpT)_2}{(Cp_1 + Cp_2)} \qquad (4.49)$$

where the subscripts I, 1 and 2 represent the inserted and two original nodes, respectively.

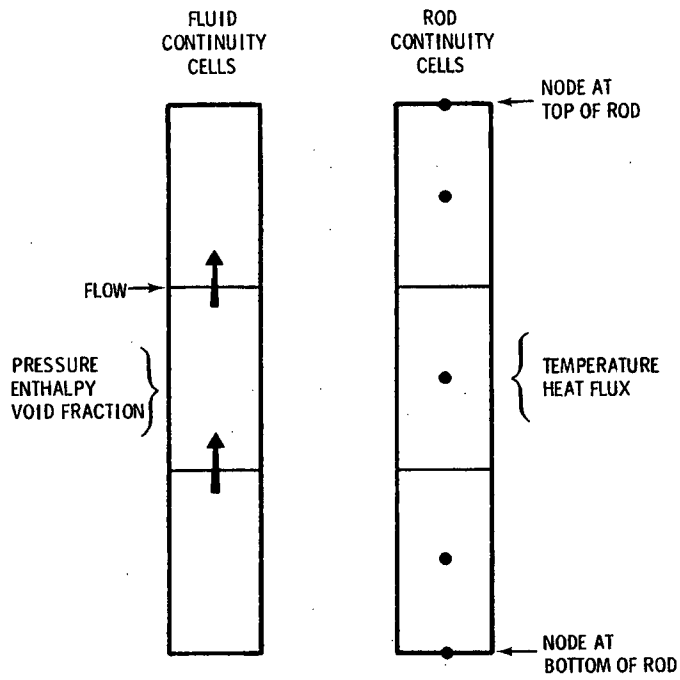

FIGURE 4.11. Example of COBRA-TF Axial Noding Scheme

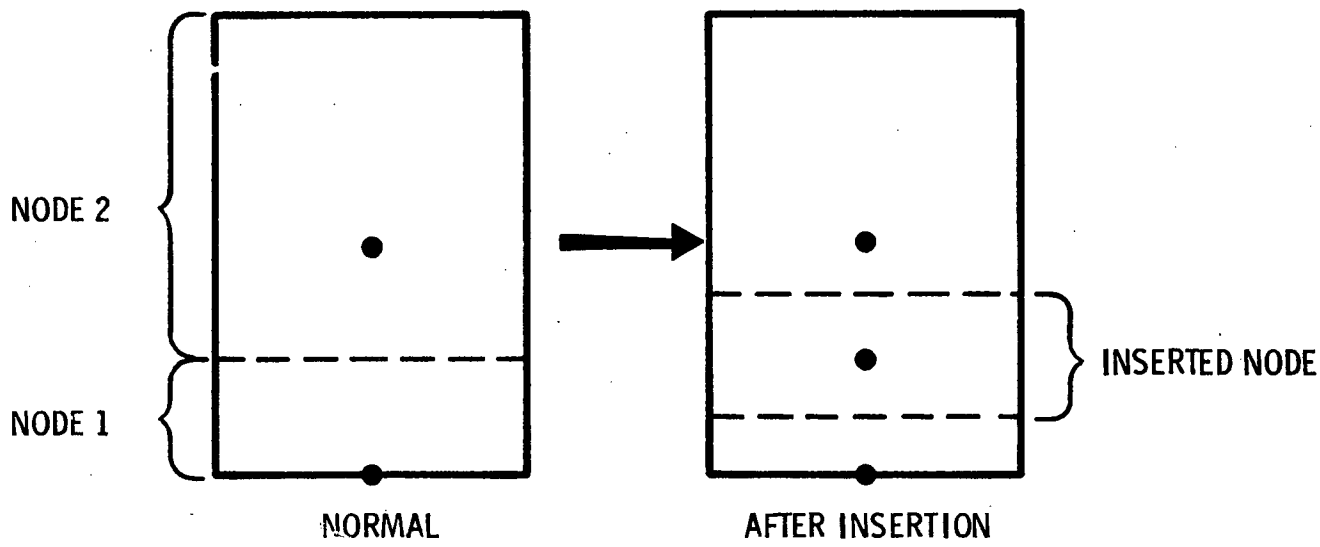

FIGURE 4.12. Example of Node Insertion

Conversely, when a fine mesh has been established, but the disturbance has propagated downstream and the fine mesh is no longer necessary, adjacent nodes can be coalesced back down to one node. The decision to merge cells is based on minimum temperature differences between adjacent nodes. Eventually, all the fine mesh nodes in a region will coalesce, and only the original nodes (those coincident with hydrodynamic scalar mesh cell boundaries) will remain.

The fine mesh-rezoning model differs from other reflood models (such as the one employed in RELAP4/MOD6 (Ref. 63) in that the fine mesh nodes are stationary and do not have a fixed mesh spacing. The fine mesh nodes are split to create a graduated mesh spacing that readjusts itself consonantly to the changing axial temperature gradient. This approach permits node sizes small enough (e.g., 0.05 inches) to resolve axial conduction and the boiling curve shape at the quench front, and yet minimizes the number of nodes required. It ensures conservation of stored energy when cells are added, and simplifies coupling with the hydrodynamic solution. Figures 4.13 and 4.14 (taken from a simulation of a FLECHT low flooding rate test) illustrate the resolution of the cladding temperature profile and the surface heat flux in the vicinity of the quench front.

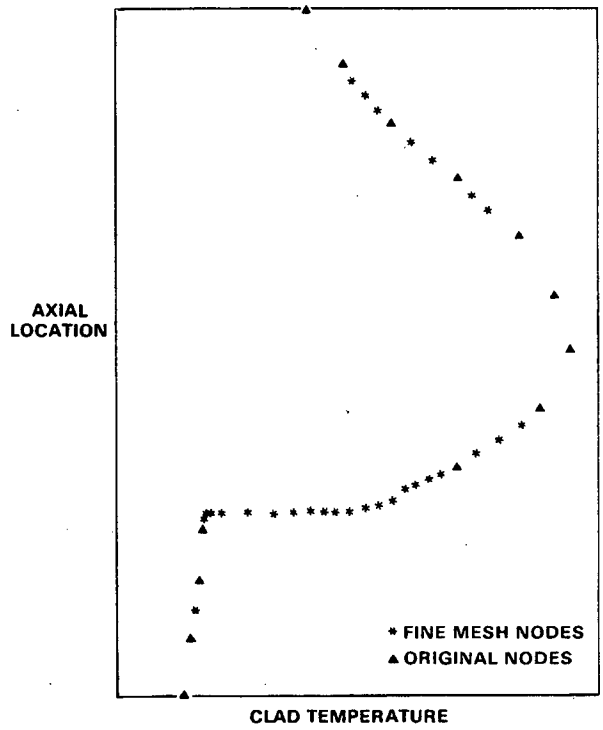

FIGURE 4.13. Fine Mesh Renoding: Cladding Temperature Profile

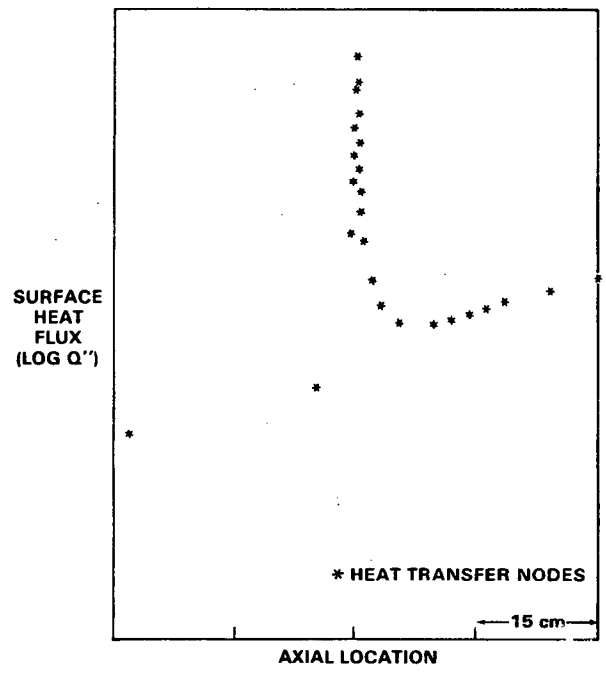

FIGURE 4.14. Fine Mesh Renoding: Surface Heat Flux

4.4 GAP CONDUCTANCE MODEL

The dynamic gap conductance model, originally developed for the VIPRE (Ref. 35) code, computes changes in the fuel rod structure and fill gas pressure that affect the gap conductance and fuel temperature during a transient. The method is based primarily on previous work in the GAPCON (Ref. 37,39) and FRAP (Ref. 36,40,41) series of fuel performance codes but with the mechanics and fill gas pressure models greatly simplified. The material property correlations are taken exclusively from MATPRO-11 (Revision 1) (Ref. 38); refer to Appendix B.

The gap conductance between the fuel outside surface and cladding inside surface has three components:

$$H_{gap} = H_{rad} + H_{gas} + H_{solid} \tag{4.50}$$

where H_{rad} = heat transfer due to thermal radiation
H_{gas} = heat transfer due to conduction in the fill gas
H_{solid} = heat transfer due to physical contact between the fuel pellet and the clad

Each of these terms has associated with it certain models and assumptions. These are discussed in detail below. In all models, the gap is assumed axisymmetric.

4.4.1 Radiant Heat Transfer

The gap conductance due to radiant heat transfer is the ratio of the gap radiant heat flux, q''_r, to the temperature rise across the fuel/cladding gap

$$H_{rad} = \frac{q''_r}{T_1 - T_2} \tag{4.51}$$

The radiant heat flux leaving the fuel surface, q''_r, is determined from the Stefan-Boltzmann equation using appropriate fuel cladding geometry factors, so that

$$q''_r = \sigma_{SB} \left[\frac{1}{\varepsilon_1} + \frac{A_1}{A_2}\left(\frac{1}{\varepsilon_2} - 1\right)\right]^{-1} \left[T_1^4 - T_2^4\right] \qquad (4.52)$$

where A_1 = fuel surface area (ft^2)
A_2 = cladding surface area (ft^2)
ε_1 = fuel surface emissivity
ε_2 = cladding surface emissivity
T_1 = fuel surface temperature (°R)
T_2 = cladding surface temperature (°R)
σ_{SB} = Stefan-Boltzmann constant (1.714×10^{-9} Btu/hr-ft^2-°R^4)

The emissivities of the fuel and cladding are calculated using relations from MATPRO-11 (Revision 1); see Appendix B, Equation B.6. The effect of the cladding oxide layer thickness on the emissivity is neglected.

4.4.2 Conduction Heat Transfer in the Fill Gas

Heat conduction through the fill gas is calculated using the model developed for GAPCON-2 based on a linear regression analysis of Ross-Stoudt data by Lanning and Hann (Ref. 64). For a normal open gap the conductance is

$$H_{gas} = \frac{k_{gas}}{t_g + 1.845\,(g_1+g_2)} \qquad (4.53)$$

where k_{gas} = fill gas mixture thermal conductivity (Btu/hr-ft-°F)
t_g = gas gap width (from deformation model) (ft)
g_1 = fuel pellet temperature jump distances (ft)
g_2 = cladding temperature jump distances (ft)

The temperature jump distances compensate for the nonlinearity of the temperature gradient near the walls and the temperature discontinuities on the wall surface as illustrated in Figure 4.15. The nonlinear temperature gradient is due to the incomplete thermal mixing of the gas molecules near the surface. The surface temperature discontinuity results from the incomplete thermal accommodation of the gas molecules to the surface temperature.

The GAPCON-2 modification of the Lloyd (Ref. 65) model is used to calculate the temperature jump distance. The Lloyd model compares well with available data and is used in both the FRAP and GAPCON-2 codes. The temperature jump distance term is evaluated with the relation[a]

$$(g_1+g_2) = 1.131(10^{-5}) \frac{k_{gas}(\bar{T}_g)^{1/2}}{P_{gas} \sum_{j=1}^{6} \frac{a_j f_j}{(M_j)^{1/2}}} \quad \text{(ft)} \tag{4.54}$$

where k_{gas} = fill gas mixture thermal conductivity (Btu/hr-ft-°F) (see Appendix B)

T_g = gas gap average temperature (°K)

f_j = mole fraction of jth gas

M_j = molecular weight of jth gas

a_j = accommodation coefficient of jth gas

P_{gas} = fill gas pressure (psia)

Measurements for helium and xenon on UO_2 by Ullman et al. (Ref. 66) show that accommodation coefficients are temperature-dependent and vary for different gases. These dependencies are incorporated by using the GAPCON-2 curve fits to the Ullman data.

(a) Note that the equation as written in the GAPCON-2 manual is in error.

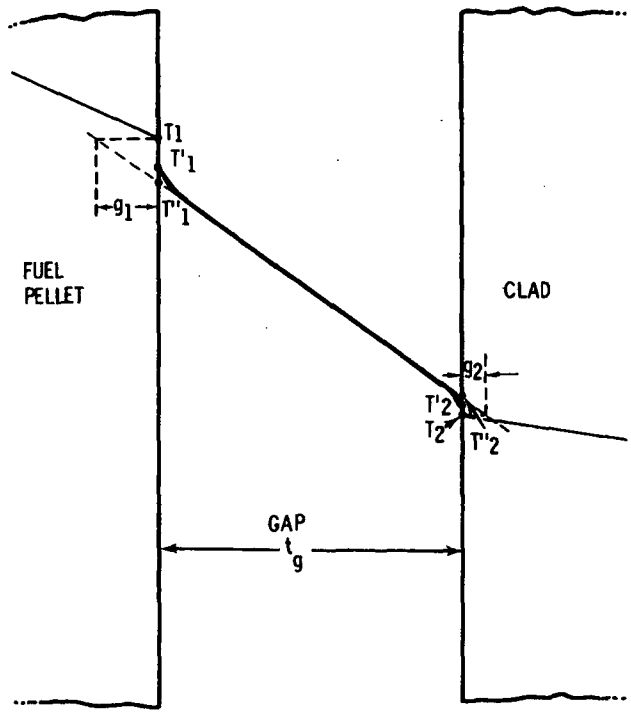

FIGURE 4.15. Illustration of Temperature Jump Distances for an Ideal Gap

$$a_{He} = 0.425 - 2.3(10^{-4})T$$

$$a_{Xe} = 0.749 - 2.5(10^{-4})T \qquad (4.55)$$

where T is in Kelvin (°K).

The accommodation coefficients for other gases are approximated using a linear interpolation between those of helium and xenon based on molecular weight. This was found to correlate the data of Thomas (Ref. 67) with reasonable accuracy.

The gas mixture conductivity, k_{gas}, is determined from the conductivities of the constituent gases using a simplified version of the model in the MATPRO-11 subroutine GTHCON. Since the code uses the temperature jump model described above the free molecular convection (Knudsen) regime correction to the gas conductivity given in MATPRO is not required. The conductivities of

helium, xenon, argon, krypton, hydrogen and nitrogen gas are calculated using correlations from MATRPO-11 (Revision 1). The correlations compare favorably with the Chapman-Enskog theory used in GAPCON but are much easier to implement.

When fuel/cladding contact occurs--from deformation caused by thermal expansion or mechanical stress or a combination of the two--the heat conductance in the gas becomes

$$H_{gas} = \frac{k_{gas}}{\{1.8[C(R_1+R_2) + g_1 + g_2] - 4.2(10^{-7})\}} \tag{4.56}$$

where k_{gas} = fill gas mixture thermal conductivity (determined as for open gap)

g_1, g_2 = fuel pellet and cladding temperature jump distances (determined as for the open gap)

$C = 1.98 \exp[-8.8(10^{-5})]P_i$, dimensionless constant where P_i is the contact pressure (in psi, determined by the deformation model)

Fuel cladding contact is defined to occur when

$$t_g < 3.6\ (R_1+R_2) \tag{4.57}$$

where t_g = gas gap width (from the deformation model; discussed below)

R_1 = mean surface roughness of fuel pellet

R_2 = mean inside surface roughness of cladding

By this criterion, contact is assumed to occur because of waviness and mismatch of the fuel/clad interface when the calculated gap width closes to within 3.6 times the combined surface roughnesses. This was determined by comparing measured gap widths with calculated gap widths from GAPCON (Ref. 68). A more complete discussion is available in the GAPCON-2 manual (Ref. 37).

4.4.3 Fuel/Cladding Contact Conductance

When the fuel and cladding are not in contact, H_{solid} must be zero. But when the deformation model determines that the gap between the fuel and cladding is small enough for contact to occur, the Mikic/Todreas model (Ref. 69,70) is used to determine the contact conductance. Of the available models it provides the best agreement with a wide range of contact conductance data (Ref. 64,71).

In this model, H_{solid} is defined in terms of the physical properties of the materials and the geometry of the interface between them:

$$H_{solid} = \frac{5k_m}{(R_1^2+R_2^2)^{1/2}} \left(\frac{P_{int}}{H_M}\right)^n \left(\frac{R_1}{\lambda_1}\right) \tag{4.58}$$

where $k_m = \frac{2k_1k_2}{k_1+k_2}$

k_1 = fuel thermal conductivity (Btu/hr-ft-°F)

k_2 = cladding thermal conductivity (Btu/hr-ft-°F)

R_1 = mean fuel surface roughness (in.)

R_2 = mean cladding surface roughness (in.)

$\left(\frac{P_{int}}{H_M}\right)$ = the dimensionless ratio of the interface pressure to the Meyer hardness

$\left(\frac{R_1}{\lambda_1}\right)$ = the dimensionless ratio of the mean fuel surface roughness and wave length (distance between peaks)

The interfacial pressure, P_{int}, due to the differential fuel and cladding expansion, is calculated with the fuel deformation model and is nondimensionalized using the Meyer hardness calculated from MATPRO-11 (Revision 1) subroutine CMHARD (Ref. 38). The exponent, n, on the ratio of interfacial pressure to Meyer hardness is defined (Ref. 67) as

$n = 1.0 \qquad (P_{int}/H_M) > 0.01$

$n = 0.5 \qquad (P_{int}/H_M) \leq 0.0001$

For the intermediate range, the ratio is held constant:

$$\left(\frac{P_{int}}{H_M}\right)^n = 0.01 \qquad 0.0001 < (P_{int}/H_M) < 0.01$$

The ratio of fuel surface roughness to wave length is estimated by GAPCON-2 as

$$\left(\frac{R_1}{\lambda_1}\right) = \exp\,[0.5285 * \ln\,(R_1 - 5.738)] \qquad (4.59)$$

where R_1 = the mean fuel surface roughness (microinches).

4.4.4 Deformation Model

The fuel rod deformation model is used to predict changes in the gap width caused by elastic and thermal stresses. Fuel pellet deformation due to thermal expansion and an optional relocation model is computed. Any fuel pellet geometry changes from as-built specifications due to burnup-dependent quantities, such as swelling and densification, are not modeled and should be included in the input cold gap width. For the cladding deformation under both mechanical and thermal stresses is considered. If the fuel/cladding gap is open, elastic deformation may be induced by the difference between the internal gas pressure and the system pressure. When the gap closes, elastic displacement of the cladding by radial expansion of the fuel in contact with it is calculated, but plastic deformation is neglected. Bending stresses or strains in the cladding or fuel are considered insignificant, and creep deformation of the cladding is ignored.

The axial and diametral thermal expansion of the fuel is calculated using the MATPRO-11 (Revision 1) (Ref. 38) FTHEXP subroutine correlation for

thermally induced strain in UO_2. The correlation was simplified by omitting the corrections for molten fuel and mixed oxide (Pu).

In this model, the radial cracks in the fuel are assumed to relieve the hoop and radial stresses, allowing unrestrained radial movement of the fuel in each concentric radial node. The total radial movement at the fuel pellet exterior is the sum of the expansion in all the fuel nodes.

$$(\Delta r_{th})_{fuel} = \sum_{i=1}^{NFUEL} \varepsilon_r(T_i)_j \Delta r_i \tag{4.60}$$

where $\varepsilon_r(T_i)_j$ = thermal strain at axial node j and radial node i
Δr_i = thickness of radial node i
NFUEL = number of radial nodes in the fuel

The stress-free axial thermal expansion of the fuel pellet stack is calculated in an analogous manner. The fuel pellet stack length change due to the thermal expansion is

$$(\Delta \ell_{th})_{fuel} = \sum_{j=1}^{NDX} \varepsilon_Z(\overline{T}_j) \Delta X_j \tag{4.61}$$

where $\varepsilon_Z(\overline{T}_j)$ = thermal strain at axial node j based on volume-averaged radial node temperatures
ΔX_j = height of axial node j
NDX = number of axial nodes

The radial thermal expansion of the cladding is described by

$$(\Delta r_{th})_{clad} = \varepsilon_r(\overline{T}_j)\overline{r} \tag{4.62}$$

where $\varepsilon_r(T_j)$ = radial thermal strain at axial node j based on the average cladding temperature

$\bar{r}$ = cladding mean radius

The axial thermal expansion of the cladding is

$$(\Delta \ell_{th})_{clad} = \sum_{j=1}^{NDX} \varepsilon_Z(T_j) \Delta X_j \tag{4.63}$$

where $\varepsilon_Z(T_j)$ = axial thermal strain at axial node j based on the average cladding temperature at node j

ΔX_j = height of axial node j

When the fuel cladding gap is open, elastic deformation of the cladding is driven by the difference between the fill gas and system pressures. If the gap closes, the cladding deformation is caused by the radial motion of the fuel. In both models the cladding is assumed sufficiently thin for the stress, strain and temperature to be uniform throughout the cladding thickness.

In the open gap elastic deformation model, the cladding is considered as a thin cylindrical shell loaded by internal and external pressures. (Axisymmetric loading and deformation are assumed.) The radial and axial elastic deformation is the result of hoop stress and axial stress caused by pressure difference. These stresses are given by the following equations:

$$\sigma_\theta = \frac{r_i P_i - r_o P_o}{t_c} \tag{4.64}$$

$$\sigma_Z = \frac{\pi r_i^2 P_i - \pi r_o^2 P_o}{\pi (r_o^2 - r_i^2)} \tag{4.65}$$

where r_o = cladding outside radius
r_i = cladding inside radius
t_c = cladding thickness
P_i = internal fill gas pressure (P_G if the gap is open, Equation 4.70; P_{int} if the gap is closed, Equation 4.74)
P_o = system pressure

The radial stress component is neglected, yielding the following relationships from Hook's Law:

$$\varepsilon_\theta = \frac{\Delta r}{\overline{r}} = \frac{1}{E}(\sigma_\theta - \nu\sigma_Z) \tag{4.66}$$

$$\varepsilon_Z = \frac{\Delta \ell}{\ell} = \frac{1}{E}(\sigma_Z - \nu\sigma_\theta) \tag{4.67}$$

where ε_θ = hoop strain
ε_Z = axial strain
E = modulus of elasticity (Young's modulus)
ν = Poisson ratio, $\frac{E}{2G} - 1$ where G = shear modulus

The relations for the cladding radial and axial elastic deformations, then, are

$$(\Delta r_{el})_{clad} = \varepsilon_\theta \overline{r} \tag{4.68}$$

$$(\Delta \ell_{el})_{clad} = \sum_{j=1}^{NDX} \varepsilon_Z \Delta X_j \tag{4.69}$$

where ε_θ = hoop strain at axial node j
$\overline{r}$ = cladding mean radius
ε_Z = axial strain at axial node j
ΔX_j = height of axial node j

The internal fill gas pressure used to determine the cladding elastic deformation when the gap is open is calculated from the relation

$$P_G = \frac{MR}{\frac{V_P}{T_P} + \sum_{j=1}^{NDX} \pi \Delta X_j \left[\frac{(r_{ci}^2 - r_{fo}^2)}{T_G} + \frac{r_v^2}{T_V} + \frac{(r_{fo}^2 - r_f^2)}{T_F}\right]_j} \qquad (4.70)$$

where M = gram-moles of gas in fuel rod

V_P = gas plenum volume, including effects of fuel and cladding axial expansion (ft^3) (from Equations 4.61, 4.63, and 4.69)

T_P = gas plenum temperature (°K) (defined as the outlet fluid temperature + 10 °K)

ΔX_j = computational cell length at axial level j (ft)

r_{ci} = cladding inside radius including thermal and elastic expansion (ft) (from Equations 4.62 and 4.68)

r_{fo} = fuel outside radius including thermal expansion and relocation (ft) (from Equations 4.60, 4.75 and 4.76)

r_f = fuel outside radius including thermal expansion (ft)

R = universal gas constant (6.1313 $\frac{\text{ft-lbf}}{\text{g-mole-}^0\text{K}}$)

r_v = radius of central void (ft) (from input data)

T_G = gas gap temperature (°K)

T_V = central void temperature (°K)

T_F = average fuel pellet temperature (°K)

This is a static lumped pressure model, similar to those in FRAP or GAPCON. The pressure is assumed uniform throughout the fuel pin, with constant fission gas inventory.

The fuel cladding gap width is given by

$$t_g = t_{cold} - (\Delta r_{th})_{fuel} - (\Delta r_{rel})_{fuel} + (\Delta r_{el})_{clad} + (\Delta r_{th})_{clad} \qquad (4.71)$$

where t_{cold} = input value for fuel cladding gap width (including burnup-dependent effects)

$(\Delta r_{th})_{fuel}$ = fuel radial thermal expansion (from Equation 4.60)

$(\Delta r_{th})_{clad}$ = cladding radial thermal expansion (from Equation 4.62)

$(\Delta r_{el})_{clad}$ = cladding radial elastic expansion (from Equation 4.68)

$(\Delta r_{rel})_{fuel}$ = fuel radial relocation (from Equation 4.75 or 4.76)

The value of t_g calculated in Equation 4.71 is used in Equation 4.57 to determine if the gap is open or closed. If the gap is open, the gap conductance is calculated with H_{solid} set to zero. If the gap is closed, the Mikic/Todreas model for H_{solid} must be evaluated. This requires the closed gap deformation model, which is used to determine the interfacial contact pressure needed in Equation 4.58.

In the closed gap deformation model, the cladding is considered as thin-wall tubing with a specified displacement at the inside and pressure loading at the outside surface. The radial fuel displacement that elastically deforms the cladding is applied directly to the cladding and can be calculated as

$$(\Delta r_{th})_{fuel} = (\Delta r_{th})_{clad} + t_g|_L - t_{cold} \qquad (4.72)$$

where $t_g|_L$ = fuel cladding gap width that defines the closed gap (i.e., 3.6 $(R_1 + R_2)$ as in Equation 4.57)

t_{cold} = user-input cold fuel cladding gap width (including burnup-dependent effects)

$(\Delta r_{th})_{fuel}$ = fuel radial thermal expansion (Equation 4.60)

$(\Delta r_{th})_{clad}$ = cladding radial thermal expansion (Equation 4.62)

Fuel deformation due to relocation does not displace the cladding and is therefore not included in Equation 4.72.

Displacement due to radial strain is assumed negligible, so the radial elastic deformation of the cladding must be equal to the applied fuel displacement on the inside surface,

$$(\Delta r'_{th})_{fuel} = (\Delta r_{th})_{fuel} - (\Delta r_{th})_{clad} + t_g|_L - t_{cold}$$

$$(\Delta r_{el})_{clad} = (\Delta r'_{th})_{fuel} \tag{4.73}$$

The fuel cladding interfacial pressure generated by the applied displacement can be computed using the equilibrium stress (Equations 4.64 and 4.65), Hook's Law (Equations 4.66 and 4.67), and the applied displacement, Δr_f. The interfacial pressure is

$$P_{int} = \frac{(\Delta r'_{th})_{fuel} E t_c (r_o^2 - r_i^2)}{\bar{r}[r_i(r_o^2 - r_i^2) - r_i^2 t_c \nu]} + P_o \frac{r_o(r_o^2 - r_i^2) - r_o^2 t_c \nu}{r_i(r_o^2 - r_i^2) - r_i^2 t_c \nu} \tag{4.74}$$

where $(\Delta r'_{th})_{fuel}$ = applied fuel displacement in cladding (from Equation 4.73)

E = modulus of elasticity for the cladding

t_c = cladding thickness

r_o = cladding outside radius

r_i = cladding inside radius

$\bar{r}$ = cladding mean radius

ν = Poisson's ratio for the cladding

P_o = system pressure (on the outside surface of the cladding)

The cladding inside and outside radius (r_o and r_i) and the mean radius ($\bar{r}$) are evaluated with elastic and thermal expansion taken into account. The thermal expansion is evaluated using Equation 4.62, just as in the open gap model. The elastic deformation is evaluated using the relation in Equation 4.68, but the internal pressure P_i is defined as the interfacial pressure P_{int} from Equation 4.74 instead of the fill gas pressure P_G from Equation 4.70.

Fuel relocation is calculated using the FRACAS-I mechanics model from FRAPCON-2 (Ref. 72). FRACAS-I has been chosen for its simplicity and compatibility with the conduction solution. The model allows fuel fragments to move radially into the pellet-cladding gap. Cracks formed in the pellet change the effective conductivity of the fuel. Figure 4.16 illustrates fuel

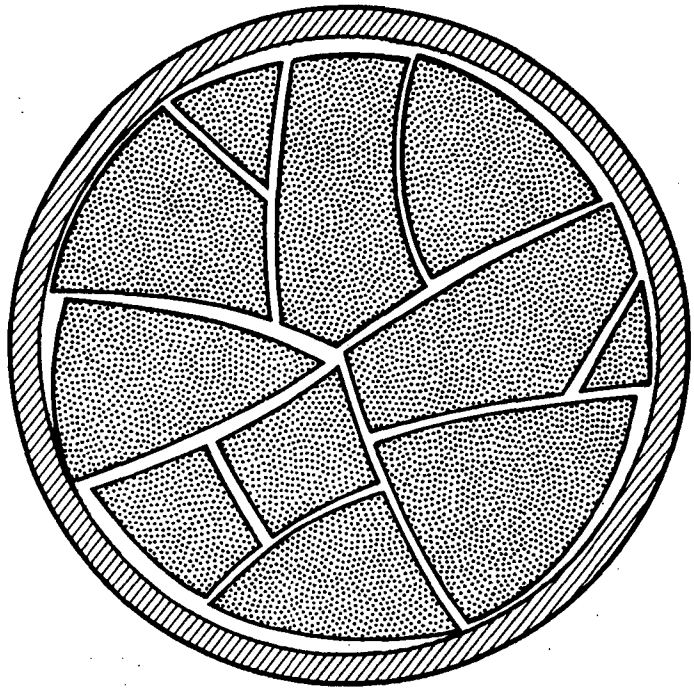

FIGURE 4.16. Illustration of Fuel Relocation

relocation and how cracking changes heat conduction in the radial direction. Gap closure and conductivity degradation provide a more realistic radial temperature profile for nuclear fuel rods than is possible without relocation.

Coleman (Ref. 73) has shown that the amount of relocation necessary for proper gap closure can be expressed as a function of the cold state rod geometry:

$$(\Delta r_{rel})_{fuel} = \delta - 0.005 r_f \qquad (4.75)$$

where $(\Delta r_{rel})_{fuel}$ = fuel radial relocation (ft)

δ = as-fabricated fuel-cladding gap size (ft)

r_f = as-fabricated pellet radius (ft)

The amount of relocation remains constant as long as the fuel-cladding gap is open. When the gap closes, radial displacement due to relocation remains large enough to keep the fuel and cladding in contact without radially displacing the cladding. Cladding is displaced by fuel thermal expansion when the radial displacement of the fuel due to relocation is zero. The amount of fuel relocation in the closed gap case is defined as

$$(\Delta r_{rel})_{fuel} = \delta - (\Delta r_{th})_{fuel} + (\Delta r_{th})_{clad} + (\Delta r_{el})_{clad} \quad (4.76)$$

where $(\Delta r_{rel})_{fuel}$ = fuel radial relocation (ft)
δ = as-fabricated fuel-cladding gap size (ft)
$(\Delta r_{th})_{fuel}$ = fuel radial thermal expansion (ft)
$(\Delta r_{th})_{clad}$ = cladding radial thermal expansion (ft)
$(\Delta r_{el})_{clad}$ = cladding radial elastic expansion (ft)

Gap closure is determined by a gap width of less than or equal to 3.6 times the sum of fuel and cladding mean surface roughness.

When fuel relocates into the pellet-cladding gap the effective conductivity of the fuel is reduced by cracking. FRACAS-I uses an empirical conductivity factor to calculate an effective fuel conductivity when cracks are present.

$$K_{EFF} = R\, K_{LAB} \quad (4.77)$$

where K_{EFF} = effective fuel thermal conductivity (W/m·°K)
K_{LAB} = uncracked fuel thermal conductivity (W/m·°K)
R = conductivity factor

The conductivity factor[a] is a function of gas conductivity and volume available for cracking and is given by

$$R = 1.0 - C\,C_{rel}\,[1.0 - \frac{k_g}{K_{LAB}}] \qquad (4.78)$$

where $C_{rel} = \delta/0.8\times10^{-4}$

δ = as-fabricated fuel cladding gap size (m)

C = 0.30 (1/m)

K_g = thermal conductivity of gas in gap (W/m·°K)

K_{LAB} = uncracked fuel thermal conductivity (W/m·°K)

The factor $(1.0-k_g/K_{LAB})$ accounts for the fact that gas in the cracks has a lower thermal conductivity than the fuel and therefore decreases the effective conductivity of the fuel pellet. C_{rel} is a measure of the volume available for cracking. Since cracked fuel does not fully solidify when compressed, C_{rel} is never less than 0.25. Crack healing is assumed to occur instantly when the local fuel temperature exceeds nine-tenths of the fuel sintering temperature. The conductivity factor is set equal to 1.0 when the fuel temperature exceeds 4304.0°F.

(a) Equation 4.78 is derived by substituting the definition for V into Equation (51) of Reference 72. ($V = 3Uc/r_f = 3(\delta_s-\delta_T)/r_f$)

REFERENCES

1. D. R. Liles and others, "TRAC-PD2, An Advanced Best-Estimate Computer Program for Pressurized Water Reactor Loss-of-Coolant Accident Analysis," USNRC Report NUREG/CR-2054, 1981.

2. M. Ishii, Thermo-Field Dynamic Theory of Two-Phase Flow, Eyrolles. 1975.

3. C. W. Stewart, C. L. Wheeler, R. J. Cena, C. A. McMonagle, J. M. Cuta, and D. S. Trent, "COBRA-IV: The Model and the Method," BNWL-2214, Pacific Northwest Laboratory, Richland, Washington, 1977.

4. D. R. Liles, "Vessel Constitutive Package and Flow Regime Map," LA-NUREG-6924-PR, Nuclear Reactor Safety Quarterly Progress Report, prepared for NRC by Los Alamos Scientific Laboratory, August 1977.

5. S. LeKach, "Development of a Computer Code for Thermal Hydraulics of Reactors (THOR)," BNL-19978, Brookhaven National Laboratory Quarterly Progress Report.

6. A. E. Dukler, "Flow Regime Transitions for Vertical Upward Gas Liquid Flow: A Preliminary Approach Through Physical Modeling," USNRC Report NUREG-0162, University of Houston, January 1977. Available for purchase from National Technical Information Service, Springfield, Virginia, 22161.

7. T. W. Lovell, "The Effect of Scale on Two-Phase Countercurrent Flow Flooding in Vertical Tubes," Masters Thesis, Thayer School of Engineering, Dartmouth College, 1977.

8. A. E. Dukler and L. Smith, "Two-Phase Interactions in Countercurrent Flow Studies of the Flooding Mechanism," NUREG/CR-0617, Annual Report, January 1979. Available for purchase from National Technical Information Service, Springfield, Virginia, 22161.

9. M. Ishii," Drift Flux Model and Constitutive Equations for Relative Motion Between Phases in Various Two-Phase Flow Regimes," ANL-77-47, October 1977.

10. P. N. Rowe, K. T. Claxton and J. B. Lewis, "Heat Transfer from a Single Sphere in an Extensive Flowing Fluid," Transaction of the Institute of Chemical Engineers, 43, T14-T31, (1965).

11. Andersen, Jens G. Munthe, REMI/HEAT COOL, A Model for Evaluation of Core Heat-up and Emergency Core Spray Cooling System Performance for Light-Water Cooled Nuclear Power Reactors, "Heat Transfer in a Spherical Droplet," Report No. 296, RISO National Laboratory, Denmark, September 1973.

12. D. Moalem and S. Sideman, "The Effect of Motion on Bubble Collapse," International Journal of Heat and Mass Transfer 16, 2331-2329 (1973).

13. G. A. Hughmark, "Film Thickness, Entrainment, and Pressure Drop in Upward Annular and Dispersed Flow," AIChE Journal 14, 1062 (1973).

14. G. B. Wallis, "Annular Two-Phase Flow, Part I: Simple Theory," Journal of Basic Engineering (March 1970).

15. F. W. Dittus and L. M. K. Boelter, University of California Engineering Publications, Vol. 2, 443, 1930.

16. P. Ihle, "Flooding Experiments in Blocked Arrays," paper presented at the Eighth Water Reactor Safety Research Information Meeting, Gaithersburg, Maryland, October 1980.

17. W. H. Henstock and T. J. Hanratty, "The Interfacial Drag and the Height of the Wall Layer in Annular Flows," AIChE Journal 22 (6), 990-1000 (November 1976).

18. D. A. Drew and R. T. Lahey, Jr., "Application of General Constitutive Principles to the Derivation of Multidimensional Two-Phase Flow Equations," International Journal of Multiphase Flow, (1979).

19. G. F. Hewitt and N. S. Hall-Taylor, Annular Two-Phase Flow, Pergamon Press, Oxford, Great Britian, 1970.

20. D. E. Woodmansee and T. J. Hanratty, "Mechanism for the Removal of Droplets from a Liquid Surface by a Parallel Air Flow," Vol. 24, 299-307, 1969.

21. M. Ishii and M. A. Grolmes, "Inception Criteria for Droplet Entrainment in Two-Phase Concurrent Film Flow," AIChE Journal 21(2), 308 (1975).

22. P. B. Whalley, G. F. Hewitt, and P. Hutchinson, Experimental Wave and Entrainment Measurements in Vertical Annular Two-Phase Flow, AERE-R7521, Atomic Energy Research Establishment, Harwell, England, 1973.

23. J. Wurtz, "An Experimental and Theoretical Investigation of Annular Steam-Water Flow in Tubes and Annuli at 30 to 90 Bar," Report No. 372, RISO National Laboratory, Denmark, April 1978.

24. I. I. Paleev and B. S. Filippovich, "Phenomena of Liquid Transfer in Two-Phase Dispersed Annular Flow," International Journal Heat Mass Transfer, 9, 1089-1093 (1966).

25. D. F. Tatterson and others, "Drop Sizes in Annular Gas-Liquid Flows," AIChE Journal 23 (1), 68-76 (January 1977).

26. L. B. Cousins, W. H. Denton, and G. F. Hewitt, "Liquid Mass Transfer in Annular Two-Phase Flow," Paper C4 presented at the Symposium on Two-Phase Flow Volume 2, Exeter, England, June 1965, pages (401-430).

27. P. B. Whalley, "The Calculation of Dryout in a Rod Bundle," International Journal of Multiphase Flow 13, 501-515 (1977).

28. NRC Steam Generator Workshop, Silver Spring, Maryland,April 1979.

29. J. C. Dallman and W. L. Kirchner, Los Alamos Scientific Laboratory, "De-Entrainment Phenomena on Vertical Tubes in Droplet Cross Flow," USNRC Report NUREG/CR-1421, April 1980. Available for purchase from National Technical Information Service, Springfield, Virginia, 22161.

30. R. C. Hendricks and others, "WASP - Flexible FORTRAN IV Computer Code for Calculating Water and Steam Properties," NASA TND-7391, Lewis Research Center, Cleveland, Ohio, 1973.

31. ASME Steam Tables, 1967, American Society of Mechanical Engineers, 2nd Edition, 1968.

32. J. H. McFadden and others, "RETRAN-02 A Program for Transient Thermal-Hydraulic Analysis of Complex Fluid Flow Systems, Volume 1: Equations and Numbers," Report NP-1850, Electric Power Research Institute, Palo Alto, California, May 1980.

33. J. H. Keenan and F. G. Keyes, Thermodynamic Properties of Steam, New York, John Wiley & Sons, 1936.

34. R. B. McClintock and G. J. Silvestri, Formulations and Iterative Procedures for the Calculation of Properites of Steam, American Society of Mechanical Engineers, 1936.

35. C. W. Stewart and others, "VIPRE-01 A Thermal-Hydraulics Analysis Code for Reactor Cores: Volume 1, Mathematical Modeling," Electric Power Research Institute, Palo Alto, California, NP-2511, December 1982.

36. J. A. Dearien and others, "FRAP-S3: A Computer Code for the Steady-State Analysis of Oxide Fuel Rods--Report I, Analytical Models and Input Manual," TFBP-TR-164, Idaho National Engineering Laboratory, Idaho Falls, Idaho, October 1977.

37. C. E. Beyer and others, "GAPCON-THERMAL-2: A Computer Program for Calculating the Thermal Behavior of an Oxide Fuel Rod," BNWL-1898, Pacific Northwest Laboratory, Richland, Washington, November 1975.

38. D. L. Hagrman, G. A. Reymann, and R. E. Manson, Idaho National Engineering Laboratories, "MATPRO-Version 11 (Revision 1): A Handbook of Materials Properties for Use in the Analysis of Light Water Reactor Fuel Rod Behavior," USNRC Report NUREG/CR-0497, TREE-1290, Revision 1, February 1980.

39. D. D. Lanning and others, "GAPCON-THERMAL-3 Code Description." PNL-2434, Pacific Northwest Laboratory, Richland, Washington. Available for purchase from National Technical Information Service, Springfield, Virginia, 22161.

40. L. J. Siefken and others, Idaho National Engineering Laboratory, "FRAP-T5: A Computer Code for Transient Analysis of Oxide Fuel Rods," NUREG/CR-0840 TREE-1281, June 1979. Available for purchase from National Technical Information Service, Springfield, Virginia, 22161.

41. G. A. Berna and others, "FRAPCON-1: A Computer Code for the Steady-State Analysis of Oxide Fuel Rods," CDAP-TR-032-R1, Idaho National Engineering Laboratory, Idaho Falls, Idaho, November 1978.

42. C. L. Wheeler and others, "COBRA-IV-I: An Interim Version of COBRA for Thermal-Hydraulic Analysis of Rod Bundle Nuclear Fuel Elements and Cores," BNWL-1962, Pacific Northwest Laboratory, Richland, Washington, March 1973.

43. D. S. Trent and J. R. Welty, "A Summary of Numerical Methods for Solving Transient Heat Conduction Problems," Bulletin No. 49, Engineering Experimental Station, Oregon State University, Corvallis, Oregon, 1974.

44. W. H. McAdams, Heat Transfer, p. 378, McGraw-Hill, New York, 1954.

45. E. M. Sparrow, A. L. Loeffler, and H. A. Hubbard, "Heat Transfer to Longitudinal Laminar Flow Between Cylinders," Journal of Heat Transfer 83, 415 (1961).

46. J. C. Chen, "A Correlation for Boiling Heat Transfer to Saturated Fluids in Convective Flow," ASME 63-HT-34, American Society of Mechanical Engineers, 1963.

47. J. G. Collier, Convective Boiling and Condensation, McGraw-Hill Book Co., England, 1972.

48. F. D. Moles and J. F. G. Shaw, "Boiling Heat Transfer to Subcooled Liquids Under Conditions of Forced Convection," Transactions of the Institute of Chemical Engineers, 50 (1972).

49. W. T. Hancox and W. B. Nicoll, "A General Technique for the Prediction of Void Distributions in Non-Steady Two-Phased Forced Convection," International Journal of Heat and Mass Transfer 14 (1971).

50. S. Z. Rouhani and E. Axelsson, "Calculation of Void Volume Fraction in Subcooled and Quality Boiling Regions," International Journal of Heat and Mass Transfer 13 (1970).

51. C. W. Stewart and others, "Improvements to the COBRA-TF(EPRI) Computer Code for Steam Generator Analysis," Report NP-1509, Electric Power Research Institute, Palo Alto, California, September 1980.

52. M. J. Thurgood and others, "COBRA-TF Development," paper presented at the Eighth Water Reactor Safety Information Meeting, Gaithersburg, Maryland, October 1980.

53. N. Zuber and others, "The Hydrodynamics Crisis in Pool Boiling of Saturated and Subcooled Liquids," Part II, No. 27, p. 23-236 in International Developments in Heat Transfer. International Heat Transfer Conference, Boulder, Colorado, 1961.

54. L. Biasi and others, "Studies on Burnout, Part 3," Energia Nucleare, 14 (9), 530-536 (1967).

55. P. B. Whalley, P. Hutchinson and G. F. Hewitt, "The Calculation of Critical Heat Flux in Forced Convection Boiling," Report No. AERE-R7520, Atomic Energy Research Establishment, Harwell, England, 1973.

56. P. B. Whalley, "The Calculation of Dryout in a Rod Bundle," Report No. AERE-R8319, Atomic Energy Research Establishment, Harwell, England, April 1976.

57. A. W. Bennett and others, "Heat Transfer to Steam-Water Mixtures Flowing in Uniformly Heated Tubes in Which the Critical Heat Flux has been Exceeded," Report No. AERE-R5373, Atomic Energy Research Establishment, Harwell, England, 1967.

58. R. E. Henry, "A Correlation for the Minimum Film Boiling Temperature," AIChE Symposium Series, 70 (138), 81-90 (1974).

59. R. P. Forslund and W. M. Rohsenow, "Dispersed Flow Film Boiling," Journal of Heat Transfer 90 (6), 399-407 (1968).

60. K. H. Sun and others, "Calculations of Combined Radiation and Convection Heat Transfer in Rod Bundles Under Emergency Cooling Conditions," ASME 75-HT-64, American Society of Mechanical Engineers, 1975.

61. L. A. Bromley, "Heat Transfer in Stable Film Boiling," Chemical Engineering Progress 46 (5), 221-226 (1950).

62. J. M. Kelly, "Quench Front Modeling and Reflood Heat Transfer in COBRA-TF," paper 79-WA/HT-63, ASME Winter Annual Meeting, New York, New York, 1979.

63. Idaho National Engineering Laboratory. "RELAP4/MOD6: A Computer Program for Transient Thermal-Hydraulic Analysis of Nuclear Reactors and Related Systems," Report PG-R-77-06, Idaho National Engineering Laboratory, Idaho Falls, Idaho, March 1977.

64. D. D. Lanning and C. R. Hann, "Review of Methods Applicable to the Calculation of Gap Conductance in Zircaloy-Clad UO_2 Fuel Rods," BNWL-1894, Pacific Northwest Laboratory, Richland, Washington, April 1975.

65. W. R. Lloyd and others, "Heat Transfer in Multicomponent Monatomic Gases in the Low, Intermediate, and High Pressure Regime," paper presented at the Nuclear Thermionics Conference, 1973.

66. A. Ullman, R. Acharya, and D. R. Olander, "Thermal Accommodation Coefficients of Inert Gases on Stainless Steel and UO_2," Journal of Nuclear Materials 51, 277-279 (1974).

67. L. B. Thomas, Fundamentals of Gas-Surfacing Interactions, pp. 346-369, H. Saltsburg et al., eds., Academic Press, New York, 1967.

68. C. R. Hann, C. E. Beyer, and L. J. Parchen, "GAPCON-THERMAL-1: A Computer Program for Calculating the Gap Conductance in Oxide Fuel Pins." BNWL-1778, Pacific Northwest Laboratory, Richland, Washington, September 1973.

69. M. G. Cooper, B. B. Mikic, and M. M. Yavonovich, "Thermal Contact Conductance," Journal of Heat and Mass Transfer 12 (1969).

70. N. Todreas and G. Jacobs, "Thermal Contact Conductance of Reactor Fuel Elements," Nuclear Science and Engineering 50, 283 (1973).

71. J. E. Garnier and S. Begej, Pacific Northwest Laboratory, "Ex-Reactor Determination of Thermal Gap and Contact Conductance Between Uranium Dioxide: Zircaloy Interfaces. Stage 1: Low Gas Pressure," USNRC Report NUREG/CR-0330, April 1979. Available for purchase from National Technical Information Service, Springfield, Virginia, 22161.

72. G. A. Berna and others, EG&G, "FRAPCON-2: A Computer Code for the Calculation of Steady-state Thermal-Mechanical Behavior of Oxide Fuel Rods," USNRC Report NUREG/CR-1845, January 1981. Available for purchase from National Technical Information Service, Springfield, Virginia, 22161.

73. D. R. Coleman and E. T. Laats, Idaho National Engineering Laboratory, "FRAP-T3, A Computer Code for the Transient Analysis of Oxide Fuel Rods - Model Assessment Report," USNRC Report NUREG/CR-0555, TREE-1320, February 1979. Available for purchase from National Technical Information Service, Springfield, Virgina 22126.

74. T. A. Bjornard and P. Griffith, "PWR Blowdown Heat Transfer," Thermal and Hydraulic Aspects of Nuclear Reactor Safety, American Society of Mechanical Engineers, New York, Vol. 1, p 17-41, 1977.

APPENDIX A

TWO FLUID PHASIC CONSERVATION EQUATIONS

APPENDIX A
TWO FLUID PHASIC CONSERVATION EQUATIONS

APPENDIX NOMENCLATURE

e	internal energy
$\underline{f}$	body force
$\underline{g}$	acceleration of gravity
h	enthalpy
I	phase interface
$\underline{\underline{I}}$	identity tensor
k	thermal conductivity
$1/L_j$	surface area concentration for the jth interface
$1/L_s$	total surface area concentration
$\underline{M}$	interfacial momentum exchange
$\underline{M}^d$	interfacial drag force
$\underline{M}^\Gamma$	interfacial momentum exchange due to phase change
$\dot{m}$	mass flow rate
$\underline{n}$	unit exterior normal vector
P	pressure
$\underline{Q}$	conduction heat flux
$\dot{Q}$	volumetric heat generation rate
$\underline{q}^T$	turbulent heat flux
q_I'''	interfacial heat transfer per unit volume
S	phase interface
$\underline{\underline{T}}$	stress tensor
$\underline{\underline{T}}^T$	turbulent (Reynolds) stress tensor
T	temperature
$\underline{t}$	stress vector
t	time
Δt	averaging time interval
$\underline{U}$	fluid velocity
$\underline{U}_I$	interface velocity
$\underline{V}$	velocity of volume V

V	arbitrary volume
$\underline{x}$	position vector

Greek Symbols

∂V	boundary of V
v_j	normal displacement speed of interface j
α	void fraction
β	phase function
Γ	net rate of interfacial mass transfer per unit volume
Λ	net rate of interfacial energy transfer per unit volume
λ	second viscosity coefficient
μ	viscosity
ρ	density
$\underline{\Sigma}$	surface tension vector
$\underline{\underline{\tau}}$	viscous stress tensor (stress deviator)
ψ	arbitrary fluid property

Subscripts

1	phase 1
2	phase 2
1_I	phase 1 interfacial limit
2_I	phase 2 interfacial limit
I	interfacial
j	jth interface
k	phase k
k_I	phase k interfacial limit

Superscripts

i	interfacial surface average
m	material
T	turbulent
t	transpose

A.1 INTRODUCTION

This appendix describes the derivation of the average phasic conservation equations for the two-fluid model of multiphase flow. In recent years numerous derivations of conservation equations for multiphase flows have appeared in the literature. Among the more rigorous are the works of Drew (Ref. 1), Vernier and Delhaye (Ref. 2), and Ishii (Ref. 3). All of these authors rely on some form of averaging; that is, average variables are introduced, and conservation equations are derived in terms of the average variables.

Average equations for multiphase flow fall into two broad categories: the two-fluid model and the mixture model. The two-fluid model uses separate conservation equations for each phase and requires additional models for the interactions between phases. The mixture model treats the multiphase mixture as a whole and has only one set of conservation equations plus a diffusion equation. Specific examples of the mixture approach include the homogeneous, slip and drift flux models. Although the two-fluid formulation involves the solution of additional equations, it is capable of modeling more complex situations than the mixture model, and it has greater physical appeal. Because of this greater versatility, the two-fluid model is used exclusively in COBRA-TF.

At the heart of any derivation of two-fluid conservation equations is the choice of the averaging method. Ishii uses Eulerian time averaging to obtain variables that are continuous in time (Ref. 3). Since only one integration is used, his variables are not continuously differentiable in time. They are not even continuous in space. Ishii explains this by noting that differential operations on the average variables are to be interpreted as finite-difference operations in the applications. Drew obtains continuously differentiable average variables by using two integrations in both space and time (Ref. 1). Vernier and Delhaye use various combinations of space and time averaging, depending on the application (Ref. 2). Regardless of the type of averaging used, the resulting average equations are quite similar in form. The differences arise in the definition and physical interpretation of the average

variables and in the constitutive assumptions required to close the set of equations.

This appendix does not attempt to give a completely detailed derivation of all the equations for the two-fluid formulation of multiphase flow. The main features applicable to COBRA-TF are developed here, with references to the original work for the more involved derivations and proofs. The methods and notation of Ishii (Ref. 3) have been used here, since these have won wide acceptance and are more commonly used in the nuclear industry. However, some changes have been made in the notation for the average variables to make the notation less cumbersome.

The two-fluid model is usually derived by considering a mixture of only two phases. To keep this derivation as straightforward and uncluttered as possible, the two phase approach is used here. However, since the general phasic conservation equations obtained will have exactly the same form for any phase, the generalization to n phases is immediate. In particular, the two-fluid model can easily be extended to obtain the three-field formulation used in COBRA-TF.

This appendix is organized into six sections. Section A.2 presents the basic integral theorems needed to study continuum mechanics with surfaces of discontinuity. In Section A.3 exact integral conservation equations applicable to single-phase or two-phase flow are derived. These equations are used to obtain differential conservation equations for single-phase regions in Section A.4. In Section A.5 the integral conservation equations are used to derive interfacial jump conditions for two-phase flow. Average variables are introduced in Section A.6, and the average phasic conservation equations are derived in Section A.7.

A.2 INTEGRAL THEOREMS

Several integral theorems are used in the derivations given in this appendix. The divergence theorem is used in deriving the single-phase differential conservation equations. Leibnitz's theorem, or one of its many variations, is used in deriving the single- and two-phase integral conservation equations. Leibnitz's theorem is also used to obtain derivative

relations for the average variables. This section presents, without proof, these important theorems.

A.2.1 The Divergence Theorem

An arbitrary volume of fluid, V(t), is shown in Figure A.1. It is assumed that V(t) is located in a single-phase region and that the boundary of V(t), ∂V(t), is piecewise smooth. The volume V(t) need not be a material volume. Let $\underline{n}$ denote the unit exterior normal to V(t), and let $\underline{a}(\underline{x},t)$ be any vector function that is continuously differentiable in some region containing V(t). For this situation the divergence theorem (Ref. 4) yields

$$\int_{V(t)} \nabla \cdot \underline{a}\, d\underline{x} = \int_{\partial V(t)} \underline{n} \cdot \underline{a}\, ds \qquad (A.1)$$

This theorem also holds if a continuously differentiable tensor function, $\underline{A}$, replaces $\underline{a}$ in Equation A.1.

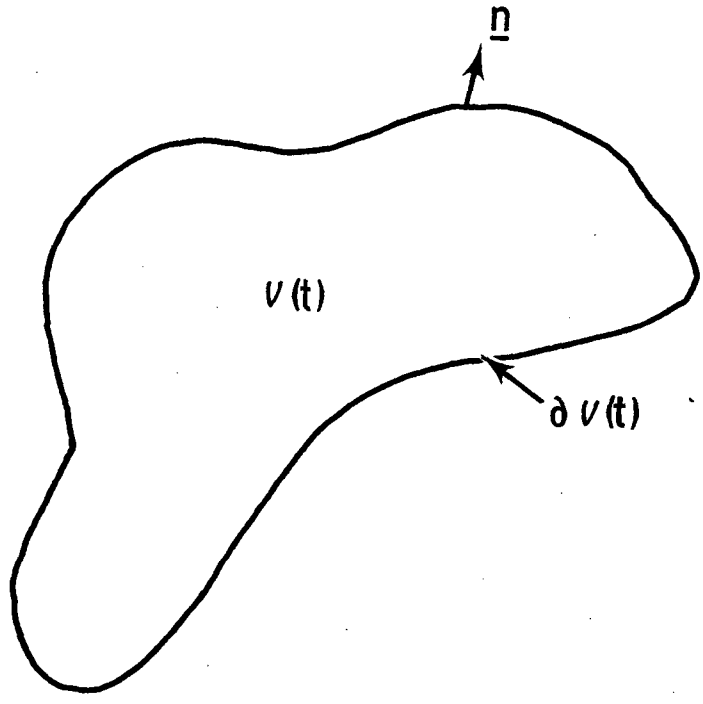

FIGURE A.1. Single-Phase Volume

A.2.2 Leibnitz's Theorem

The basic Leibnitz theorem (Ref. 5) states that if $g(x)$ and $h(x)$ are continuously differentiable for $a \leq x \leq b$, and if $f(x,y)$ is continuously differentiable in a region containing R: $\{(x,y) \mid a \leq x \leq b,\ g(x) \leq y \leq h(x)\}$, then in R

$$\frac{d}{dx} \int_{g(x)}^{h(x)} f(x,y)\, dy = \int_{g(x)}^{h(x)} \frac{\partial f}{\partial x}\, dy + f[x,h(x)] \frac{dh}{dx} - f[x,g(x)] \frac{dg}{dx} \qquad (A.2)$$

This theorem can be generalized to multiple integrals and is used extensively in both single-phase and two-phase derivations.

Single-Phase Case

In addition to the nomenclature introduced in Figure A.1, let

$\underline{V}(\underline{x},t)$ = translational velocity of $V(t)$
$\rho(\underline{x},t)$ = fluid density
$\underline{U}(\underline{x},t)$ = fluid velocity
$\psi(\underline{x},t)$ = any fluid mass specific property (scalar, vector or tensor)

Then, assuming all variables are continuously differentiable, Leibnitz's theorem generalizes to (Ref. 6)

$$\frac{d}{dt} \int_{V(t)} \rho\psi d\underline{x} = \int_{V(t)} \frac{\partial}{\partial t} (\rho\psi)\, d\underline{x} + \int_{\partial V(t)} \underline{n} \cdot (\rho\psi \underline{V})\, ds \qquad (A.3)$$

If $V(t)$ is a material volume, the fluid velocity $\underline{U}$ replaces $\underline{V}$, and Equation A.3 reduces to the Reynolds transport theorem.

Two-Phase Case

The volume $V(t)$ may contain two phases separated by a singular surface, $I(t)$, as illustrated in Figure A.2. For this situation Leibnitz's theorem becomes (Ref. 6)

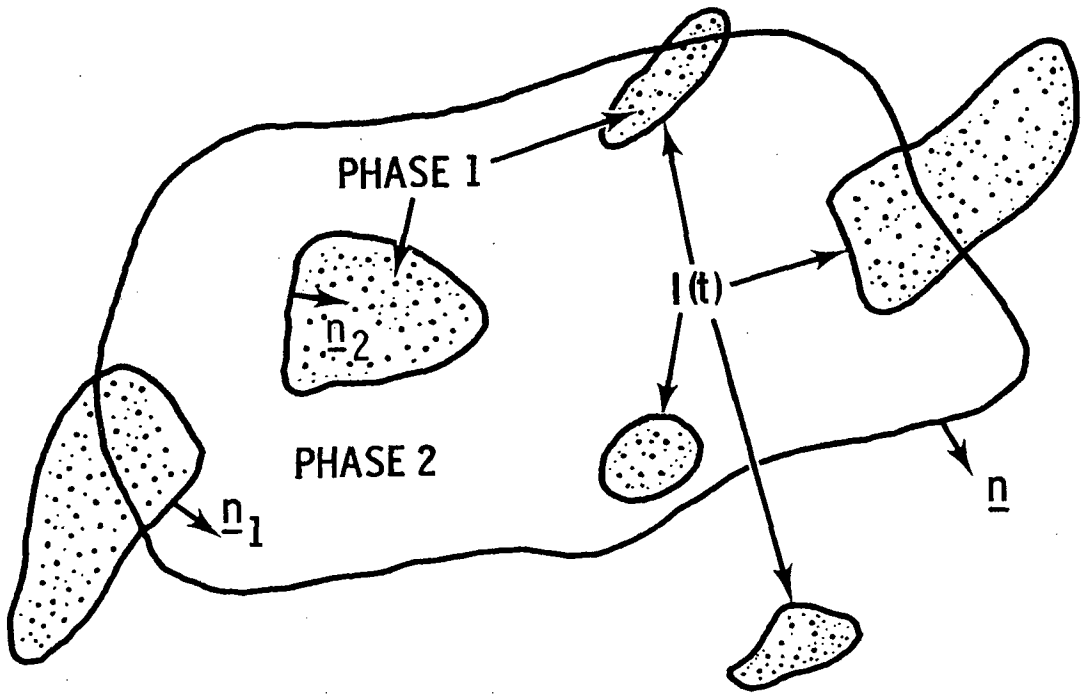

FIGURE A.2. Two-Phase Volume

$$\frac{d}{dt}\int_{V(t)} \rho\psi d\underline{x} = \int_{V(t)} \frac{\partial}{\partial t}(\rho\psi)\, d\underline{x} + \int_{\partial V(t)} \underline{n} \cdot (\rho\psi \underline{V})\, ds$$

$$+ \int_{S(t)} (\rho_{1_I}\psi_{1_I} - \rho_{2_I}\psi_{2_I})\,(\underline{n}_1 \cdot \underline{U}_I)\, ds \qquad (A.4)$$

where S(t) = that portion of I(t) interior to V(t)

$\underline{n}_k$ = unit exterior normal to phase k

$\underline{U}_k$ = velocity of surface I(t)

ψ_{k_I} = interface limit quantity for phase k

The interface limit quantities introduced in Equation A.4 are defined by

$$\psi_{k_I} = \lim_{\substack{\underline{x} \to \underline{x}_I \in I \\ \underline{x} \in \text{phase k}}} \psi(\underline{x},t) \qquad (A.5)$$

A.3 EXACT INTEGRAL EQUATIONS

Exact integral conservation equations are derived by applying Equation A.4 to a material volume that may contain two phases. Let $V^m(t)$ denote such a volume.

Mass

Conservation of mass requires

$$\frac{d}{dt} \int_{V^m(t)} \rho \, d\underline{x} = 0 \tag{A.6}$$

Applying Equation A.4 yields

$$\int_{V^m(t)} \frac{\partial \rho}{\partial t} \, d\underline{x} + \int_{\partial V^m(t)} \rho(\underline{n} \cdot \underline{U}) \, ds + \int_{S(t)} (\rho_{1_I} - \rho_{2_I}) (\underline{n}_1 \cdot \underline{U}_I) \, ds = 0 \tag{A.7}$$

Momentum

Conservation of momentum requires

$$\frac{d}{dt} \int_{V^m(t)} \rho \underline{U} \, d\underline{x} = \int_{\partial V^m(t)} \rho \underline{f} \, d\underline{x} + \int_{\partial V^m(t)} \underline{t} \, ds + \int_{\partial V^m(t) \; I(t)} \underline{\Sigma} \, d\ell \tag{A.8}$$

where $\underline{f}$ = body force per unit mass

$\underline{t}$ = stress vector

$\underline{\Sigma}$ = surface tension vector.

Applying Equation A.4 yields

$$\int_{V^m(t)} \frac{\partial}{\partial t}(\rho \underline{U})d\underline{x} + \int_{\partial V^m(t)} \underline{n} \cdot (\rho \underline{U}\underline{U})ds = \int_{V^m(t)} \rho \underline{f}\, d\underline{x} + \int_{\partial V^m(t)} \underline{t}\, ds$$

$$+ \int_{\partial V^m(t)} \int_{I(t)} \underline{\Sigma}\, d\ell - \int_{S(t)} (\rho_{1_I} \underline{U}_{1_I} - \rho_{2_I} \underline{U}_{2_I})(\underline{n}_1 \cdot \underline{U}_I)\, ds \qquad (A.9)$$

Energy

Conservation of energy requires

$$\frac{d}{dt} \int_{V^m(t)} \rho(e + \tfrac{1}{2}|\underline{U}|^2)\, d\underline{x} = \int_{\partial V^m(t)} -\underline{Q} \cdot \underline{n}\, ds + \int_{V^m(t)} \dot{Q}\, d\underline{x}$$

$$+ \int_{V^m(t)} \rho\, \underline{f} \cdot \underline{U}\, d\underline{x} + \int_{\partial V^m(t)} \underline{t} \cdot \underline{U}\, ds + \int_{\partial V^m(t)} \int_{I(t)} \underline{\Sigma} \cdot \underline{U}_I\, d\ell \qquad (A.10)$$

where e = specific internal energy

$\underline{Q}$ = conduction heat flux vector

$\dot{Q}$ = volumetric heat generation rate

Applying Leibnitz's theorem yields

$$\int_{V^m(t)} \frac{\partial}{\partial t}[\rho(e + \tfrac{1}{2}|\underline{U}|^2)]d\underline{x} + \int_{\partial V^m(t)} \underline{n} \cdot [\rho(e + \tfrac{1}{2}|\underline{U}|^2)\underline{U}]\, ds$$

$$= -\int_{\partial V^m(t)} \underline{Q} \cdot \underline{n}\, ds + \int_{V^m(t)} \dot{Q}\, d\underline{x} + \int_{V^m(t)} \rho \underline{f} \cdot \underline{U}\, dx + \int_{\partial V^m(t)} \underline{t} \cdot \underline{U}\, ds$$

$$+ \int_{\partial V^m(t)} \int_{I(t)} \underline{\Sigma} \cdot \underline{U}_I\, d\ell - \int_{S(t)} [\rho_{1_I}(e + \tfrac{1}{2}|\underline{U}|^2)_{1_I} - \rho_{2_I}(e + \tfrac{1}{2}|\underline{U}|^2)_{2_I}](\underline{n}_1 \cdot \underline{U}_I)\, ds \qquad (A.11)$$

Equations A.7, A.9 and A.11 cannot be used directly to solve two-phase flow problems, but they are used to derive jump conditions relating fluid variables on one side of the interface to those on the other. They also can be used to derive single-phase differential equations that can be averaged to obtain two-phase flow equations.

A.4 SINGLE-PHASE DIFFERENTIAL EQUATIONS

This section describes the derivation of the single-phase differential conservation equations. Equations for conservation of mass, momentum and energy are obtained by applying Equations A.7, A.9 and A.11 to an arbitrary material volume small enough to contain only one phase for some length of time. These equations and additional constitutive equations are presented here.

A.4.1 Mass, Momentum and Energy Equations

Mass

Application of the divergence theorem to Equation A.7 yields

$$\int_{V^m(t)} \left[\frac{\partial \rho}{\partial t} + \nabla \cdot (\rho \underline{U})\right] d\underline{x} = 0 \qquad (A.12)$$

Because $V^m(t)$ is arbitrary and the integrand is continous, Equation A.12 implies that the integrand must be zero throughout the phase. So,

$$\frac{\partial \rho}{\partial t} + \nabla \cdot (\rho \underline{U}) = 0 \qquad (A.13)$$

at any point in the interior of either phase.

Momentum

Let $\underline{\underline{T}}$ denote the stress tensor defined by

$$\underline{t} = \underline{n} \cdot \underline{\underline{T}} \tag{A.14}$$

Then divide $\underline{\underline{T}}$ into its pressure and viscous parts according to

$$\underline{\underline{T}} = -P\underline{\underline{I}} + \underline{\underline{\tau}} \tag{A.15}$$

The tensor $\underline{\underline{\tau}}$ is called the viscous stress tensor or the stress deviator. Then, using Equations A.14 and A.15 in Equation A.9 and manipulating as in the derivation of Equation A.13, the momentum equation can be expressed as

$$\frac{\partial}{\partial t}(\rho\underline{U}) + \nabla \cdot (\rho\underline{U}\underline{U}) = \rho\underline{f} - \nabla P + \nabla \cdot \underline{\underline{\tau}} \tag{A.16}$$

Equation A.16 is valid at any point in the interior of either phase.

Energy

Manipulating Equation A.11 as above and using Equation A.14 gives the differential conservation of energy equation within a phase:

$$\frac{\partial}{\partial t}[\rho(e + \tfrac{1}{2}|\underline{U}|^2)] + \nabla \cdot [\rho(e + \tfrac{1}{2}|\underline{U}|^2)\underline{U}] = -\nabla \cdot \underline{Q}$$

$$+ \dot{Q} + \rho f \cdot \underline{U} + \nabla \cdot (\underline{\underline{T}} \cdot \underline{U}) \tag{A.17}$$

The thermal energy equation is obtained by taking the dot product of the momentum equation and $\underline{U}$ and then subtracting the result from Equation A.17. The result, after a little manipulation, is

$$\frac{\partial}{\partial t}(\rho e) + \nabla \cdot (\rho e \underline{U}) = - \nabla \cdot \underline{Q} + \dot{Q} - P \nabla \cdot \underline{U} + \underline{\underline{\tau}} : \nabla \underline{U} \qquad (A.18)$$

The thermal energy equation can be written in terms of enthalpy by introducing

$$h = e + P/\rho \qquad (A.19)$$

The result is

$$\frac{\partial}{\partial t}(\rho h) + \nabla \cdot (\rho h \underline{U}) = - \nabla \cdot \underline{Q} + \dot{Q} + \frac{\partial P}{\partial t} + \underline{U} \cdot \nabla P + \underline{\underline{\tau}} : \nabla \underline{U} \qquad (A.20)$$

For development of the COBRA-TF equations, the enthalpy formulation is the most convenient form of the energy equations.

A.4.2 Additional Equations

Taken together, Equations A.13, A.16 and A.20 are not sufficient to solve for all the fluid variables in a single-phase region. Constitutive equations are needed for the conduction vector, $\underline{Q}$, and the stress deviator, $\underline{\underline{\tau}}$. Thermodynamic equations of state are also needed. Fourier's law for heat conduction gives $\underline{Q}$ as

$$\underline{Q} = - k(T) \nabla T \qquad (A.21)$$

For Newtonian fluid the constitutive equation for the stress deviator is

$$\underline{\underline{\tau}} = \lambda(\nabla \cdot \underline{U})\,\underline{\underline{I}} + \mu(\nabla\underline{U} + (\nabla\underline{U})^t) \tag{A.22}$$

In these equations

k = thermal conductivity

T = temperature

μ = viscosity

λ = second viscosity coefficient

The thermodynamic equations of state define the density and enthalpy as functions of pressure and temperature:

$$\begin{aligned} \rho &= \rho(P,T) \\ h &= h(P,T) \end{aligned} \tag{A.23}$$

Equations A.13, A.16 and A.20 through A.23 are sufficient to solve for all flow variables in a single-phase region, provided values for $\underline{f}$, $\dot{Q}$, k, μ and λ are known and suitable initial and boundary conditions are given. In a two-phase region the above equations are of little direct use in problem solving. They do, however, provide the basis for the derivation of average equations.

A.5 INTERFACIAL JUMP CONDITIONS

The exact integral conservation equations, Equations A.7, A.9 and A.11, can be used to obtain interfacial jump conditions for two-phase flows. The jump conditions relate flow variables on one side of the interface to those on the other. Such relations are useful for deriving constitutive models for the interfacial interaction terms that arise when the single-phase conservation equations are averaged to obtain the two-fluid model. This section describes the derivation of the jump conditions for mass, momentum and energy.

Consider a small material volume, $V^m(t)$, that contains some of each phase and part of the interface, as shown in Figure A.3. To obtain jump conditions one must examine the limit as $\delta \to 0$ of Equations A.7, A.9, and A.11.

A.5.1 Conservation of Mass at the Interface

Assuming $\frac{\partial \rho}{\partial t}$ is bounded, Equation A.7 becomes

$$\int_{S(t)} \{-(\rho_{1_I} \underline{U}_{1_I} - \rho_{2_I} \underline{U}_{2_I}) + (\rho_{1_I} - \rho_{2_I}) \underline{U}_I\} \cdot \underline{n}_1 \, ds = 0 \qquad (A.24)$$

Because the individual phase variables are continuous within each phase, and because S(t) is arbitrary, the integrand must be zero at all points of I(t). Thus

$$\rho_{1_I} (\underline{U}_{1_I} - \underline{U}_I) \cdot \underline{n}_1 = \rho_{2_I} (\underline{U}_{2_I} - \underline{U}_I) \cdot \underline{n}_1 \qquad (A.25)$$

Equation A.25 merely states that the rate at which mass leaves one phase equals the rate at which it enters the other.

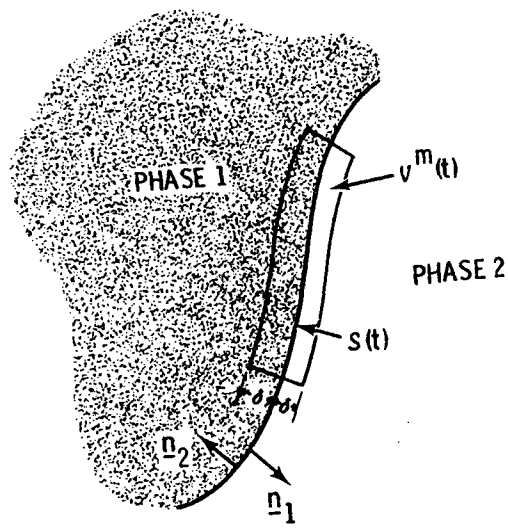

FIGURE A.3. Interface Material Volume

A.5.2 Conservation of Momentum at the Interface

Manipulating Equation A.9 in a manner similar to the manipulation of Equation A.7 above gives

$$\int_{S(t)} \{[-(\rho_{1_I} \underline{U}_{1_I} \underline{U}_{1_I} - \rho_{2_I} \underline{U}_{2_I} \underline{U}_{2_I}) + (\rho_{1_I} \underline{U}_{1_I} - \rho_{2_I} \underline{U}_{2_I}) \underline{U}_I$$

$$+ (\underline{\underline{T}}_{1_I} - \underline{\underline{T}}_{2_I})] \cdot \underline{n}_1 \} \, ds = \int_{\partial S(t)} \Sigma \, d\ell \qquad (A.26)$$

In most reactor safety applications it is permissible to neglect the effect of surface tension in the above equation. This immediately yields the local momentum jump condition as

$$- \rho_{1_I} \underline{U}_{1_I} (\underline{U}_{1_I} - \underline{U}_I) \cdot \underline{n}_1 + \rho_{2_I} \underline{U}_{2_I} (\underline{U}_{2_I} - \underline{U}_I) \cdot \underline{n}_1 + (\underline{\underline{T}}_{1_I} - \underline{\underline{T}}_{2_I}) \cdot \underline{n}_1 = \underline{0} \qquad (A.27)$$

It is possible to derive a local momentum jump condition without neglecting surface tension by invoking the surface divergence theorem (Ref. 4). (See, for instance, Reference 3).

Equations A.25 and A.27 can be combined to illustrate more clearly the jump condition for the stress tensor. First, the local rate of mass transfer to phase k per unit interfacial area can be defined as

$$\dot{m}_{k_I} = - \rho_{k_I} (\underline{U}_{k_I} - \underline{U}_I) \cdot \underline{n}_k \qquad (A.28)$$

Then Equation A.25 can be written

$$\dot{m}_{1_I} + \dot{m}_{2_I} = 0 \tag{A.29}$$

while A.27 becomes

$$(\underline{\underline{I}}_{1_I} - \underline{\underline{I}}_{2_I}) \cdot \underline{n}_1 = - \dot{m}_{1_I} (\underline{U}_{1_I} - \underline{U}_{2_I}) \tag{A.30}$$

Assuming no slip at the interface, the components of $\underline{U}_{1_I}$ and $\underline{U}_{2_I}$ tangential to the interface must be equal, and therefore the vector $(\underline{U}_{1_I} - \underline{U}_{2_I})$ is normal to the interface. Equation A.30 thus implies that the stress jump is also normal to the interface. A small amount of manipulation with Equations A.28, A.29 and A.30 yields

$$[(\underline{\underline{I}}_{1_I} - \underline{\underline{I}}_{2_I}) \cdot \underline{n}_1] \cdot \underline{n}_1 = \dot{m}_{1_I}^2 (\frac{1}{\rho_{1_I}} - \frac{1}{\rho_{2_I}}) \tag{A.31}$$

This shows that there is always a jump in the stress component normal to the interface unless there is no change of phase ($\dot{m}_{1_I} = \dot{m}_{2_I} = 0$) or the phase densities are equal at the interface. If the viscous contribution to the normal stress is neglected, Equation A.31 reduces to

$$P_{2_I} - P_{1_I} = \dot{m}_{1_I}^2 (\frac{1}{\rho_{1_I}} - \frac{1}{\rho_{2_I}}) \tag{A.32}$$

which shows that the pressure is higher in the denser fluid, regardless of the sign of $\dot{m}_{1_I}$.

A.5.3 Conservation of Energy at the Interface

The energy jump condition is obtained by neglecting the surface tension and collapsing Equation A.11 on the surface. This gives

$$\dot{m}_{1_I} \left[\left(e + \frac{1}{2}|\underline{U}|^2\right)_{1_I} - \left(e + \frac{1}{2}|\underline{U}|^2\right)_{2_I} - \left(\underline{Q}_{1_I} - \underline{Q}_{2_I}\right) \cdot \underline{n}_1\right.$$

$$\left. + \underline{n}_1 \cdot \left(\underline{\underline{T}}_{1_I} \cdot \underline{U}_{1_I} - \underline{\underline{T}}_{2_I} \cdot \underline{U}_{2_I}\right)\right] = 0 \qquad \text{(A.33)}$$

after Equations A.28 and A.29 have been applied.

A thermal energy jump condition can be derived by manipulating the momentum and energy jump conditions. However, since two different phase velocities are involved in Equation A.30, the result will still contain some mechanical energy terms. One approach, which expresses the mechanical energy terms as relative velocities between the phases and the interface, is to take the dot product of Equation A.30 and the interface velocity, $\underline{U}_I$. This gives

$$\dot{m}_{1_I} \left(\underline{U}_{1_I} - \underline{U}_{2_I}\right) \cdot \underline{U}_I + \left[\underline{n}_1 \cdot \left(\underline{\underline{T}}_{1_I} - \underline{\underline{T}}_{2_I}\right)\right] \cdot \underline{U}_I = 0 \qquad \text{(A.34)}$$

Subtracting Equation A.34 from Equation A.33 and rearranging yields the following thermal energy jump condition:

$$\dot{m}_{1_I} \left\{e_{1_I} + \frac{1}{2}|U_{1_I} - \underline{U}_I|^2 - \left[e_{2_I} + \frac{1}{2}|\underline{U}_{2_I} - \underline{U}_I|^2\right]\right\}$$

$$- \left(\underline{Q}_{1_I} - \underline{Q}_{2_I}\right) \cdot \underline{n}_1 + \underline{n}_1 \cdot \left[\underline{\underline{T}}_{1_I} \cdot \left(\underline{U}_{1_I} - \underline{U}_I\right) - \underline{\underline{T}}_{2_I} \cdot \left(\underline{U}_{2_I} - \underline{U}_I\right)\right] = 0 \qquad \text{(A.35)}$$

Equation A.35 can be used to obtain an enthalpy jump condition by introducing

$$h_{k_I} = e_{k_I} + \frac{p_{k_I}}{\rho_{k_I}} \tag{A.36}$$

The result after a little manipulation is

$$\dot{m}_{1_I} \{[h_{1_I} + \frac{1}{2}|\underline{U}_{1_I} - \underline{U}_I|^2 - \frac{1}{\rho_{1_I}} (\underline{\underline{\tau}}_{1_I} \cdot \underline{n}_1) \cdot \underline{n}_1]$$

$$- [h_{2_I} + \frac{1}{2} |\underline{U}_{2_I} - \underline{U}_I|^2 - \frac{1}{\rho_{2_I}} (\underline{\underline{\tau}}_{2_I} \cdot \underline{n}_1) \cdot \underline{n}_1\}$$

$$- (\underline{Q}_{1_I} - \underline{Q}_{2_I}) \cdot \underline{n}_1 = 0 \tag{A.37}$$

A.6 AVERAGE VARIABLES

Given appropriate initial and boundary conditions, the exact differential equations, together with the jump conditions and constitutive equations, could theoretically be solved to obtain the exact solution for all flow variables in a two-phase flow. In practice the solution is unattainable except in a few very simple flow situations. Moreover, the excess of detail that such a solution would provide is not needed in most engineering studies. What is needed are results describing the average motion of each phase in terms of suitable average variables. With this in mind, the following discussion defines the averaging method and introduces the average variables.

Let $f(\underline{x},t)$ be piecewise continuous and have piecewise continuous derivatives. Then the time average of $f(\underline{x},t)$ is given by

$$\overline{F}(\underline{x},t) = \frac{1}{\Delta t} \int_{t-\Delta t/2}^{t+\Delta t/2} f(\underline{x},t')dt' \tag{A.38}$$

The time interval, Δt, is chosen to be long enough to smooth out random fluctuations but short enough to preserve any gross unsteadiness in the flow.

The phase function, $\beta_k(\underline{x},t)$, is defined to isolate the contribution to the average from each phase:

$$\beta_k(\underline{x},t) = \begin{cases} 1 \text{ if } \underline{x} \in \text{phase k at time t} \\ 0 \text{ otherwise} \end{cases} \tag{A.39}$$

Then the average k-phase void fraction, α_k, is simply the average of the phase function:

$$\alpha_k = \overline{\beta}_k \tag{A.40}$$

The average k-phase density, ρ_k, is defined by

$$\alpha_k \rho_k = \overline{\beta_k \rho} \tag{A.41}$$

Velocities are weighted with density so that the average velocity is derived from averaged momenta, which makes the derivation of the averaged equations easier. Thus, the average k-phase velocity, $\underline{U}_k$, is defined by

$$\alpha_k \rho_k \underline{U}_k = \overline{\beta_k \rho \underline{U}} \tag{A.42}$$

The average k-phase stress tensor, $\underline{\underline{T}}_k$, is defined by

$$\alpha_k \underline{\underline{T}}_k = \overline{\beta_k \underline{\underline{T}}} \tag{A.43}$$

This leads to the obvious definitions for the average k-phase pressure and stress deviator:

$$\alpha_k P_k = \overline{\beta_k P}$$

and

$$\alpha_k \underline{\underline{\tau}}_k = \overline{\beta_k \underline{\underline{\tau}}} \tag{A.44}$$

The average k-phase enthalpy, h_k, is defined by

$$\alpha_k \rho_k h_k = \overline{\beta_k \rho h} \tag{A.45}$$

The average k-phase heat flux vector, $\underline{Q}_k$, is defined by

$$\alpha_k \underline{Q}_k = \overline{\beta_k \underline{Q}} \tag{A.46}$$

In Equations A.40 through A.46 the averaging method defined by Equation A.38 has been applied to piecewise continuous functions defined in both phases. Some variables, however, such as $\underline{U}_I$ and ψ_{k_I}, are defined only at

points on the interface and therefore require a different type of averaging. The next few paragraphs describe this surface averaging method and introduce the surface average variables.

During the averaging period, Δt, several interfaces may pass any given location $\underline{x}$. Let the subscript j denote the jth such interface, and let

$$v_j = |\underline{U}_I \cdot \underline{n}_I| = \text{the normal displacement speed of the jth interface to pass location } \underline{x} \text{ during the averaging period, } \Delta t. \tag{A.47}$$

$$L_j = v_j \, \Delta t \tag{A.48}$$

$$\frac{1}{L_s} = \sum_j \frac{1}{L_j} \tag{A.49}$$

where the sum is over all interfaces that pass location $\underline{x}$ during time interval Δt. The term $1/L_j$ is the surface area concentration due to the jth interface, and $1/L_s$ is the total surface area concentration. Then if ψ_I is a surface variable, the surface average of ψ_I is defined by

$$\overline{\psi_I}^s = L_s \left(\sum_j \frac{\psi_{I_j}}{L_j} \right) \tag{A.50}$$

where the sum is over all surfaces that pass location $\underline{x}$ during Δt.

The average k-phase mass supply per unit interface area, $\dot{m}_k$, is defined by

$$\dot{m}_k = \overline{\dot{m}_{k_I}}^s \tag{A.51}$$

while the average k-phase mass supply per unit volume, Γ_k, is given by

$$\Gamma_k = \frac{\dot{m}_k}{L_s} \tag{A.52}$$

The average interface velocity, $\underline{U}^i$, is defined by

$$\dot{m}_k \underline{U}^i = \overline{\dot{m}_{k_I} \underline{U}_I}^s \tag{A.53}$$

and the average k-phase limit velocity, $\underline{U}_k^i$, is given by

$$\dot{m}_k \underline{U}_k^i = \overline{\dot{m}_{k_I} \underline{U}_{k_I}}^s \tag{A.54}$$

The surface average k-phase limit stress tensor, $\underline{\underline{I}}_k^i$, is given by

$$\underline{\underline{I}}_k^i = \overline{\underline{\underline{I}}_{k_I}}^s \tag{A.55}$$

with

$$p_k^i = \overline{p_{k_I}}^s$$

and

$$\underline{\underline{\tau}}_k^i = \overline{\underline{\underline{\tau}}_{k_I}}^s \tag{A.56}$$

The surface average interfacial heat input to phase k per unit volume is defined by

$$q''' _{I_k} = - \frac{1}{L_s} \left(\overline{\underline{n}_k \cdot \underline{Q}_{k_I}}^{s} \right) \tag{A.57}$$

The surface average k-phase limit enthalpy, h_k^i, is given by

$$\dot{m}_k \, h_k^i = \overline{\dot{m}_{k_I} h_{k_I}}^{s} \tag{A.58}$$

In addition to the average variables defined above, it is necessary to introduce notation for the turbulent fluxes that arise as a result of the averaging process. To do this, it is convenient to define fluctuating quantities as

$$\psi' = \psi - \psi_k \tag{A.59}$$

where ψ is the instantaneous value and ψ_k is the average value. The usual assumption is that the average of ψ' is zero if the averaging operation is the same as that used to define ψ_k. (Fluctuating values can also be defined for surface average variables, but these are not needed in the COBRA-TF development.)

Using the notation of Equation A.59, the k-phase turbulent stress tensor, $\underline{\underline{T}}_k^T$, is defined by

$$\alpha_k \underline{\underline{T}}_k^T = - \overline{\beta_k \rho \underline{U}' \underline{U}'} \tag{A.60}$$

and the k-phase turbulent heat flux, $\underline{q}_k^T$, is defined by

$$\alpha_k \underline{q}_k^T = \overline{\beta_k \rho h' \underline{U}'} \tag{A.61}$$

Additional average variables could be defined, e.g., average internal energy or average entropy, but the above-defined variables are sufficient for the development of the COBRA-TF equations. Readers interested in a more extensive treatment of the two-fluid model are referred to Ishii (Ref. 3).

A.7 AVERAGE EQUATIONS

Average phasic conservation equations are derived by taking the time average of the single-phase conservation equations and applying the definitions of the average variables and turbulent fluxes. When the time average is taken, expressions relating the average of a derivative to the derivative of an average variable are needed. These relations are presented in this section, and the phasic conservation equations that form the basis for the COBRA-TF three-field model are derived.

A.7.1 Derivative Relations

Two fundamental relations are used repeatedly in the derivations to follow. From Ishii's (Ref. 3) work, these are

$$\overline{\frac{\partial}{\partial t}(\beta_k \psi)} = \frac{\partial}{\partial t}\overline{(\beta_k \psi)} - \frac{1}{\Delta t}\sum_j \frac{1}{v_j} \psi_{k_I}(\underline{x}, t_j)\,(\underline{n}_k \cdot \underline{U}_{I_j}) \tag{A.62}$$

$$\overline{\nabla(\beta_k \psi)} = \nabla\overline{(\beta_k \psi)} + \frac{1}{\Delta t}\sum_j \frac{1}{v_j}[\underline{n}_k\, \psi_{k_I}(\underline{x}, t_j)] \tag{A.63}$$

Equations A.62 and A.63 can be derived using Leibnitz's theorem as given by Equations A.2 and A.4. In these equations the subscript j stands for the jth interface to pass point $\underline{x}$ during the averaging period, Δt. For a discussion of the singular case $v_j = 0$ see Ishii (Ref. 3) or Drew and Lahey (Ref. 7).

Relations for the derivatives of the void fraction can be derived from Equations A.62 and A.63 as

$$\nabla\alpha_k = -\frac{1}{\Delta t}\sum_j \frac{1}{\nu_j}\underline{n}_k \tag{A.64}$$

$$\frac{\partial\alpha_k}{\partial t} = \frac{1}{\Delta t}\sum_j \frac{1}{\nu_j}\underline{n}_j \cdot \underline{U}_{I_j} \tag{A.65}$$

A.7.2 Phasic Conservation Equations

Mass

Considering Equation A.13 for kth phase only and taking the time average gives

$$\overline{\frac{\partial}{\partial t}(\beta_k\rho)} + \overline{\nabla\cdot(\beta_k\rho\underline{U})} = 0 \tag{A.66}$$

Invoking Equations A.62, A.63, and the definition of Γ_k yields the average k-phase conservation of mass equation:

$$\frac{\partial}{\partial t}(\alpha_k\rho_k) + \nabla\cdot(\alpha_k\rho_k\underline{U}_k) = \Gamma_k \tag{A.67}$$

Momentum

When Equation A.16 is time averaged the result is

$$\frac{\partial}{\partial t}(\alpha_k \rho_k \underline{U}_k) + \nabla \cdot (\alpha_k \rho_k \underline{U}_k \underline{U}_k) = \alpha_k \rho_k f_k - \nabla(\alpha_k P_k)$$

$$+ \nabla \cdot [\alpha_k (\underline{\underline{\tau}}_k + \underline{\underline{T}}_k^T)] - \underline{M}_k \qquad (A.68)$$

Note that Equations A.59 and A.60 have been used to introduce the turbulent stress tensor into the above equation. Also, the average k-phase interfacial supply of momentum has been defined as

$$\underline{M}_k = \frac{1}{\Delta t} \sum_j \frac{1}{\nu_j} \{\rho_{k_I} \underline{U}_{k_I} (\underline{U}_{k_I} - \underline{U}_I) \cdot \underline{n}_k - \underline{n}_k \cdot \underline{\underline{T}}_{k_I}\}_j \qquad (A.69)$$

At this point it is worthwhile to examine the momentum supply term a little more closely. Separating the stress tensor into its pressure and viscous parts and using Equation A.64 gives

$$\underline{M}_k = \frac{1}{\Delta t} \sum_j \frac{1}{\nu_j} \{\underline{U}_{k_I} \dot{m}_{k_I} - \underline{n}_k P_{k_I} + \underline{n}_k \cdot \underline{\underline{\tau}}_{k_I}\}_j$$

$$= \Gamma_k \underline{U}_k^i + P_k^i \nabla \alpha_k - \frac{1}{\Delta t} \sum_j \frac{1}{\nu_j} [P_{k_{I_j}} - P_k^i] \underline{n}_k$$

$$+ \frac{1}{\Delta t} \sum_j \frac{1}{\nu_j} (\underline{n}_k \cdot \underline{\underline{\tau}}_{k_{I_j}}) \qquad (A.70)$$

Making the definitions

$$\underline{M}_k^d = \frac{1}{\Delta t} \sum_j \frac{1}{\nu_j} \{[P_k^i - P_{k_{I_j}}] \underline{n}_k + \underline{n}_k \cdot \underline{\underline{\tau}}_{k_{I_j}}\} \tag{A.71}$$

$$\underline{M}_k^\Gamma = \Gamma_k \underline{U}_k^i \tag{A.72}$$

yields the more compact expression

$$\underline{M}_k = \underline{M}_k^\Gamma + P_k^i \nabla\alpha_k + \underline{M}_k^d \tag{A.73}$$

Physically, the term $\underline{M}_k^\Gamma$ represents the momentum supplied to phase k due to change of phase, and $P_k^i \nabla\alpha_k$ is the force on phase k due to the average interfacial pressure. The term $\underline{M}_k^d$ is traditionally called the drag force, although it may also include lift and virtual mass forces (Ref. 7).

Substitution of Equation A.73 into A.68 will yield the general k-phase conservation of momentum equation. The equation will contain the term $(P_k^i - P_k) \nabla\alpha_k$, which represents a force due to the difference between the average pressure in the bulk of phase k and that at the interface. The COBRA-TF model assumes $P_k^i = P_k$. Moreover, the model assumes that the average pressure is the same in all phases, i.e., $P_k^i = P_k = P$. Such an assumption is certainly reasonable for flows that do not involve phase change. When phase change is occurring, Equation A.32 shows that there must be a pressure difference across the interface unless the phase densities are equal. Consequently, it seems logical for the average phase pressures to be different in this case. For most cases of practical importance, however, this difference is small enough to neglect.

An additional assumption, compatible with the intended applications of COBRA-TF, is that gravity is the only body force; i.e., $\underline{f}_k = \underline{g}$ for all phases.

Substituting Equations A.73 into Equation A.68 and implementing the assumptions discussed above yields the phasic conservation of momentum equation used by COBRA-TF,

$$\frac{\partial}{\partial t}(\alpha_k \rho_k \underline{U}_k) + \nabla \cdot (\alpha_k \rho_k \underline{U}_k \underline{U}_k) = \alpha_k \rho_k \underline{g} - \alpha_k \nabla P$$

$$+ \nabla \cdot [\alpha_k (\underline{\underline{\tau}}_k + \underline{\underline{I}}^T) + \underline{M}_k^\Gamma + \underline{M}_k^d \qquad \text{(A.74)}$$

Energy

For reactor safety analysis the most useful form of the single-phase energy equation is the enthalpy formulation, Equation A.20. Since most flows of interest in this field involve relatively low velocities and because thermal effects predominate, it is permissible to neglect the dissipation and the spatial derivative of the pressure in Equation A.20. Also, the intended applications of COBRA-TF do not include flows with heat generation in the fluid. The equation to be averaged is therefore

$$\frac{\partial}{\partial t}(\rho h) + \nabla \cdot (\rho h \underline{U}) = - \nabla \cdot \underline{Q} + \frac{\partial P}{\partial t} \qquad \text{(A.75)}$$

Readers interested in the complete treatment of the full energy equation should consult one of the references cited in the introduction to this appendix.

Averaging Equation A.75 yields

$$\frac{\partial}{\partial t}(\alpha_k \rho_k h_k) + \nabla \cdot (\alpha_k \rho_k h_k \underline{U}_k) = - \nabla \cdot [\alpha_k (\underline{Q}_k + \underline{q}_k^T)] + \Lambda_k + \alpha_k \frac{\partial P}{\partial t} \qquad \text{(A.76)}$$

where Equations A.59, A.61, A.62 and A.63 have been used. The averaging process has introduced the average k-phase interfacial supply of energy, defined as

$$\Lambda_k = -\frac{1}{\Delta t}\sum_j \frac{1}{\nu_j}\left(\rho_{k_I} h_{k_I}\right)_j \left(\underline{U}_{k_I} - \underline{U}_I\right)_j \cdot \underline{n}_k$$

$$-\frac{1}{\Delta t}\sum_j \frac{1}{\nu_j}\left(\underline{n}_k \cdot \underline{Q}_{k_I}\right)_j \qquad \text{(A.77)}$$

Equations A.77 can be written in a more convenient form by using the definitions of Γ_k, h_k^i and q'''_{k_I}:

$$\Lambda_k = \Gamma_k\, h_k^i + q'''_{k_I} \qquad \text{(A.78)}$$

The energy equation used to derive the COBRA-TF three-field model is obtained by substituting Equation A.78 into Equation A.76. The result is

$$\frac{\partial}{\partial t}\left(\alpha_k \rho_k h_k\right) + \nabla \cdot \left(\alpha_k \rho_k h_k \underline{U}_k\right) = -\nabla \cdot \left[\alpha_k \left(\underline{Q}_k + \underline{q}_k^T\right)\right] + \Gamma_k\, h_k^i + q'''_{k_I} + \alpha_k \frac{\partial P}{\partial t} \qquad \text{(A.79)}$$

REFERENCES

1. D. A. Drew, "Averaged Field Equations for Two-Phase Media." Studies in Applied Mathematics. L(2): 133-166, 1971.

2. P. Vernier and J. M. Delhaye, "General Two-Phase Flow Equations Applied to the Thermodynamics of Boiling Nuclear Reactors," Energie Primaire 4(1-2).

3. M. Ishii, Thermo-Fluid Dynamic Theory of Two-Phase Flow. Eyrolles, Paris, France, 1975.

4. R. Aris, Vectors, Tensors, and the Basic Equations of Fluid Mechanics. Prentice-Hall, Englewood Cliffs, New Jersey, 1962.

5. J. M. H. Olmstead, Real Variables. Appleton-Century-Crofts, New York, New York, 1959.

6. C. Truesdell and R. Toupin, "The Classical Field Theories," in Handbook der Physik. 3(1).

7. D. A. Drew and R. T. Lahey, "Application of General Constitutive Principles to the Derivation of Multidimensional Two-Phase Flow Equations," Internation Journal of Multiphase Flow 5, 243-264 (1979).

APPENDIX B

NUCLEAR FUEL ROD MATERIAL PROPERTIES

APPENDIX B

NUCLEAR FUEL ROD MATERIAL PROPERTIES

As part of the default nuclear fuel rod model, the material properties of uranium-dioxide and zircaloy from MATPRO-11 (Revision 1) (Ref. 1) were built into the code. They were implemented as statement functions to allow easy modification. The correlations used are shown below.

URANIUM DIOXIDE

Density (cold) (lbm/ft^3):

$$\rho_{UO_2} = 684.86*D \qquad (B.1)$$

where D = fraction of theoretical density (input)

Thermal Conductivity (Btu/hr-ft-°F):

The UO_2 thermal conductivity is computed from the MATPRO-9 (Ref. 2) correlation instead of the more complex version in MATPRO-11 (Revision 1) to save computer time. Both correlations have the same error band (0.2 W/m-°K) and give very nearly the same conductivity over the expected operating range of 500-3000K. A comparison is shown in Figure B-1. The thermal conductivity is computed by

$$k_{UO_2} = C \times \{\text{MAXIMUM } (0.0194,\ 40.4/(464. + T_c)$$

$$+ 1.216\times10^{-4} \text{ EXP } (1.867 \times 10^{-3})T_c)\} \qquad (B.2)$$

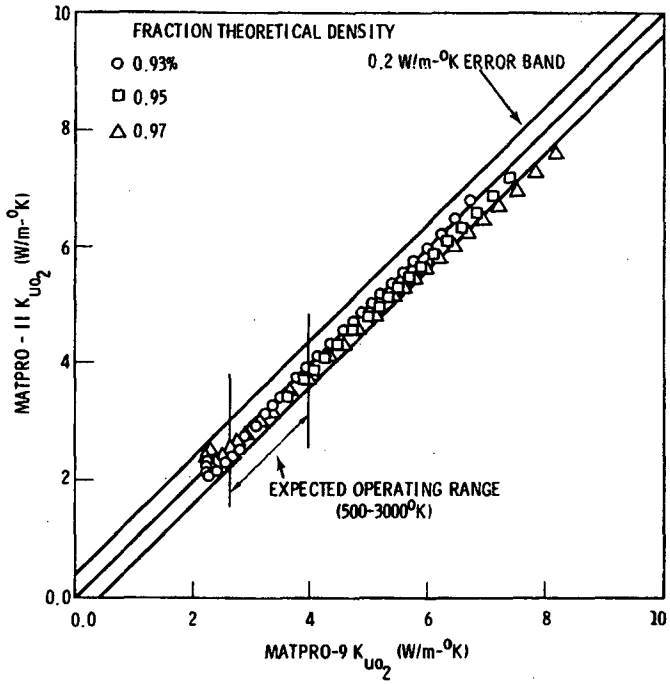

FIGURE B.1. Comparison of MATPRO-9 and MATPRO-11 Conductivities

where $C = (0.5779)\ 100\ [1. - \beta\ (1 - D)]/(1.0 - 0.05\ \beta)$

$\beta = 2.58 - (5.8 \times 10^{-4})T_C$

T_C = temperature (°C)

Specific Heat (Btu/lbm-°F):

$$C_{p_{UO_2}} = (2.388 \times 10^{-4}) \left\{ \frac{K_1\ \theta^2\ \exp(\theta/T_k)}{T_k^2[\exp\ (\theta/T_k) - 1]^2} + K_2 T_k \right.$$

$$\left. + \frac{O/M}{2} \frac{K_3\ E_D}{R\ T_k^2} \exp\ (-E_D/RT_k) \right\} \qquad \text{(B-3)}$$

where T_k = temperature (°K)

R = 8.3143 (J/mol-°K)

θ = Einstein temperature (535.285 °K)

K_1 = 296.7 (J/kg-°K)

K_2 = 2.43×10^{-2} (J/kg-°K)

K_3 = 8.745×10^{7} (J/kg)

E_D = 1.577×10^{5} (J/mol)

O/M = oxygen/metal ratio (2.0)

Zircaloy

Density (cold) (lbm/ft^3):

$$\rho_Z = 409.0 \tag{B.4}$$

Thermal conductivity (Btu/hr-ft-°F)

$$k_Z = .5779 \left[7.51 + 0.0209\, T_K - (1.45 \times 10^{-5})\, T_k^{\,2} + (7.67 \times 10^{-9})\, T_k^{\,3}\right] \tag{B.5}$$

where T_k = temperature (°K)

Specific Heat (Btu/lbm-°F)

MATPRO-11 (Revision 1) uses a table lookup and determines C_p as a function of temperature using the values shown in Table B.1.

TABLE B.1. Specific Heat of Zircaloy as a Function of Temperature

T(°K)	Cp (Btu/lbm-°F)
300.	.0671
400.	.07212
640.	.07904
1090.	.08955
1093.	.11988
1113.	.14089
1133.	.14686
1153.	.1717
1173.	.1949
1193.	.1839
1213.	.1478
1233.	.1120
1248.	.0850
>1248.	.0850

Material properties other than uranium-dioxide and Zircaloy can be input in material property tables. The required input is:

- cold state density
- thermal conductivity versus temperature
- specific heat versus temperature

EMISSIVITIES FOR UO_2 AND ZIRCALOY

The gap conductance model draws heavily on the MATPRO-11 (Revision 1) correlations to provide quantities needed for various models.

For the radiation heat transfer model, the fuel and cladding thermal emissivities from FEMISS and ZOEMIS are used.

From FEMISS in MATPRO-11 (Revision 2) (Ref. 4) the emissivity of UO_2 is given by

$$\varepsilon_1 = 0.7856 + 1.5263 \times 10^{-5} T_k \tag{B.6}$$

where T_k = temperature (K)

The cladding emissivity is set to the constant value $E_2 = 0.75$, based on the data in MATPRO-11 subroutine ZOEMIS.

FILL GAS CONDUCTIVITY

The thermal conductivity of the gas mixture as a function of temperature is determined from the relation

$$k_{gas} = \sum_{i=1}^{N} \frac{k_i}{1 + \sum_{\substack{j=1 \\ j \neq i}}^{N} \psi_{ij} \frac{X_j}{X_i}} \tag{B.7}$$

where N = number of component gases (limited to 6)

$$\psi_{ij} = \phi_{ij} \left[1 + 2.41 \frac{(M_i - M_j)(M_i - 0.142\, M_j)}{(M_i + M_j)^2}\right] \tag{B.8}$$

and

$$\phi_{ij} = \frac{\left[1 + \left(\frac{k_i}{k_j}\right)^{1/2} \left(\frac{M_i}{M_j}\right)^{1/4}\right]^2}{2^{3/2}\left(1 + \frac{M_i}{M_j}\right)^{1/2}} \qquad \text{(B.9)}$$

where M_i = molecular weight of gas species i

X_i = mole fraction of gas species i

k_i = thermal conductivity of gas species i

The thermal conductivities of the six component gases are evaluated as a function of temperature from the following relations:

	Gas	k(Btu/hr-ft-°F)
1-	Helium	$(1.314\times10^{-3})\ T_g^{\ 0.668}$
2-	Xenon	$(1.395\times10^{-5})\ T_g^{\ 0.872}$
3-	Argon	$(1.31\times10^{-3})\ T_g^{\ 0.701}$
4-	Krypton	$(1.588\times10^{-5})\ T_g^{\ 0.92331}$
5-	Hydrogen	$(5.834\times10^{-4})\ T_g^{\ 0.8213}$
6-	Nitrogen	$(7.35\times10^{-5})\ T_g^{\ 0.846}$

where T_g = gas temperature (°R).

For conductance between the fuel and cladding when in physical contact, the thermal conductivity for UO_2 is determined using the relation given in Equation B.2 above. The cladding thermal conductivity is calculated with Equation B.5.

MEYER HARDNESS FOR ZIRCALOY

The Meyer hardness number, H_M, used in the relation for the solid heat conductance is

$$H_M = (1.4504 \times 10^{-4}) \exp [\ 26.03 - (0.02639)T_Z + (4.3502 \times 10^{-5})T_Z^2 - (2.5621 \times 10^{-8})T_Z^3] \quad (B.10)$$

where H_M = Meyer hardness of the cladding (psi)

T_Z = cladding temperature (K)

STRAIN IN UO_2 AND ZIRCALOY

The strain in UO_2 fuel due to thermal expansion, a parameter needed in the fuel deformation model, is calculated using the relation from FTHEXP in MATPRO-11 (Revision 2). This equation is

$$\varepsilon_{UO_2} = (1.0 \times 10^{-5})T - (3.0 \times 10^{-3}) + (4.0 \times 10^{-2}) \exp \left[\frac{(-6.9 \times 10^{-20})}{\sigma_{SB} T}\right] \quad (B.11)$$

where ε = thermal strain for UO_2 based on 300K reference temperature

T = fuel pellet temperature (K)

σ_{SB} = Boltzmann constant = 1.38×10^{-23} J/K.

The strain in the cladding is calculated for axial and radial directions.

For 300°K < T < 1073°K, the zircaloy α-phase,

$$\varepsilon_{Z_L} = (4.44 \times 10^{-6})T - (1.24 \times 10^{-3}) \quad (B.12)$$

$$\varepsilon_{Z_r} = (6.72 \times 10^{-6})T - (2.07 \times 10^{-3}) \quad (B.13)$$

For, 1273K < T < melting, the zircaloy β-phase

$$\varepsilon_{Z_L} = (9.7 \times 10^{-6})T - (1.10 \times 10^{-2}) \quad \text{(B.14)}$$

$$\varepsilon_{Z_r} = (9.7 \times 10^{-6})T - (9.45 \times 10^{-3})$$

where T = cladding temperature (K).

In the α-phase to β-phase transition zone, 1073°K < T < 1273°K, very little data exist. For this temperature range the thermal strain values are determined directly from Scott's data (Ref. 3) as presented in MATPRO-11 (Revision 1).

STRESS IN UO_2 AND ZIRCALOY

The mechanical stress in the cladding is calculated using Young's modulus and the shear modulus for zircaloy as calculated in CELMOD and CSHEAR in MATPRO-11. The effects of oxidation, cold work and irradiation are ignored. The relations are given by the following equations.

Young's modulus, E, (in Pa) for zircaloy 2 and 4:

For, T < 1093°K, the zircaloy α-phase

$$E_{Z_\alpha} = (1.088 \times 10^{11}) - (5.475 \times 10^{7})T$$

For, T > 1239°K, the zircaloy β-phase

$$E_{Z_\beta} = (9.21 \times 10^{10}) - (4.05 \times 10^{7})T \quad \text{(B-15)}$$

where T = the cladding temperature (°K)

The shear modulus, G, (in Pa) for zircaloy

For, $T < 1093°K$, the zircaloy α-phase

$$G_{Z_\alpha} = (4.04 \times 10^{10}) - (2.168 \times 10^{7})T \qquad \text{(B.16)}$$

For, $T > 1239°K$, the zircaloy β-phase

$$G_{Z_\beta} = (3.48 \times 10^{10}) - (1.66 \times 10^{7})T \qquad \text{B.17)}$$

where T = the cladding temperature (°K).

In the α-phase to β-phase transition region, linear interpolation is used to obtain G and E.

Poisson's ratio is obtained from the identity:

$$\nu = \frac{E}{2G} - 1 \qquad \text{(B.18)}$$

Appendix B

REFERENCES

1. D. L. Hagrman, G. A. Reymann, and R. E. Mason. Idaho National Engineering Laboratories, "MATPRO - Version 11 (Revision 1): A Handbook of Materials Properties for Use in the Analysis of Light Water Reactor Fuel Rod Behavior," USNRC Report NUREG/CR-0497, TREE-1280, Revision 1, February 1980.

2. P. E. MacDonald et al, "MATPRO - Version 9: A Handbook of Materials Properties for Use in the Analysis of Light Water Reactor Fuel Rod Behavior," Idaho National Engineering Laboratories, TREE-NUREG-1005, 1976.

3. D. B. Scott. "Physical and Mechanical Properties of Zircaloy-2 and -4," WCAP-3269-41, pp. 8-12, May 1965.

4. D. L. Hagrman, G. A. Reymann, and R. E. Mason. Idaho National Engineering Laboratories, "MATPRO - Version 11 (Revision 2): A Handbook of Materials Properties for Use in the Analysis of Light Water Reactor Fuel Rod Behavior," USNRC Report NUREG/CR-0497, TREE-1280, Revision 2, August 1981.

APPENDIX C

CALCULATION OF THERMAL CONNECTORS

APPENDIX C

CALCULATION OF THERMAL CONNECTORS

The internode conductance, $K_{i,i+1}$, between nodes i and i+1, as shown in Figure C.1, is calculated from

$$K_{i,i+1} = 1/(R_{i,i+1} + R_{i+1,i}) \qquad (C.1)$$

The thermal resistance $R_{i,i+1}$ is the resistance to heat flow from node i to the boundary between nodes i and i+1. The thermal resistance $R_{i+1,i}$ is the resistance to heat flow from node i+1 to the boundary between i+1 and i. Formulas for these resistances for both plate and cylindrical geometries are given below.

FLAT PLATE

The steady, one-dimensional heat conduction equation with no internal generation is

$$\frac{d^2T}{dx^2} = 0 \qquad (C.2)$$

with the boundary conditions (see Figure C.2)

$$X = 0 \quad , \quad T = T_1$$

$$X = L \quad , \quad T = T_2$$

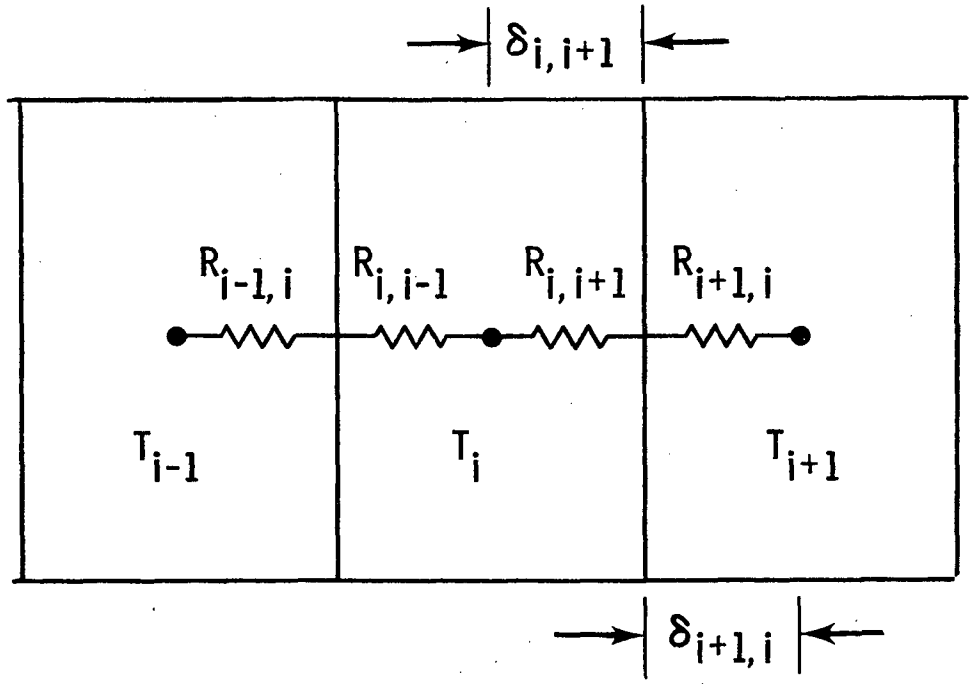

FIGURE C.1. Heat Balance Control Volume

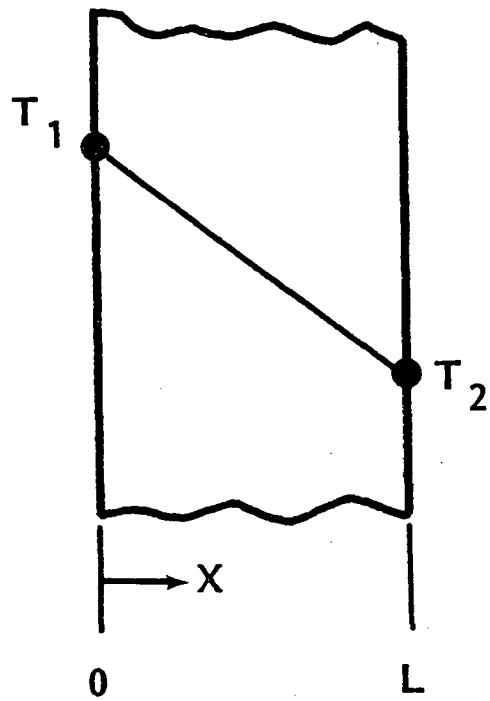

FIGURE C.2. Steady-State Temperature Distribution in a Slab with no Internal Heat Generation

Integrating Equation C.2 and applying the boundary conditions gives the following formula for temperature distribution in the plate:

$$T = (T_2 - T_1)\left(\frac{X}{L}\right) + T_1 \qquad (C.3)$$

where L = thickness of the plate.

The rate of heat transfer, from the Fourier equation, is

$$q = -kA\frac{\partial T}{\partial X} = \frac{kA}{L}(T_1 - T_2) \qquad (C.4)$$

where k = thermal conductivity of the plate

A = surface area perpendicular to the direction of heat flow

If the heat transfer is thought of as energy being pushed down a temperature gradient against some thermal resistance, q can be expressed as

$$q = \frac{\Delta T}{R} \qquad (C.5)$$

Then

$$R = \frac{L}{kA} \qquad (C.6)$$

Therefore, the resistance from node i to the boundary between i and i+1 for a flat plate is

$$R_{i,i+1} = \frac{\delta_{i,i+1}}{k_i A} \qquad (C.7)$$

The total resistance from node i to node i+1 is $(R_{i,i+1} + R_{i+1,i})$. The conductance, K, between nodes i and i+1 is therefore

$$K_{i,i+1} = K_{i+1,i} = \frac{k_i k_{i+1} A}{k_{i+1}\delta_{i,i+1} + k_i \delta_{i+1,i}} \tag{C.8}$$

where $\delta_{i,i+1}$ = distance from node i to boundary between nodes i and i+1
A = area
k_i, k_{i+1} = thermal conductivity of the material in node i and i+1, respectively.

CYLINDER

For steady radial flow of heat through the wall of a hollow cylinder (see Figure C.3) the conduction is

$$\frac{1}{r}\frac{\partial}{\partial r}\left(r \frac{\partial T}{\partial r}\right) = 0 \tag{C.9}$$

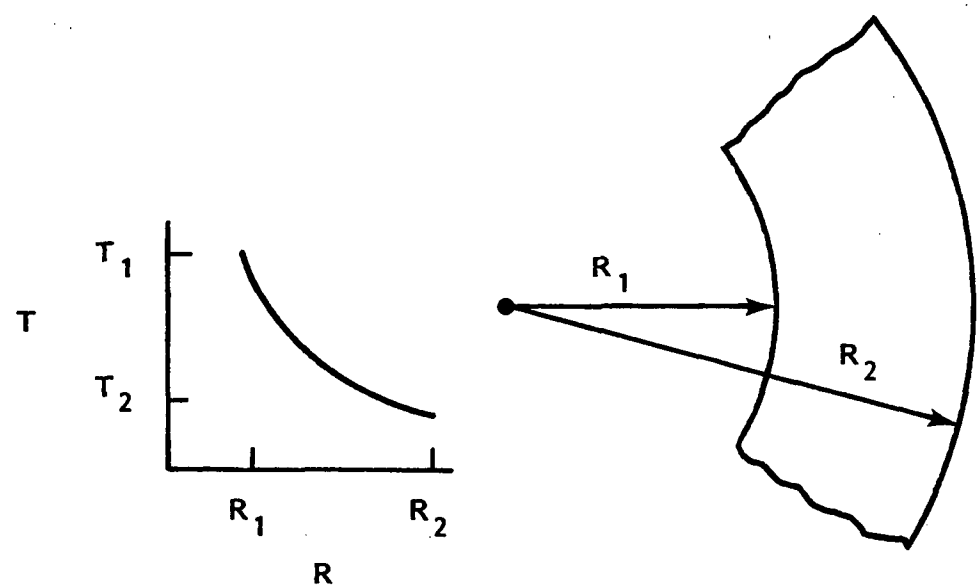

FIGURE C.3. Steady-State Temperature Distribution in a Cylinder Wall

with boundary conditions

$$r = r_1 \quad , \quad T = T_1$$
$$r = r_2 \quad , \quad T = T_2$$

Integration of Equation C.9 yields

$$T = \frac{T_1 - T_2}{\ln\left(\frac{r_1}{r_2}\right)} \ln\left(\frac{r}{r_2}\right) + T_2 \tag{C.10}$$

The rate of heat flow is

$$q = -k(2\pi r\,\Delta X)\frac{\partial T}{\partial r} = \frac{2\pi\Delta X}{\ln\left(\frac{r_2}{r_1}\right)}(T_1 - T_2) \tag{C.11}$$

and the resistance is

$$R = \frac{\ln\left(\frac{r_2}{r_1}\right)}{2\pi k\,\Delta X} \tag{C.12}$$

where ΔX = node length in axial direction.

Therefore, the resistance from node i to the boundary between i and i+1 for a cylinder is

$$R_{i,i+1} = \frac{\ln\left[\frac{(r_i + \delta_{i,i+1})}{r_i}\right]}{2\pi k\,(\Delta X)} \tag{C.13}$$

where r_i = radius of node i

$\delta_{i,i+1}$ = radial distance from r_i to node boundary.

The total resistance between nodes i and i+1 is $(R_{i,i+1} + R_{i+1,i})$, so the conductance is

$$K_{i,i+1} = K_{i+1,i} = \frac{2\pi k_i k_{i+1} \Delta X}{k_{i+1} \ln (r_B/r_i) + k_i \ln (r_{i+1}/r_B)} \qquad (C.14)$$

where $r_B = r_i + \delta_{i,i+1}$

The formulation for the hollow cylinder applies also to solid cylinders, simply by assuming an adiabatic condition on the inside boundary.

NUREG/CR-3046
PNL-4385
R4

DISTRIBUTION

No. of Copies

OFFSITE

335 U.S. Nuclear Regulatory Commission
Division of Technical Information and Document Control
7920 Norfolk Avenue
Bethesda, MD 20014

5 James Han
U.S. Nuclear Regulatory Commission
7915 Eastern Ave.
M/S 1130-SS
Silver Spring, MD 20910

No. of Copies

ONSITE

50 Pacific Northwest Laboratory

MJ Thurgood (43)
Publishing Coordination (2)
Technical Information ED (5)

NRC FORM 335 (11-81) U.S. NUCLEAR REGULATORY COMMISSION

BIBLIOGRAPHIC DATA SHEET

1. REPORT NUMBER *(Assigned by DDC)*
NUREG/CR-3046, Vol. 1
PNL-4385

4. TITLE AND SUBTITLE *(Add Volume No., if appropriate)*
COBRA/TRAC - A Thermal Hydraulics Code for Transient Analysis of Nuclear Reactor Vessels and Primary Coolant Systems - Volume 1: Equations and Constitutive Models

2. *(Leave blank)*

3. RECIPIENT'S ACCESSION NO.

7. AUTHOR(S)
M. J. Thurgood, J. M. Kelly, T. E. Guidotti, R. J. Kohrt, K. R. Crowell

5. DATE REPORT COMPLETED
MONTH: November | YEAR: 1982

9. PERFORMING ORGANIZATION NAME AND MAILING ADDRESS *(Include Zip Code)*
Pacific Northwest Laboratory
PO Box 999
Richland, Washington 99352

DATE REPORT ISSUED
MONTH: March | YEAR: 1983

6. *(Leave blank)*

8. *(Leave blank)*

12. SPONSORING ORGANIZATION NAME AND MAILING ADDRESS *(Include Zip Code)*
Division of Accident Evaluation
Office of Nuclear Regulatory Research
U.S. Nuclear Regulatory Commission
Washington, DC 20555

10. PROJECT/TASK/WORK UNIT NO.

11. FIN NO.
FIN B2391

13. TYPE OF REPORT
Computer Code Manual

PERIOD COVERED *(Inclusive dates)*

15. SUPPLEMENTARY NOTES

14. *(Leave blank)*

16. ABSTRACT *(200 words or less)*

The COBRA/TRAC computer program has been developed to predict the thermal-hydraulic response of nuclear reactor primary coolant systems to small and large break loss-of-coolant accidents and other anticipated transients. The code solves the compressible three-dimensional, two-fluid, three-field equations for two-phase flow in the reactor vessel. The three fields are the vapor field, the continuous liquid field, and the liquid drop field. A five-equation drift flux model is used to model fluid flow in the primary system piping, pressurizer, pumps, and accumulators. The heat generation rate of the core is specified by input and no reactor kinetics calculations are included in the solution. This volume describes the conservation equationsand physical models used in the vessel module.

17. KEY WORDS AND DOCUMENT ANALYSIS

17a. DESCRIPTORS

17b. IDENTIFIERS/OPEN-ENDED TERMS

18. AVAILABILITY STATEMENT
Unlimited

19. SECURITY CLASS *(This report)*
Unclassified

21. NO. OF PAGES

20. SECURITY CLASS *(This page)*
Unclassified

22. PRICE
S

NRC FORM 335 (11-81)

* U.S. GOVERNMENT PRINTING OFFICE: 1983-381-297:3008